Astronomy Reports, Vol. 45, No. 7, 2001, pp. 497–501. Translated from Astronomicheskiĭ Zhurnal, Vol. 78, No. 7, 2001, pp. 579–584.

Magnetic Fronts in Galaxies

A. P. Petrov[1], D. D. Sokoloff [2], and D. L. Moss[3]

[1]*Russian University of Peoples' Friendship, Moscow, Russia*
[2]*Moscow State University, Moscow, Russia*
[3]*University of Manchester, Manchester, England*

Received October 18, 2000

Abstract—Magnetic-field reversals observed in the Milky Way at one or more Galactocentric radii are interpreted as long-lived transient structures containing memory of the seed magnetic fields. These magnetic fronts can be described using the so-called no-*z* approximation for the nonlinear, mean-field dynamo equations, which are the topic of the paper. We obtain asymptotic estimates for the speed of propagation of discontinuities in the solution (internal fronts). These estimates agree well with numerical solutions of the no-*z* equations, and support our interpretation of the magnetic-field reversals as long-lived transients. *© 2001 MAIK "Nauka/Interperiodica".*

1. INTRODUCTION

The large-scale magnetic fields of spiral galaxies appear to result from the action of the galactic dynamo, driven by the differential rotation of the galactic disk and the helicity of the interstellar turbulence. The azimuthal component of the galactic magnetic field is dominant. In the Milky Way, however, the azimuthal component reverses between the Orion and Sagittarius arms, and there may be additional reversals ([1], see [2] for a discussion of the current state of this problem and the possibility of observing reversals in external galaxies).

One possible explanation of the field reversals is the following. Let us suppose that, by chance, the seed magnetic field has a reversal somewhere between Galactocentric radii r_1 and r_2. In the nonlinear stage of magnetic-field evolution, a magnetic front with sharp field reversals appears somewhere between r_1 and r_2. We identify the front with this reversal. The front moves slowly in the Galactic disk, and the estimates of [3] show that its lifetime can be on the order of the age of the Galaxy.

However, some of the estimates in [3] require detailed information about the vertical structure of the Galactic disk, while observations mainly provide information about the properties of the magnetic field and turbulence averaged over a vertical cross section of the disk. Fortunately, the galactic dynamo equations can be presented in a form known as the no-*z* model, which focuses attention on the field structure in the galactic plane and ignores structure in the vertical direction ([4], see also [5]).

The no-*z* model appears to be very robust and quite adequate for making comparisons with most observations (see [6]). However, until now, it has been considered in the context of the particular physical problem of the galactic dynamo (see e.g. [3, 5]), and its mathematical properties have not been discussed systematically. Such a discussion is the aim of this paper. Based on our analysis, we demonstrate that estimates for the lifetimes of a magnetic front obtained in [3] are robust and do not depend on the detailed vertical structure of the galaxy.

2. EQUATIONS, GENERATION MECHANISM, AND EQUILIBRIUM SOLUTION

We consider a galactic disk of radius R and uniform semi-thickness h. The equations of the no-*z* model for the azimuthal (B_ϕ) and radial (B_r) components of an axisymmetric magnetic field averaged over the vertical cross section of the galactic disk are

$$\frac{\partial B_r}{\partial t} = -R_\alpha \alpha(|\mathbf{B}|)B_\phi - B_r + \lambda^2 \frac{\partial}{\partial r}\left[\frac{1}{r}\frac{\partial}{\partial r}(rB_r)\right],$$
$$\frac{\partial B_\phi}{\partial t} = R_\omega G B_r - B_\phi + \lambda^2 \frac{\partial}{\partial r}\left[\frac{1}{r}\frac{\partial}{\partial r}(rB_\phi)\right]. \quad (1)$$

Here, $G = r\partial\Omega/\partial r$, where $\Omega(r)$ is the rotation law, $R_\alpha = \alpha_0 h/\eta$ and $R_\omega = \Omega_0 h^2/\eta$ are dimensionless numbers specifying the amplitudes of the helicity and differential rotation, respectively, where α_0 and Ω_0 are representative values of α and Ω, and $\lambda = h/R$ is the disk aspect ratio. The $-B_r$ and $-B_\phi$ terms in the first and second equations of (1) approximate the (dominant) diffusion term perpendicular to the galactic disk. We allow the dynamo to be saturated via α quenching:

$$\alpha(|\mathbf{B}|) = \alpha(B_\phi) = \alpha_0 f(gB_\phi^2), \quad (2)$$

where α_0 is chosen such that $f(0) = 1$, $g = 1/B_0^2$, and B_0 is the characteristic magnetic-field strength at which nonlinear effects in the dynamo become important. More generally, as in Eqs. (1), α will depend on the

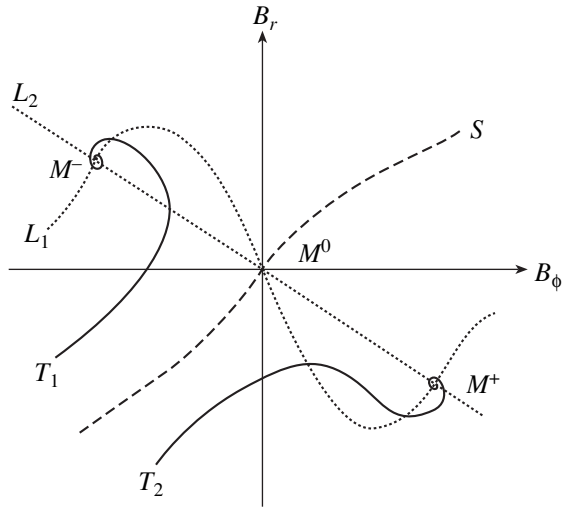

The phase plane of the dynamical system (3): trajectories are attracted to the states M^+ and M^- (for notation, see the text).

strength of the *total* field **B**, but for analytical convenience we take the simpler form (2). In the $\alpha\omega$ approximation (used here), $|\mathbf{B}| \approx B_\phi$, and the differences between these forms for α quenching are small. The function f is usually thought to decay with B_ϕ^2, to provide negative feedback on the magnetic-field generation.

If the seed magnetic field is sufficiently smooth and remains smooth during the subsequent field evolution, the radial diffusion terms in Eqs. (1) can be neglected, yielding

$$\frac{dB_r}{dt} = -R_\alpha\alpha_0 f(gB_\phi^2)B_\phi - B_r, \qquad \frac{dB_\phi}{dt} = R_\omega G B_r - B_\phi. \tag{3}$$

Note that r can be considered a parameter in Eqs. (3).

We begin with the kinematic problem, neglecting nonlinear terms and looking for a separable solution of the form $B_r(r, t) = b_r(r)e^{\gamma t}$, $B_\phi = be^{\gamma t}$. This eigenvalue problem has the solution

$$\gamma(r) = -1 + \sqrt{-D\alpha_0 G}, \quad b(r) = \gamma(r), \qquad b_r(r) = R_\alpha\alpha_0. \tag{4}$$

The excitation conditions are $G < 0$ and $D > D_{\rm cr} = \min(\alpha_0 G)^{-1}$, which is in qualitative agreement with the corresponding result for the complete mean-field equations, namely $D_{\rm cr} \approx 8$ (e.g., [7]). Phillips [8] established a close correspondence between no-z and asymptotic solutions, and suggested a correction factor to be inserted in the no-z formulation that largely removes the quantitative disagreement. If we insert this factor here, the $-B_r$ and $-B_\phi$ terms in (3) are each multiplied by $\pi^2/4$, and so $D_{\rm crit} \approx 6$.

A one-component asymptotic analysis ([7], see also [3, 9]) supposes that the field has the form

$$B_r(t, r) = e^{\Gamma t}Q(r)b_r(r), \quad B_\phi(r, t) = e^{\Gamma t}Q(r)b, \tag{5}$$

where $Q(r)$ can be obtained by solving the equation

$$\Gamma Q = \gamma(r)Q + \lambda^2\left[\frac{1}{r}(rQ)'\right]', \tag{6}$$

which coincides with the asymptotic expansion in [7]. In the nonlinear generalization of (6) [10], $\gamma(r)$ is replaced by the nonlinear term $\gamma(r, Q)$. In contrast, dealing with the no-z model, we introduce nonlinearity into Eqs. (1) directly.

We now turn to the nonlinear properties of the no-z model. Let us consider the steady-state problem for Eqs. (3):

$$R_\alpha\alpha_0 f(gB_\phi^2)B_\phi + B_r = 0, \quad R_\omega G B_r - B_\phi = 0. \tag{7}$$

Equations (7) has the trivial solution $B_r = 0$, $B_\phi = 0$ (denoted below as M^0 in the (B_ϕ, B_r) plane) and, if the magnetic-field generation is strong enough, there are two nontrivial solutions:

$$B_\phi^\pm = \pm\sqrt{\frac{k(r)}{g(r)}}, \quad B_r^\pm = \pm\frac{1}{R_\omega G}\sqrt{\frac{k(r)}{g(r)}},$$

denoted below as $M^\pm$. Here, $k(r)$ means the nonvanishing positive root of the equation

$$1 + DG\alpha_0 f(gB_\phi^2) = 0 \tag{8}$$

(if the root does not exist, then neither do the nontrivial solutions; if several roots exist, we mean the smallest one).

If the solutions $B_\phi^\pm$, $B_r^\pm$ exist, then they are stable and the solution B_ϕ^0, B_r^0 is unstable. If, as usual, $G < 0$, B_ϕ and B_r for the nontrivial equilibrium solution have opposite signs.

For the supercritical dynamo, direct calculation shows that M^0 is a saddle point, and $M^\pm$ are stable focal points if $|\alpha_0 DG| > 2$ or stable nodal points if $|\alpha_0 DG| \le 2$. Thus, the solution for the field tends to a stable point through oscillatory states if the field generation is strong enough and monotonically if the generation is weaker.

We present in the figure the phase portrait for Eqs. (3) for the oscillatory case. The curves L_1, L_2 represent the functions $B_r = -R_\alpha\alpha_0 f(gB_\phi^2)B_\phi$, $B_r = \dfrac{1}{R_\omega G}B_\phi$, respectively. The trajectories of system (3) are vertical when crossing the curve L_2 and horizontal when crossing the curve L_1. Some typical trajectories are denoted T_1 and T_2.

The trajectories in the "southeast" ("northwest") half-plane are attracted to M_1 (M_2). The separatrix S is given by

$$\frac{dB_r}{dB_\phi} = \frac{R_\alpha \alpha_0 g B_\phi^2 B_\phi + B_r}{-R_\omega G B_r + B_\phi}, \quad (9)$$

with the initial conditions $B_r = 0$, $B_\phi = 0$ (more accurately, $B_r \longrightarrow 0$ when $B_\phi \longrightarrow 0$).

The solution of (9) for small B_r and B_ϕ—i.e., for a weak seed field—is given by

$$B_r = \sqrt{-\frac{R_\alpha \alpha_0}{R_\omega G}} B_\phi + f'(0)\frac{R_\alpha \alpha_0 g}{4\sqrt{-\alpha_0 DG} + 2} B_\phi^3 + O(B_\phi^5). \quad (10)$$

Let us now consider the seed field $B_\phi(r)$, $B_r(r)$ as a curve $L(r)$ in the (B_ϕ, B_r) plane. If the seed field at a given radius is located "northwest" of the separatrix (10) in this plane, then the equilibrium state is B_ϕ^+, B_r^+, and it is B_ϕ^-, B_r^- otherwise.

If the curve L intersects the separatrix S at a radius r^*, then, at the beginning of the nonlinear stage of evolution, the magnetic field has different signs for $r < r^*$ and $r > r^*$, and so a sharp structure arises near r^*. Below, we consider the evolution of such sharp structures, which can be stationary or travelling.

3. STATIONARY SHARP STRUCTURES

We normalize the steady-state solutions of (1) by writing

$$u = B_r/B_r^+, \quad v = B_\phi/B_\phi^+, \quad (11)$$

giving

$$\lambda^2 u'' = u - \mathcal{D} f(k v^2) v - \lambda^2 u' \Phi(r), \quad (12)$$

$$\lambda^2 v'' = v - u - \lambda^2 v' \Psi(r). \quad (13)$$

Terms of order λ^2 have been omitted and we have defined $\mathcal{D} = -D\alpha_0 G > 0$,

$$\Phi(r) = \frac{k'}{k} - \frac{g'}{g} - \frac{2G'}{G} + \frac{1}{r}, \quad \Psi(r) = \frac{k'}{k} - \frac{g'}{g} + \frac{1}{r}.$$

A sharp structure is expected to contain a front domain in which the first and second radial derivatives are of order λ^{-1} and λ^{-2}, respectively. Outside this domain, the radial derivatives are expected to be of order λ^0. According to the boundary function method [11], the asymptotic solution can be presented as a combination of a smooth solution, denoted by barred quantities below, and a component intrinsic to the front, indicated by the prefix Π:

$$u = \bar{u}_0(r) + \Pi_0 u(\tau) + \lambda(\bar{u}_1(r) + \Pi_1 u(\tau)),$$
$$v = \bar{v}_0(r) + \Pi_0 v(\tau) + \lambda(\bar{v}_1(r) + \Pi_1 v(\tau)). \quad (14)$$

Here, $\tau = (r - r_0)/\lambda$ is a stretched variable and r_0 is a stable reversal point (terms up to order λ are presented). The smooth part of expansion (14) approximates the solution where $|r - r_0| \sim \lambda^0$, while the boundary functions are introduced to make the expansion valid when $r \approx r_0$. The boundary functions must decrease rapidly (usually exponentially).

Substituting (14) into (12) and equating terms of order λ^0, we obtain $\bar{u}_0 = \bar{v}_0 = \pm 1$, or $\bar{u}_0 = \bar{v}_0 = 0$. For a front solution, we set $\bar{u}_0 = \bar{v}_0 = -1$ for $r < r_0$ and $\bar{u}_0 = \bar{v}_0 = 1$ for $r > r_0$. Equating terms of order λ^1, we obtain $\bar{u}_1 = \bar{v}_1 = 0$.

We introduce the continuous function of zeroth approximation $\tilde{u}(\tau) = -1 + \Pi_0 u(\tau)$ for $\tau < 0$, $\tilde{u}(\tau) = 1 + \Pi_0 u(\tau)$ for $\tau > 0$, $\tilde{v}(\tau) = -1 + \Pi_0 v(\tau)$ for $\tau < 0$, $\tilde{v}(\tau) = 1 + \Pi_0 v(\tau)$ for $\tau > 0$.

Equating terms of λ^0 in Eqs. (12), we obtain

$$\tilde{u}'' = \tilde{u} - \mathcal{D}_0 f(k_0 \tilde{v}^2)\tilde{v}, \quad \tilde{v}'' = \tilde{v} - \tilde{u}, \quad (15)$$

where $\tilde{u}(+\infty) = \tilde{v}(+\infty) = 1$, $\tilde{u}(-\infty) = \tilde{v}(-\infty) = -1$, and $\mathcal{D}_0 = \mathcal{D}(r_0)$, $k_0 = k(r_0)$.

To obtain the condition for a point r_0 to be a stationary point for a sharp structure, we multiply the first equation in (15) by $\tilde{v}'$ and the second equation by $\tilde{u}'$, integrate both equations over τ from $-\infty$ to $+\infty$, and add the results to obtain the identity

$$\mathcal{D}_0 \int_{-\infty}^{+\infty} \tilde{v} f(k_0 \tilde{v}^2)\tilde{v}' d\tau + \int_{-\infty}^{+\infty} \tilde{u}\tilde{u}' d\tau = 0. \quad (16)$$

It can be shown that both terms in this condition are identically equal to zero. However, the next order of accuracy (λ^2) gives, after some algebra, the nontrivial condition for a stationary reversal point r_0

$$\int_{-\infty}^{+\infty} (\mathcal{D}_0' f(k_0 \tilde{v}^2)\tilde{v} + \mathcal{D}_0 f'(k_0 \tilde{v}^2) k_0' \tilde{v}^3)\tau \tilde{v}' d\tau + (\Phi_0 + \Psi_0)\int_{-\infty}^{+\infty} u' v' d\tau = 0. \quad (17)$$

Here, $\Phi_0 = \Phi(r_0)$ and $\Psi_0 = \Psi(r_0)$. We stress that the vicinity of the point r_0 makes a substantial contribution to the left hand side of (17).

If the magnetic-field generation is homogeneous, i.e., $\mathcal{D}$ = const, the condition (17) simplifies to

$$\left(\frac{g'(r)}{g(r)} + \frac{G'(r)}{G(r)} - \frac{1}{r}\right)\Bigg|_{r = r_0} = 0, \quad (18)$$

which is identical with the condition for a stationary sharp structure obtained in [9] for a nonlinear version of Eq. (6).

Table 1

λ	R_ω	D	r	V_f	V_{pred}
0.05	80	800	0.596	−6.43	−7.12
0.05	80	800	0.525	−7.62	−7.71
0.05	100	1000	0.581	−7.12	−7.24
0.05	100	1000	0.500	−7.98	−7.93
0.05	100	1000	0.423	−8.69	−8.56
0.05	150	1500	0.640	−6.69	−6.75
0.05	150	1500	0.574	−7.33	−7.34
0.05	150	1500	0.497	−7.99	−7.96
0.025	60	600	0.667	−1.63	−1.60
0.025	100	1000	0.682	−1.61	−1.61
0.025	100	1000	0.666	−1.77	−1.77

Table 2

λ	R_ω	D	r	V_f	V_{pred}
0.025	100	1000	0.684	−1.41	−1.43
0.025	100	1000	0.574	−1.73	−1.71

4. TRAVELLING SHARP STRUCTURES

If condition (17) is not satisfied, the reversal point begins to move, so the evolution of the sharp structure is governed by the equations

$$\lambda^2 u'' - u_t = u - Hf(kv^2)v - \lambda^2 u'\Phi(r), \qquad (19)$$

$$\lambda^2 v'' - v_t = v - u - \lambda^2 v'\Psi(r). \qquad (20)$$

We anticipate that the sharp structure will have the form (14) of a steady sharp structure [12], however now with $r_0 = R(t)$, where the function $R(t)$ has to be determined. Thus,

$$\frac{\partial u}{\partial t} = -\tilde{u}'\frac{1}{\lambda}\frac{dR}{dt}, \quad \frac{\partial v}{\partial t} = -\tilde{v}'\frac{1}{\lambda}\frac{dR}{dt}. \qquad (21)$$

Integrating Eqs. (19) and (20) over r, using (21), and then adding, we obtain after some algebra

$$\frac{dR}{dt} = -\lambda^2\left\{\frac{k'(R)}{k(R)} - \frac{g'(R)}{g(R)} - \frac{G'(R)}{G(R)} + \frac{1}{R}\right.$$

$$+\frac{1}{2}\left[\int_{-\infty}^{+\infty}(\tilde{u}^2 - \tilde{u}\tilde{v})d\tau\right]^{-1}\left[-\frac{1}{2}\left(\frac{\mathcal{D}(R)}{k(R)}\right)'\int_{-\infty}^{+\infty}F(k(R)\tilde{v}^2)d\tau\right.$$

$$\left.\left.-\frac{\mathcal{D}(R)k'(R)}{2k(R)}\int_{-\infty}^{+\infty}(\tilde{v}^2 f(k(R)\tilde{v}^2) - f(k(R)))d\tau\right]\right\},$$

where $F(t) = \int_k^t f(x)dx$.

When $\mathcal{D}$ = const, we have k = const, and deduce

$$\frac{dR}{dt} = \lambda^2\left[\frac{g'(R)}{g(R)} + \frac{G'(R)}{G(R)} - \frac{1}{R}\right]. \qquad (22)$$

Equation (22) should be compared with the result of [3], which was obtained for (6) with the nonlinearity

$$\gamma(r, Q) = \gamma_0(1 - gQ^2). \qquad (23)$$

That paper derived the result

$$\frac{dR}{dt} = \lambda^2\left[\frac{g'(R)}{g(R)} - \frac{\gamma_0'(R)}{\gamma_0(R)} - \frac{1}{R}\right]. \qquad (24)$$

In the case of homogeneous field generation, the predictions of (24) and (22) coincide.

In the general case, the results (24) and (22) have similar structures, although they depend on slightly different quantities (G on the one hand, and γ_0, on the other). We conclude that the asymptotic approach based on (6) and the no-z model give slightly different predictions for the velocity of front propagation. However, the disagreement between the two predictions is negligible from a practical point of view.

5. COMPARISON WITH NUMERICAL SOLUTIONS

The above conclusion is supported by the numerical simulations of [3]. However, predictions of the no-z model were not directly compared with numerical results in [3]. Here, we present such a comparison. We use a Brand rotation curve (cf. [3])

$$\Omega = \frac{\Omega_0}{\left(1 + \left(\frac{r}{r_\omega}\right)^2\right)^{1/2}} \qquad (25)$$

with $r_\omega = 0.2$, and take $R_\alpha = 10$; the value of R_ω, and hence that of D, is varied. The computations begin with a discontinuity in the seed field at $r = 0.7$. The front position is determined by the zero of B_ϕ; using the zero of B_r does not make a significant difference. For larger values of D and/or smaller values of λ, the front is steep. The front velocities V_f (multiplied by a factor 10^3) at a given position r for homogeneous α quenching are given in Table 1, in comparison with the front velocity V_{pred} predicted by (22).

When the α quenching is inhomogeneous, with $g(r) = (1 + r(1 - r))^{-1}$, we obtain the results in Table 2.

We conclude that the agreement between the asymptotic and numerical results is quite satisfactory, even when the condition of applicability of (22), i.e., $\mathcal{D}$ = const, is not formally satisfied.

6. DISCUSSION

The above results confirm that the no-*z* model gives stable results that are in reasonable agreement with other simplified models for the galactic dynamo. The results of these models are in agreement even if they are extrapolated somewhat outside the formal area of the applicability of the approximations. This implies that predictions of galactic dynamo theory are very robust, unless some new physics (for example, non-circular velocities, [13]) is included.

Because of analytical difficulties, we were unable to obtain explicit asymptotic expressions for the propagation of external fronts in the no-*z* approximation. Our experience here with internal fronts, and also comparison with the numerical results of [3] for both internal and external fronts, increase our confidence in the suitability of extending the result of Eqs. (11) in [3] to the no-*z* model.

ACKNOWLEDGMENTS

This work was supported by NATO (grants CRG153095, PST.CLG974737) and the Russian Foundation for Basic Research (project codes 00-02-17854, 99-01-01208).

REFERENCES

1. M. Simard-Normandin and P. P. Kronberg, Astrophys. J. **242**, 74 (1980).
2. R. Beck, Space Sci. Rev. (2001) (in press).
3. D. Moss, A. Petrov, and D. Sokoloff, Geophys. Astrophys. Fluid Dyn. **92**, 129 (2000).
4. D. Moss, Mon. Not. R. Astron. Soc. **285**, 191 (1995).
5. K. Subramanian and L. Mestel, Mon. Not. R. Astron. Soc. **265**, 649 (1993).
6. R. Beck, A. Brandenburg, and D. Moss, Annu. Rev. Astron. Astrophys. **34**, 155 (1996).
7. A. A. Ruzmaikin, A. M. Shukurov, and D. D. Sokoloff, *Magnetic Fields of Galaxies* (Kluwer, Dordrecht, 1988).
8. A. Phillips, Geophys. Astrophys. Fluid Dyn. **94**, 135 (2001).
9. M. P. Belyanin, D. D. Sokoloff, and A. M. Shukurov, Russ. J. Math. Phys. **2**, 149 (1994).
10. A. Poezd, A. Shukurov, and D. Sokoloff, Mon. Not. R. Astron. Soc. **264**, 285 (1993).
11. A. B. Vasil'eva and V. F. Butuzov, *Asymptotic Methods in the Theory of Singular Perturbations* [in Russian] (Vysshaya Shkola, Moscow, 1990).
12. A. P. Petrov, Zh. Vychisl. Mat. Mat. Fiz. **39**, 1513 (1999).
13. D. Moss, A. Shukurov, and D. Sokoloff, Astron. Astrophys. **358**, 1142 (2000).

Translated by A. Petrov

Astronomy Reports, Vol. 45, No. 7, 2001, pp. 502–509. Translated from Astronomicheskiĭ Zhurnal, Vol. 78, No. 7, 2001, pp. 585–593.

A Correlation between the Distributions of Pulsars and Emission Measures in the Galaxy

A. V. Pynzar' and V. I. Shishov

Pushchino Radio Astronomy Observatory, Pushchino, Moscow oblast, Russia

Received December 27, 1999

Abstract—A correlation has been detected between the volume density of pulsars and the density of interstellar ionized gas on scales of more than 500 pc in Galactic longitude and 200 pc in Galactic latitude. On smaller scales, the correlation is present only for pulsars with ages less than 60000 years, which are located predominantly near supernova remnants and H II regions. This all indicates that pulsars are born in regions with high concentrations of interstellar gas. The minimum emission measures observed in the directions toward pulsars are inversely proportional to the pulsar ages. It is concluded that the ionized gas in the vicinities of a number of pulsars was formed during supernova explosions, and corresponds to Strömgren zones. The ionization of the gas in these zones requires a radiation energy on the order of 10^{50}–10^{51} erg. © *2001 MAIK "Nauka/Interperiodica".*

1. INTRODUCTION

It is usually thought that pulsars form as the result of the evolution of massive early-type stars, which are born in dense molecular clouds. This suggests that we should expect the volume density of pulsars to be correlated with the concentration of interstellar gas. The dependence of the emission measures EM on the dispersion measures DM of pulsars is presented in [1]; the dependence of pulse broadening τ on EM is considered in [2]. A preliminary analysis of these dependences suggested that the number of pulsars in a fixed interval of emission measure depended only weakly on the magnitude of EM. This means that the number density of pulsars on the celestial sphere grows with the emission measure, since the fraction of the celestial sphere occupied by gas with a given EM decreases as the emission measure increases. Consequently, pulsars are concentrated toward gas complexes with large electron densities N_e.

Here, we investigate in more detail the relation between the density of the interstellar gas and the volume density of pulsars. However, since it is rather difficult to measure the gas density, we consider here the correlation between the volume density of pulsars and the emission measure EM. Since the emission measure is proportional to the square of the electron density N_e, it is a very good parameter to use when searching for correlations between the volume density of pulsars and the density of the interstellar medium.

2. DEPENDENCE OF THE SPACE DENSITY OF PULSARS ON EMISSION MEASURE

Since the volume density of pulsars is difficult to measure, but is proportional to the surface density of pulsars on the celestial sphere *N*/*S*, we considered the dependence of *N*/*S* on emission measure EM, where *N* is the number of pulsars in a particular area of sky with area *S* (in square degrees). We used the catalog of 558 pulsars [3] supplemented by 148 pulsars from [4].

We obtained data on emission measures in the Galaxy from measurements of the intensity of the Galactic background in the radio at 5 and 10 GHz [5–8], in the optical Hα line [9–12], in the infrared at 60 μm, and in the H166α hydrogen recombination line [14–16]. The technique used to derive the emission measures from these data is described in [17] and references therein. The values of EM in the directions of the pulsars were primarily derived using measurements of the thermal background at 5 and 10 GHz, for which the telescope beam sizes were from 2.6 to 4 arcminutes [5–7].

We used these data to construct contours of emission measure EM for the entire Galaxy (as functions of latitude and longitude). We then divided the entire range of EM values into several intervals, such that the emission measure varied by about a factor of two within each interval. This manner of dividing the entire range was dictated by the need to ensure there was a sufficient number of pulsars in each interval of EM and also by the discrete character of the EM contours.

In each interval of EM contours, we counted the number of pulsars *N* observed in the directions of the corresponding EM values, then measured the area (in square degrees) enclosed by the contours corresponding to the given EM interval. The values of *N*/*S* are plotted as a function of EM in Fig. 1. Note that the values EM = 40–180 pc/cm^6 were joined into one interval instead of two. This was necessitated by the fact that there are few observational data in this interval, since EM values greater than 40 pc/cm^6 are observed at Galactic latitudes lower than 5°, where optical data are

1063-7729/01/4507-0502$21.00

distorted by interstellar absorption, and radio data on the thermal background and recombination lines are available only for latitudes lower than 1°, where EM > 200 pc/cm^6.

We can see in Fig. 1 that N/S grows with EM roughly in accordance with a power law right to EM ~ 1000 pc/cm^6, after which N/S becomes constant. This dependence can be fitted by

$$N/S = \begin{cases} 0.1\ (\mathrm{EM}/100\ \mathrm{pc/cm^6})^{0.6}\ (\mathrm{deg})^{-2} \\ \mathrm{EM} < 10^3\ \mathrm{pc/cm^6} \\ 0.4\ (\mathrm{deg})^{-2}, \quad \mathrm{EM} > 10^3\ \mathrm{pc/cm^6}. \end{cases} \quad (1)$$

We can see that there is undoubtedly a relation between the volume density of pulsars n_* and the density of the ionized gas. Relation (1) corresponds roughly to a linear dependence of n_* on N_e:

$$n_* \propto N_e. \quad (2)$$

The question arises of why the relation between N/S and EM ceases to be apparent at large emission measures. Values EM > 1000 pc/cm^6 are observed at Galactic latitudes lower than 1°, in the directions of spiral arms. The mean angular scales of formations with such emission measures are about 2° in latitude and about 5° in longitude, which, for distances from the Sun of about 5 kpc, corresponds to linear scales of about 200 pc in latitude and 500 pc in longitude. The simultaneous absence of a correlation between N/S and EM on scales smaller than 200 pc in latitude and 500 pc in longitude and presence of such a correlation on larger scales can be explained as follows.

Pulsars are old objects and can move far from the place of their birth during their lifetimes. For example, at a speed of about 100 km/s, a pulsar can travel a distance of 100 pc over 10^6 yr. However, even if pulsars had low velocities and were not able to travel as far from the places of their births during their lifetimes, we would not necessarily expect a correlation between N/S and EM, since the H II regions ionized by the hot, massive stars that were the progenitors of these pulsars would no longer be visible. The material in an H II region that ceases to be irradiated by a source of ionization recombines on a timescale of about $10^5/N_e$ yr [18], where N_e is the electron density. In this case, there should not be a correlation between young pulsars and H II regions.

To test the hypothesis that pulsars have left compact regions of ionized gas with EM > 1000 pc/cm^6, we studied the near neighborhoods of all formations in the Galactic plane with EM > 1000 pc/cm^6, in order to look for a dependence of the number of pulsars in the vicinity of an H II region on its EMission measure and the mass of gas it contains. We counted the number of pulsars N in circles with radii of 1.5° and 3° centered on the H II regions. We found no evidence of a correlation between N and EM. We then measured the angular sizes in degrees φ of compact thermal regions at the half-intensity level and computed for each such region the value of $T_B * \varphi^4$, which is proportional to the square of the mass of ionized gas in the region (T_B is the brightness temperature in the center of the region.) Likewise, we found no correlation between N and $T_B * \varphi^4$ for circular regions with radii 1.5° and 3° surrounding the centers of the H II regions. Consequently, compact H II regions with emission measures EM > 1000 pc/cm^6 are not long-lived regions that continuously give birth to pulsars.

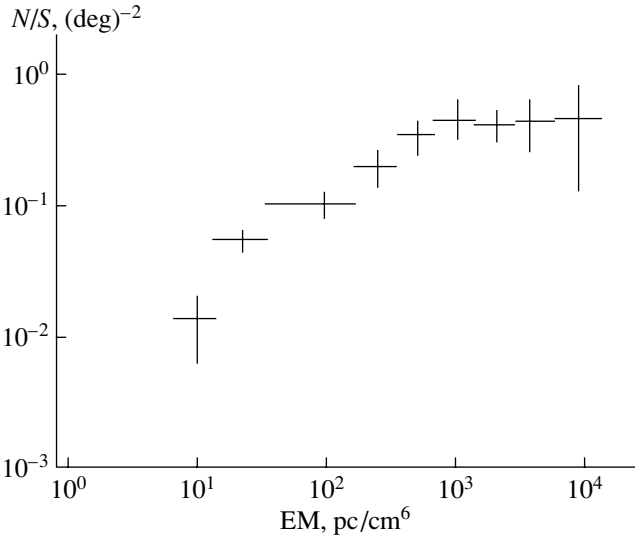

Fig. 1. Dependence of the number density of pulsars on the celestial sphere N/S on the emission measure EM in the direction of the pulsars.

3. RELATION BETWEEN EMISSION MEASURE AND PULSAR AGE

To verify the hypothesis that the lifetimes of compact H II regions are much shorter than the lifetimes of pulsars, we must test for a correlation between young pulsars and H II regions. With this aim, we searched for a relation between the ages of pulsars and the emission measures in the directions toward them. The results are shown in Fig. 2, where the horizontal axis plots pulsar age T (in years) and the vertical axis plots the emission measure EM in the area of sky onto which the pulsar is projected. We can see that, at young ages, there is a deficit of pulsars at small emission measures, while, at ages greater than 10^6 yr, the distribution of pulsars with emission measure is fairly uniform. At ages below 10^6 yr, we can clearly see a lower envelope for the plotted points, which can be approximated by the relation

$$\mathrm{EM_{min}} = 10^7/(\mathrm{yr}\ T\ \mathrm{pc\ cm^6}). \quad (3)$$

It is possible that $\mathrm{EM_{min}}$ = const for $T < 10^4$ yr.

The concentration of young pulsars in areas with high emission measures indicates that these pulsars

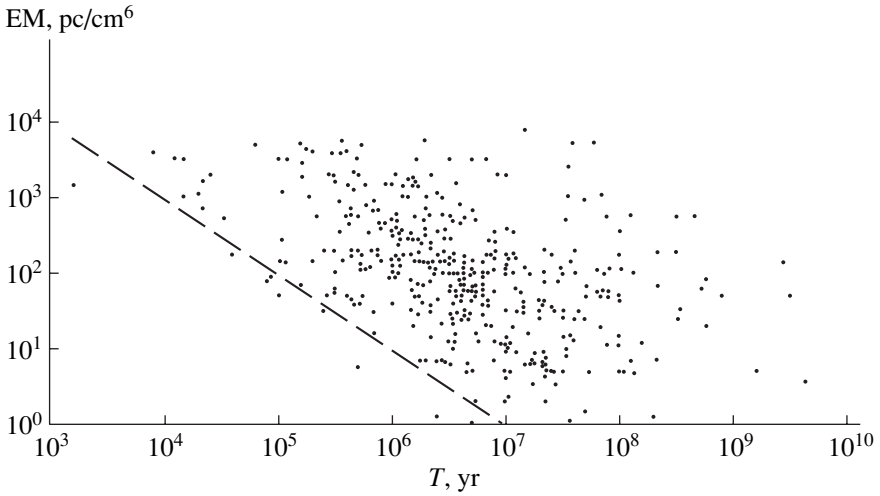

Fig. 2. Dependence of the emission measure EM of the Galactic background in the directions of pulsars and the pulsar ages *T*.

were born in regions with high-density interstellar gas EM > 10^3 pc/cm^6. The table presents data for young pulsars located within 1° (except for the pulsar 0833-45) of the centers of supernova remnants [19, 20] and H II regions [21–25]. The columns give (1) the pulsar's name, (2) its Galactic coordinates (longitude *l* and latitude *b*), (3) the logarithm of its age (in years), (4) the name of the supernova remnant or H II region, (5)–(6) their Galactic coordinates and mean angular diameter (in arcminutes), and (7) the angular distance of the pulsar from the center of the supernova remnant or H II region in longitude and latitude, respectively.

Our analysis showed that, of the 18 pulsars with ages less than 60000 yr, 11 are located less than 0.7° and 8 less than 0.4° from the centers of H II regions (table). Thirteen of the pulsars in the table are located less than 0.9°, 10 less than 0.5°, and 7 less than 0.1° from the centers of supernova remnants. The positions of young pulsars near supernova remnants and H II regions appears to confirm that they were born in regions with a high concentration of interstellar gas. Figure 2 shows that the ionized interstellar gas undoubtedly evolves with time, and that the characteristic evolution time of an ionized-gas complex is less than that for clusters of pulsars. Accordingly, the disappearance of a correlation between the number density of pulsars and emission measure at high emission measures is associated with such evolution. Below, we analyze in more detail regions of ionized gas with high emission measures.

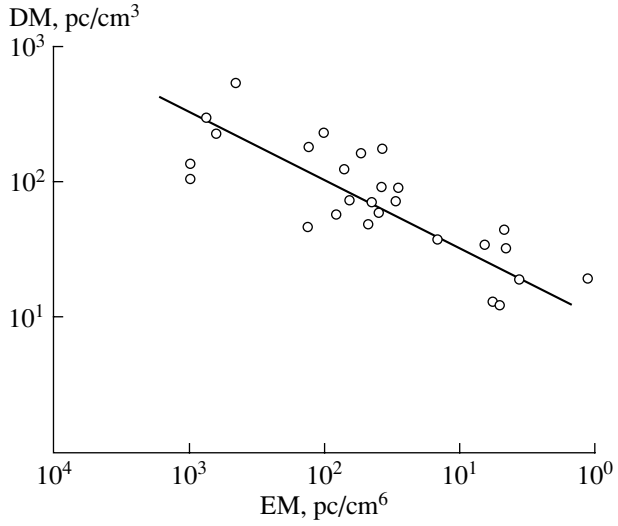

Fig. 3. Dependence of the dispersion measures of pulsars DM and the emission measures EM in the direction of these pulsars for pulsars near the lower envelope in Fig. 2.

4. EVOLUTION OF THE STRÖMGREN ZONE OF A SUPERNOVA

The limiting emission measures EM_{min} described by relations (3) are determined by regions of ionized gas, which are undoubtedly associated with pulsars. This statement is supported by the following arguments. First, a region with such emission measures must be associated with each pulsar; otherwise, we would observe EM values below the envelopes (3). Second, the clear link between the evolution of the minimum emission measure EM_{min} and the age of the pulsar provides evidence that the pulsar and region of ionized gas were born simultaneously. To investigate the structure of the ionized gas, we separated pulsars in the boundary area near relations (3) and determined their dispersion measures DM_{min}. We then constructed a plot of DM_{min} as a function of EM_{min}, shown in Fig. 3. The solid curve in this figure shows the relation

$$DM = 300(EM/1000\ pc/cm^6)^{0.5}\ pc/cm^3. \quad (4)$$

We will derive the size of the region of ionized gas created by the supernova explosion L and the electron density N_e in this region from the relations

$$L_{\min} = (2\mathrm{DM})^2/\mathrm{EM},$$
$$N_{e,\min} = \mathrm{EM}/2\mathrm{DM}. \quad (5)$$

When estimating EM, we took the background electron temperature to be $T_e = 6000$ K [17]; however the ionizing radiation during a supernova explosion (or during radiative cooling of the supernova shell) should have a temperature of $T_e = 10^6$ K [26, 27]. To determine the EM values, we primarily used measurements of the background brightness temperature T_B at the high frequencies of 5 GHz [5, 6, 8] and 10 GHz [7], where the interstellar medium is optically thin. In this case, $T_B \propto T_e^{-0.35}$ EM. An increase in the temperature by a factor of 166 leads to an increase in the EM by a factor of 6.

Therefore, when $T_e = 10^6$ K, relation (4) can be replaced by the expression

$$\mathrm{DM}' = 300(\mathrm{EM}/6000\ \mathrm{pc/cm^6})^{0.5}\ \mathrm{pc/cm^3},$$
$$\mathrm{EM}' = 6\mathrm{EM}, \quad T_e = 10^6\ \mathrm{K}, \quad (4')$$

where the value of EM' corresponds to the estimated emission measure for $T_e = 10^6$ K.

Relations (5) take into account the fact that the pulsar is located at the center of a region of ionized gas, so that the dispersion measure DM is determined by the radius of the region, $L/2$, while EM is determined by the full size (diameter) of the region, L. Substituting (4) into (5) yields

$$L_{\min} = \mathrm{const} \cong 360\ \mathrm{pc},$$
$$N_{e,\min} \cong 1.5\ (\mathrm{EM}/1000\ \mathrm{pc/cm^6})\ \mathrm{cm^{-3}} \cong 1.5\ (10^4/T(\mathrm{yr}))^{1/2}\ \mathrm{cm^{-3}}. \quad (6)$$

With $T_e = 10^6$ K, substituting (4') into (5) yields

$$L_{\min} = \mathrm{const} \cong 60\ \mathrm{pc},$$
$$N_{e,\min} = 10(\mathrm{EM}/6000\ \mathrm{pc/cm^6})^{1/2}\ \mathrm{cm^{-3}} \cong 10\ (10^4/T(\mathrm{yr}))^{1/2}\ \mathrm{cm^{-3}}. \quad (6')$$

We can see that the size of the region is preserved, whereas the electron density in the region decreases with time. The large size of the region and the fact that it remains constant make it impossible to identify this ionized gas with a supernova remnant. The only object with which we can identify this type of gas complex is the Strömgren zone formed by the supernova. Such a Strömgren zone surrounds every sufficiently young pulsar, and determines the minimum emission measure that is observed in the direction of that pulsar.

5. EVOLUTION OF THE GAS COMPLEX

Above, we considered the evolution of a single zone of ionized gas associated with a supernova explosion. However, most pulsars are projected onto regions with $\mathrm{EM} \gg \mathrm{EM}_{\min}$. To analyze the properties of these regions, we divided the observational data in Fig. 1 into four subsets corresponding to the pulsar-age intervals $T < 10^5$ yr, 10^5 yr $< T < 10^6$ yr, 10^6 yr $< T < 10^7$ yr, and 10^7 yr $< T < 10^8$ yr. Figure 4 presents the dependences of N/S on EM for these intervals, which can be approximated by the analytical formula

$$N/S = (N/S)_{\max}[\mathrm{EM}/\mathrm{EM}_0]^n, \quad \mathrm{EM} < \mathrm{EM}_0,$$
$$N/S = (N/S)_{\max}, \quad \mathrm{EM} > \mathrm{EM}_0. \quad (7)$$

Figure 5 shows the time evolution of $(N/S)_{\max}$, EM_0, and $\mathrm{EM}_{\min}$. We can see that EM_0 decreases as T increases, and that this decrease is slower than the decrease in $\mathrm{EM}_{\min}$. The characteristic time for evolution of EM_0 is $T_{\mathrm{char,\,EM}} \cong 10^6$ yr. We cannot relate this ionized gas to a single Strömgren zone. It may be associated with a gas complex in which a series of supernova explosions occurred over a period of about a million years.

The value of $(N/S)_{\max}$ also decreases with time, on a characteristic timescale of $T_{\mathrm{char},\,N/S} \cong 10^7$ yr. This time can be associated with the timescale for the departure of the pulsars from the region of their birth after the end of the period of supernova explosions.

6. DISCUSSION

Thus, we can explain our data as follows. A series of supernova explosions occurs in a gas complex about 0.5 kpc in size over a period of about a million years. An explosion that occurs outside the boundary of the complex gives rise to a solitary Strömgren zone. Further, this zone evolves and determines $\mathrm{EM}_{\min}$. Using the zone parameter estimates determined by (6), we can estimate the energy required to ionize the gas in the zone:

$$E_{\mathrm{ioniz}} \cong 10^{52}\ \mathrm{erg}. \quad (8)$$

Naturally, this is also an estimate of the ionizing radiation emitted during the supernova explosion. This energy is somewhat higher than the energy of the shell of the supernova remnant ($\cong 10^{51}$ erg) [26]. However, if we adopt $T_e = 10^6$ K, we obtain

$$E_{\mathrm{ioniz}} \cong 7 \times 10^{50}\ \mathrm{erg}. \quad (9)$$

Note that the estimate (9) was obtained for a very simple model for the distribution of the medium, in the form of a uniform sphere with diameter $L_{\min}$, and is accurate only to order of magnitude. Taking into account a more realistic distribution for the medium along the line of sight could appreciably change this estimate. First and foremost, estimates of E_{ioniz} are very sensitive to the

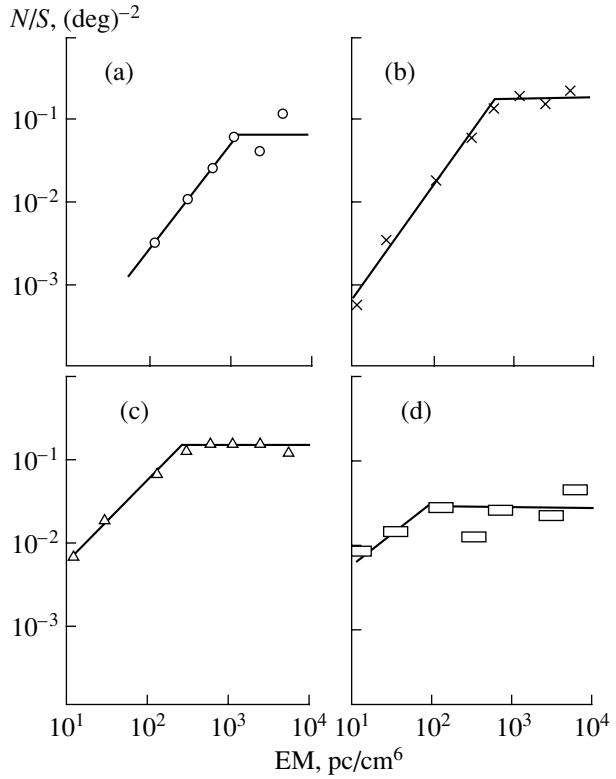

Fig. 4. Dependence of the number density of pulsars on the celestial sphere N/S on the corresponding emission measure EM for various intervals of pulsar age T: (a) $T < 10^5$ yr, (b) 10^5 yr$< T < 10^6$ yr, (c) 10^6 yr $< T < 10^7$ yr, and (d) 10^7 yr $< T < 10^8$ yr.

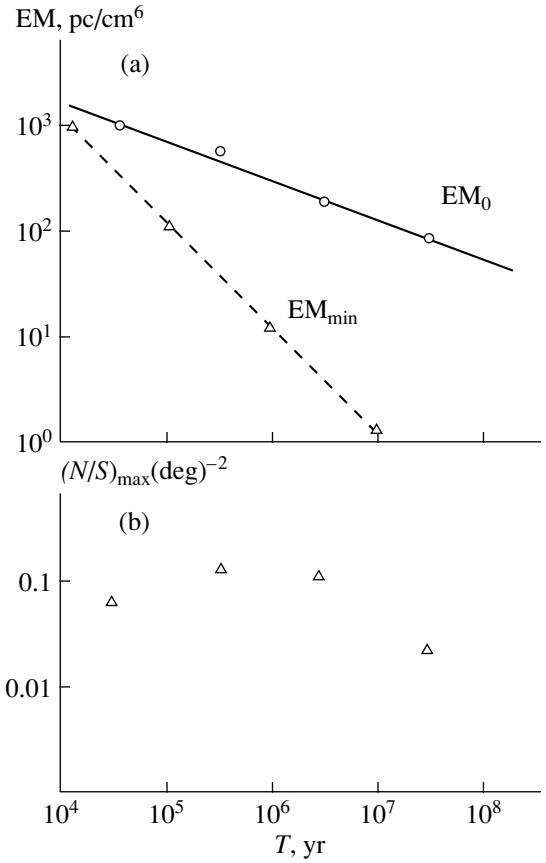

Fig. 5. Evolution of (a) EM_0 and EM_{min} and (b) $(N/S)_{max}$ with time T.

corresponding estimates of DM. In accordance with (5), we can write

$$E_{\text{ioniz}} \propto N_e L^3 \propto \text{DM}^5/\text{EM}^2. \quad (10)$$

The dispersion measure is determined not only by the Strömgren zone, but also by the background medium along the line of sight. The contribution of this background should be excluded when estimating E_{ioniz}. For example, if the contribution of the background to the DM is 20%, allowing for this decreases the energy estimate by a factor of three: $E_{\text{ioniz}} \cong 2 \times 10^{50}$ erg.

It is also known that the medium in the vicinity of a supernova is determined by its previous history, and is likely to be non-uniform and clumpy (see, for example, [28]). This inhomogeneity of the medium is described by parameters such as the filling factor f. In the case of a uniform medium, $f = 1$, whereas $f < 1$ for a non-uniform medium. Introducing a filling factor in (5) increases the estimated value of L and, accordingly, the estimated value of E_{ioniz}. However, if there are variations in the temperature as well as the density, there exist models in which it is possible to lower E_{ioniz}. In particular, the estimated E_{ioniz} can be decreased if there are more compact shells with enhanced density and temperature in the Strömgren zone. Overall, taking into account the inhomogeneity in the distribution of the medium, a more correct estimate of the ionization energy is

$$E_{\text{ioniz}} \cong (10^{50}\text{–}10^{51}) \text{ erg}. \quad (11)$$

The time dependence of the electron density determined by (3) and (6) can be related to the recombination time:

$$T_{\text{rec}} \propto N_e^{-2}. \quad (12)$$

The evolution of the gas in the Strömgren zone can be described as follows. After the supernova explosion, all the gas is ionized. Further, due to the presence of turbulent fluctuations, more dense regions cool more rapidly, and the gas in these regions recombines and is compressed. The freed space is occupied by less dense, hotter gas.

The evolution of the ionized gas in the central regions of the gas complex is more complicated. It is possible that several Strömgren zones in different stages of evolution interact. There is no doubt that we should also take into account the role of supernova remnants in the formation of ionized-gas structures, since, over a million years, supernova remnants can reach sizes of the order of a hundred parsecs.

Table

PSR	l, b	log*T* (yr)	SNR	H II	l, b	2Θ	Δl, Δb
1	2	3	4		5	6	7
1757–24	5.3°–0.9°	4.19	Milne 56		5.3°–1.0°	18'	0° 0.1°
				M8	6.0°–1.2°	8	0.7° 0.3°
				*	5.9°–0.4°	6	0.6° 0.5°
				*	5.5°–0.2°	3	0.2° 0.7°
1758–23	6.8°–0.1°	4.77	W28		6.4°–0.1°	45	0.4° 0°
				M20	7.0°–0.2°	6	0.2° 0.1°
				*	5.9°–0.4°	6	0.9° 0.3°
				*	6.7°–0.2°	5	0.1° 0.1°
				*	6.6°–0.1°	3	0.2° 0°
1800–21	8.4°+0.1°	4.20	W30		8.7°–0.1°	45	0.3° 0.2°
				*	8.1°+0.2°	3	0.3° 0.1°
				*	8.4°–0.3°	4	0° 0.4°
				*	8.7°–0.4°	3	0.3° 0.5°
1823–13	18.0°–0.7°	4.33	Kes 67		18.8°+0.3°	15	0.8° 1°
			*		18.9°–1.1°	33	0.9° 0.4°
				*	18.1°–0.3°	3	0.1° 0.4°
				*	18.2°–0.4°	4	0.2° 0.3°
				*	18.2°–0.3°	7	0.2° 0.4°
				*	18.3°–0.3°	5	0.3° 0.4°
				*	18.3°–0.4°	3	0.3° 0.3°
				*	18.8°–0.5°	8	0.8° 0.2°
				*	18.9°–0.4°	7	0.9° 0.3°
				*	19.0°–0.0°	4	1° 0.7°
1853+01	34.6°–0.5°	4.31	W44		34.7°–0.4°	30	0.1° 0.1°
				*	35.6°–0.0°	6	1° 0.5°
				*	33.9°+0.1°	3	0.7° 0.6°
				*	34.2°+0.1°	3	0.4° 0.6°
				*	35.0° –0.5°	3	0.4° 0°
				*	35.1°–1.5°	6	0.5° 1°
1930+22	57.4°+1.6°	4.60	*		57.3°+1.2°	18	0.1° 0.4°
2334+61	114.3°+0.2°	4.61	*		114.3°+03°	80	0° 0.1°
				S166	114.6° –0.8°	10	0.3° 1°
				S165	114.6°+02°	10	0.3° 0°
				S163	113.5°–0.7°	10	0.8° 0.9°
0531+21	184.6°–5.8°	3.1	Crab Nebula		184.6°–5.8°	5	0° 0°
0631+10	201.2°+0.4°	4.64		IC 2169	201.7°+0.1°	23	0.5° 0.3°
				IC 446	201.3°+0.2°	5	0.1° 0.2°
				*	201.6°+0.6	2	0.4° 0.2°
				*	201.8°+0.6°	2	0.6° 0.2°
0833–45	263.6°–2.8°	4.05	Vela XYZ		263.9°–3.3°	260	0.3° 0.5°
				Gama Nebula	260° 0°	2200	3.6° 2.8°
1046–58	287.4°+0.6°	4.31		RCW 52	287.1°+0.4°	15	0.3° 0.2°
				H36	288°+0°	15	0.6° 0.6°

Table. (Contd.)

PSR	1, b	log T	SNR	H II	1, b	2Θ	Δl, Δb
1	2	3	4		5	6	7
1338–62	308.7°+0.0°	4.08	*		308.7°+0°	12	0° 0°
				*	308.7°+0.6	4	0° 0.6°
				*	308.6°+0.6°	5	0.1° 0.6°
1509–58	320.3°–1.2°	3.19	RCW 89		320.4°–1.2°	30	0.1° 0°
				*	320.4°–1.5°	40	0.1° 0.3°
				*	320.3°–0.3°	3	0° 0.9°
				*	320.3°–0.2°	2	0° 1°
				*	320.4°–1°	6	0.1° 0.2°
				*	321.0°–0.5°	3	0.7° 0.7°
				*	321.1°–0.5°	4	0.8° 0.7°
1610–50	332.2°+0.2°	3.87	*		322.2°+0.2°	12	0° 0°
			RCW 103		332.4°–0.4°	10	0.2° 0.6°
			Kes 32		332.4°+0.1°	13	0.2° 0.1°
				*	331.3°–0.2°	1	0.9° 0.4°
				*	331.3°–0.3	2	0.9° 0.5°
				*	331.4°+0	2	0.8° 0.2°
				*	331.5°–0.1	2	0.7° 0.3°
				*	332.5°–0.5°	1	0.3° 0.7°
				*	332.4°–0.4°	6	0.2° 0.6°
				*	332.5°–0.1	1	0.3° 0.3°
				*	332.7°–0.6°	4	0.5° 0.8°
				*	332.8°–0.6°	5	0.6° 0.8°
				*	333.0°–0.4°	5	0.8° 0.6°
				*	333.1°–0.4°	4	0.9° 0.8°
1643–43	341.1°+1.0°	4.51	*		340.4°+0.4	6	0.7° 0.6°
			*		340.6°+0.3°	5	0.5° 0.7°
1706–44	343.1°–2.7°	4.24					
1723–33	354.1°+0.1°	4.41		*	353.1°+0.6°	6	1° 0.8°
				*	353.2°+0.9°	3	0.9° 0.8°
1737–30	358.3°+0.2°	4.32	MSH 17–39		357.7°–0.1°	10	0.6° 0.3°

The time evolution of the number density of pulsars suggests that pulsars are born in clusters, with the period for the birth of the pulsars in a cluster being no more than several million years. A cluster of pulsars is preserved for a period of the order of tens of millions of years, and then dissipates due to the high velocities of the pulsars. Note that the lifetime of pulsar clusters exceeds the lifetime of the associated gas complex by an order of magnitude. This suggests that the lifetime of the gas complex reflects the active stage of the entire complex, with its enhanced number of supernova explosions.

ACKNOWLEDGMENTS

The authors thank M. Prokhorov for useful comments. This work was supported by the Russian Foundation for Basic Research (project code 00-02-17850), the Astronomy State Science and Technology Program, and INTAS (grant 96-0154).

REFERENCES

1. A. V. Pynzar', Astron. Zh. **70**, 480 (1993) [Astron. Rep. **37**, 245 (1993)].
2. A. V. Pynzar' and V. I. Shishov, Astron. Zh. **76**, 504 (1999) [Astron. Rep. **43**, 436 (1999)].
3. J. H. Taylor, R. N. Manchester, and A. G. Lyne, Astrophys. J., Suppl. Ser. **88**, 529 (1993).
4. J. H. Taylor, R. N. Manchester, A. G. Lyne, and F. Camilo, unpublished work (1995).
5. W. J. Altenhoff, D. Downes, T. Pauls, and J. Shraml, Astron. Astrophys., Suppl. Ser. **35**, 23 (1979).
6. R. F. Haynes, J. L. Caswell, and L. W. J. Simons, Aust. J. Phys. Astrophys. Suppl. **45**, 1 (1978).
7. T. Handa, Y. Sofue, N. Nakai, *et al.*, Publ. Astron. Soc. Jpn. **39**, 709 (1987).
8. W. J. Altenhoff, D. Downes, L. Goad, *et al.*, Astron. Astrophys., Suppl. Ser. **1**, 319 (1970).
9. R. J. Reynolds, F. L. Roesler, and F. Sherb, Astrophys. J. Lett. **192**, L53 (1974).
10. R. J. Reynolds, Astrophys. J. **282**, 191 (1984).
11. R. J. Reynolds and P. M. Ogden, Astron. J. **87**, 306 (1982).
12. R. J. Reynolds, Astrophys. J. **216**, 433 (1977).
13. A. Broadbent, C. G. T. Haslam, and J. L. Osborne, Mon. Not. R. Astron. Soc. **237**, 381 (1989).
14. L. Hart and A. Pedlar, Mon. Not. R. Astron. Soc. **176**, 547 (1976).
15. F. J. Lockman, Astrophys. J. **209**, 429 (1976).
16. J. C. Cersosimo, I. N. Azcarate, L. Hart, and F. R. Colomb, Astron. Astrophys. **208**, 239 (1989).
17. A. V. Pynzar', Pis'ma Astron. Zh. **17**, 249 (1991) [Sov. Astron. Lett. **17**, 105 (1991)].
18. N. G. Bochkarev, in *Space Physics. Small Encyclopedia* [in Russian] (Sovetskaya Entsiklopediya, Moscow, 1986), p. 270.
19. D. A. Green, Mon. Not. R. Astron. Soc. **209**, 449 (1984).
20. A. V. Kovalenko, A. V. Pynzar', and V. A. Udal'tsov, Astron. Zh. **71**, 110 (1994) [Astron. Rep. **38**, 95 (1994)].
21. V. S. Avedisova and G. I. Kondratenko, Nauchn. Inf. Astron. Sov. Akad. Nauk SSSR **56**, 59 (1984).
22. E. C. Reinfenstein, T. L. Wilson, B. F. Burke, *et al.*, Astron. Astrophys. **4**, 357 (1970).
23. T. L. Wilson, P. G. Mezger, F. F. Gardner, and D. K. Milne, Astron. Astrophys. **6**, 364 (1970).
24. D. Downes, T. L. Wilson, J. Bieging, and J. Wink, Astron. Astrophys., Suppl. Ser. **40**, 379 (1980).
25. B. T. Lynds, Astrophys. J., Suppl. Ser. **12**, 163 (1965).
26. T. A. Lozinskaya, *Supernovae and Stellar Winds. Interaction with Galactic Gas* [in Russian] (Nauka, Moscow, 1986).
27. L. Spitzer, Jr., *Physical Processes in the Interstellar Medium* (Wiley, New York, 1978; Mir, Moscow, 1981).
28. A. M. Cherepashchuk, Astrophys. Space Sci. **221**, 227 (1994).

Translated by D. Gabuzda

Astronomy Reports, Vol. 45, No. 7, 2001, pp. 510–516. Translated from Astronomicheskiĭ Zhurnal, Vol. 78, No. 7, 2001, pp. 594–601.

The Dust Envelope of R Cas

G. Weigelt[1] and B. F. Yudin[2]

[1]*Max-Planck-Institut für Radioastronomie, Auf dem Hügel 69, D-53121 Bonn, Germany*
[2]*Sternberg Astronomical Institute, Universitetskiĭ prospekt 13, Moscow, 119899 Russia*

Received November 10, 2000

Abstract—The spectral energy distribution in the far infrared and the shape of a broad emission band in the spectrum of R Cas at 9–13 μm can be reproduced in a model with a dust envelope consisting of approximately half amorphous olivine ($Mg_{0.8}Fe_{1.2}SiO_4$) and half amorphous aluminum-oxide grains (Al_2O_3), with a small admixture of spinel grains ($MgAl_2O_4$). The dust envelope's optical depth $\tau(50\ \mu m)$ is $\approx 5 \times 10^{-3}$ [$\tau(1.25\ \mu m) \approx 0.07$ for $a_{gr} \approx 0.05$ μm], and its mass within $r \leq 0.025$ pc M_{dust} is $\approx 8 \times 10^{-6} M_\odot$. The index α in the power-law radial dust distribution, $n_d \propto (R_*/r)^\alpha$, is ≈ 1.8. Over the last several thousand years, the mass-loss rate of R Cas has been decreasing as $\dot{M}(t) \propto t^{0.2}$ (where time is measured backward from the present). This probably implies that R Cas experienced a thermal helium flare several thousand years ago. If $M_{gas}/M_{dust} \approx 200$ (where M_{gas} is the gas mass), the mean mass-loss rate of the star is $\dot{M} \approx 6 \times 10^{-7} M_\odot$/yr. © *2001 MAIK "Nauka/Interperiodica".*

INTRODUCTION

R Cas belongs to the class of Mira Ceti long-period variable giants (Miras). The period of its brightness variations is $P \approx 430\overset{d}{.}5$, with a visual brightness amplitude $\Delta V \approx 9$. The spectral class of the red giant varies in the range M6e–M10e [1]. The visual light curve of R Cas is described in detail by Isles and Saw [2]. Infrared light curves in the *JHKLM* bands are presented by Nadzhip *et al.* [3]. In particular, they showed that the amplitude of the brightness variations decreases with increasing wavelength, from $\sim 1\overset{m}{.}1$ in the *J* band to $\sim 0\overset{m}{.}5$ in the *L* band. At longer wavelengths, up to the far infrared, the amplitude remains constant.

Ground-based IR observations of R Cas with filters centered on 10, 20, and 25 μm have shown an IR excess in the energy distribution, due to the emission of a circumstellar dust envelope [4, 5]. IRAS photometry at 12, 25, 60, and 100 μm and spectrophotometric observations in the 8–23-μm band confirmed the results of the ground-based observations, revealing a broad emission band at 9–13 μm in the spectrum of R Cas [6, 7].

Spectrophotometry of R Cas at 29–197 μm using the Infrared Space Observatory (ISO) in 1996–1997 detected numerous H_2O emission lines and yielded the energy distribution in the far infrared continuum [8]. In 1997, Miyata *et al.* [9] obtained a UKIRT spectrum of R Cas at 8–13 μm.

The present work is devoted to a detailed study of the structure of the circumstellar dust envelope of R Cas. It is based on an analysis of the spectral energy distribution, currently available from 1–200 μm. By solving for the radiative transfer in a spherical dust envelope containing grains of various chemical compositions, we can construct a model for the envelope that reproduces fairly well both the energy distribution in the far infrared spectrum and the shape of the emission band.

This is the first time that the structure of the dust envelope of R Cas has been derived. In particular, Miyata *et al.* [9], whose spectrum of R Cas we have adopted, carried out a detailed study of the shapes of the emission bands in the spectra of 18 Miras, searches for correlations of the band shape and intensity with other parameters of the stellar emission, and an analysis of the chemical composition of the dust grains radiating in the emission band. In addition, we elucidate here which parameters of the optically thin dust envelopes of Miras can and which cannot be determined with reasonable certainty.

2. OBSERVATIONAL DATA

Figure 1 shows the energy distribution of R Cas at the maximum of its IR brightness. The dates of the maxima are given by $\mathrm{Max}(J) = 2447151.0 + 429\overset{d}{.}6E$ [3]. The zero phase ($\phi = 0$) corresponds to the maximum IR brightness.

The energy distribution in Fig. 1 is based on the observations of R Cas presented in [3, 8, 9]. ISO spectral observations were carried out on June 6, 1997 ($\phi \approx 0.04$) at 29–197 μm (circles in Fig. 1) [8]. Continuum fluxes of the star were obtained in nine spectral bands free of the numerous H_2O emission lines. To these we have added *JHKLM* flux estimates (squares in Fig. 1) derived from our own observations of R Cas on August 9,

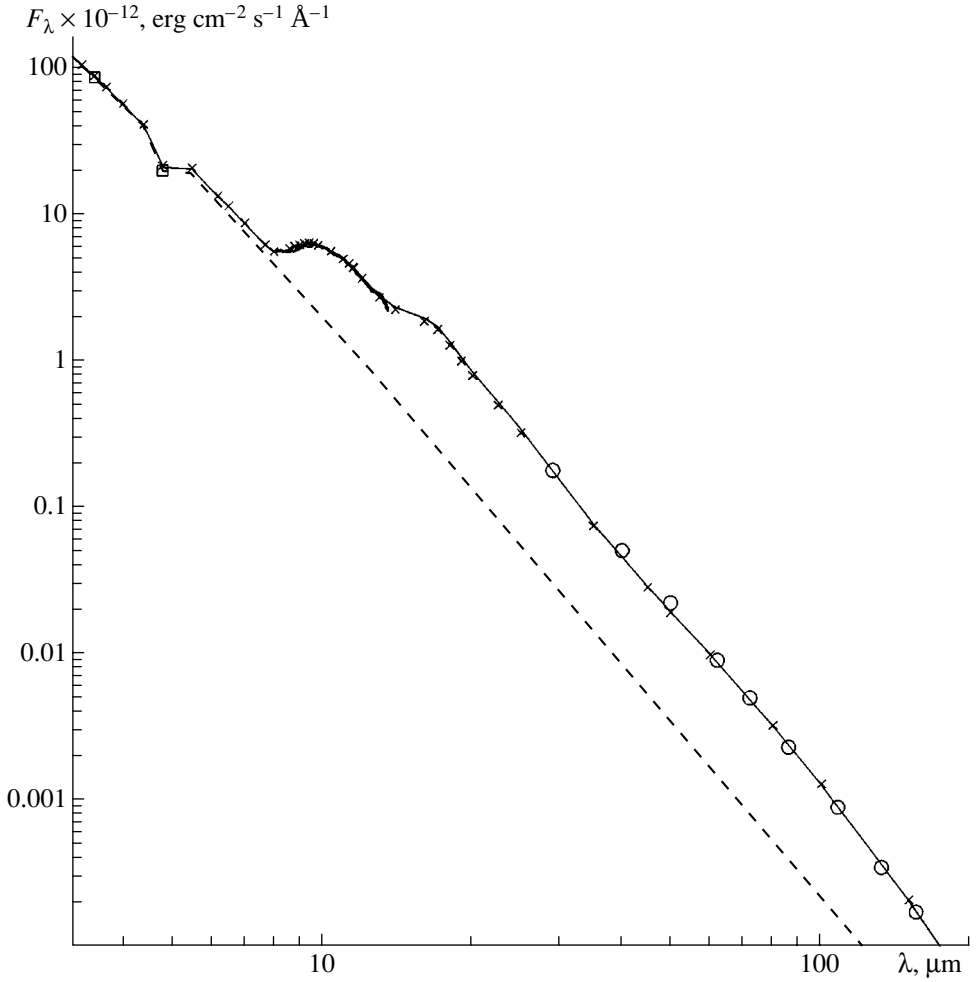

Fig. 1. Spectral energy distribution of R Cas (squares, circles, and heavy solid curve) and in models M1 (light solid curve) and M2 (crosses). The dashed curve shows an extrapolation of the stellar continuum to the infrared. For details see text.

1998 ($\phi \approx 0.04$) [3]. Analysis of the *JHKLM* light curves [3] shows that the near-infrared magnitudes of R Cas during the brightness maxima of 1997 and 1998 differed by no more than $0\overset{m}{.}1$. Such a small difference has no effect on the dust-envelope parameters derived from our combined energy distribution (Fig. 1). Therefore, we made no additional corrections to the *JHKLM* fluxes.

Spectral observations of R Cas in the 8–13.5-μm band were carried out using UKIRT on September 18, 1997 ($\phi \approx 0.28$) [9]; 12 days earlier (September 6, 1997), we estimated its *JHKLM* magnitudes [3]. By comparing the *L* and *M* magnitudes of R Cas in September 1997 and at the IR brightness maximum in August 1998, we reduced the spectrum of R Cas to the maximum. We based this reduction on the results of [3], where we showed that the amplitude of the brightness variations of R Cas remains virtually constant with wavelength when $\lambda > 3$ μm, and is $\sim 0\overset{m}{.}5$. This amplitude implies that the accuracy of the spectrum reduction was no worse than 15%. Thus, we have for the epoch of brightness maximum a combined energy distribution in the range 1–200 μm, which is quite suitable for estimating the main global parameters of the dust envelope of R Cas.

On August 24, 1996, Weigelt *et al.* [10] estimated the angular diameter of R Cas at 2.2 μm to be $\theta_{2.2} \approx 0.0253''$. At that time, R Cas was near its IR brightness maximum ($\phi \approx 0.93$). Weigelt *et al.* [10] derived the radius of the stellar photosphere by comparing the visibility curve obtained from interferometric observations with the corresponding theoretical curve, and estimated the bolometric flux from photometric observations. The distance to R Cas corresponding to its parallax is $D \approx 107$ pc. In this case, we obtain the following estimates for the parameters of the star near its IR brightness maximum (which we have used in our model calculations): radius of the photosphere $R_* \approx 277R_\odot$, bolometric luminosity $L_{bol} \approx 3280L_\odot$, and effective temperature $T_{eff} \approx 2630$ K.

3. FORMULATION OF THE PROBLEM AND CALCULATIONS

We calculated the outgoing radiation flux of the star surrounded by the dust envelope using the CSDUST3 software, described in detail by Egan *et al.* [11]. One of the input parameters is the spectral energy distribution of the star, $L_*(\lambda)/L_{bol}$. For brevity, we will call the combination of the star + dust envelope the "object."

Other input parameters are the inner radius of the dust envelope R_{in}, which can be replaced (as an input parameter) with the temperature of the dust grains at this radius, $T_{gr,\,in}$; the outer radius of the dust envelope R_{out}; the dust density distribution in the envelope, $n_d(r)$; the size of the dust grains, a_{gr}; their chemical composition and the relative number densities of dust grains with various chemical compositions; and the optical depth of the dust envelope at some wavelength,

$$\tau(\lambda) = (Q_{abs}(\lambda) + Q_{sca}(\lambda))\pi a_{gr}^2 \int_{R_{in}}^{R_{out}} n_d(r)dr, \qquad (1)$$

where $Q_{abs}(\lambda)$ and $Q_{sca}(\lambda)$ are absorption and scattering efficiencies, respectively.

Judging from the color indices, there is no IR excess in the *JHKLM* bands. In particular, the *J–K* color index at the IR brightness maximum corresponds to a color temperature of ~2650 K. The *L–M* color index is always small and negative, typical of red giants without dust envelopes, and formally does not correspond to any color temperature. Its negative value, associated with the fact that the *M* filter includes a CO absorption band, clearly demonstrates an absence of any appreciable IR excess. Thus, the spectral energy distribution at 1–5 μm is, to a fairly good approximation, determined directly by the observed *JHKLM* fluxes. This is confirmed by calculations that show the optical depth of the dust envelope of R Cas at 1.25 μm (*J* band) to be $\tau(J) \leq 0.1$.

To calculate the radiation of the star surrounded by its dust envelope, the energy-distribution curve must be extended into the optical. We did this using the mean visual magnitude of R Cas at its brightness maximum. The visual range contains less than 15% of the bolometric flux of R Cas. Therefore, possible differences between the adopted and true visual magnitudes of R Cas during the brightness maximum in June 1997 will not significantly affect the estimated parameters of the dust envelope.

Furthermore, since the optical color indices of R Cas itself are not precisely known, we cannot estimate how much the optically thin dust envelope distorts the star's energy distribution in this spectral range. In other words, even if we had *UBV* observations of R Cas for the date we need, we would have to set the spectral energy distribution in the optical (like at 1–5 μm) using the observed fluxes in these bands. The radiation of the dust envelope (IR excess) begins to be appreciable against the stellar background only at $\lambda \geq 9$ μm (Fig. 1).

We have extrapolated the spectral energy distribution to wavelengths $\lambda > 5$ μm using the formula of Engelke [12], which has the form of a modified Planck function with the effective temperature as a parameter. Engelke [12] showed that this formula reproduces well the continua in cool stars (in particular, red giants) at $\lambda > 3$ μm. We calculated this function using $T_{eff} = 2630$ K and normalized the resulting curve to the spectral radiation flux of R Cas at 3.5 μm (dashed curve in Fig. 1). Recall that the stellar flux in the *M* band corresponds to the observed magnitude, not the magnitude calculated from the formula of [12]. This results in a depression in the energy-distribution curve.

The inner radius of the optically thin dust envelope, which is equivalent to the temperature of the dust grains at the envelope inner boundary as an input parameter, is found by fitting the model to the observed energy distribution in the near infrared. Grains in the inner regions of the dust envelopes of red giants radiate precisely in this wavelength range. Since the dust envelope of R Cas is optically thin and is not observationally manifest in the near infrared, we cannot directly estimate R_{in} or $T_{gr,\,in}$ with certainty. Typical dust temperatures at the inner boundaries of red-giant envelopes are ~1000 K. To elucidate how sensitive the estimated global parameters of the dust envelope are to the choice of $T_{gr,\,in}$, we performed calculations with $T_{gr,\,in} \approx 1000$ and 1250 K.

The aperture of the ISO LWS spectrophotometer is 1.65′. R Cas is nearby, and its envelope is not completely included in the spectrophotometer aperture. In this case, the outer radius of the model dust envelope, $R_{out} \approx 0.025$ pc, is determined by the aperture size. For an envelope expansion velocity $V_{env} \approx 10$ km/s [13], we have $R_{out}/V_{env} \approx 2500$ years. Thus, our analysis deals with the innermost, recently formed parts of the dust envelope of R Cas.

In this situation, it was necessary to carry out the calculations in two steps. First, for each wavelength of a grid containing 80 points from 0.25–500 μm, we calculated the angular distribution of the object brightness within $r \leq R_{out}$ for $R_{out} = 0.3$ pc. This distribution was then convolved with a rectangular 1.65′ circular aperture corresponding to $R_{out} \approx 0.025$ pc.

Note that the effect of the aperture is appreciable only at $\lambda > 100$ μm. The cool outer layers of the dust envelope radiate precisely at these wavelengths. The inner radius θ_{in} of the dust envelope in angular units is <0.15″. Therefore, the hottest inner layers of the dust envelope radiating in the near infrared fall entirely within the aperture of the *JHKLM* photometer (12″). This means that the signal will not increase if the aperture size is enlarged to that of the ISO spectrophotometer.

The broad emission band in the spectrum of R Cas is a blend of three bands peaking at ~10, ~11.5, and ~13 μm

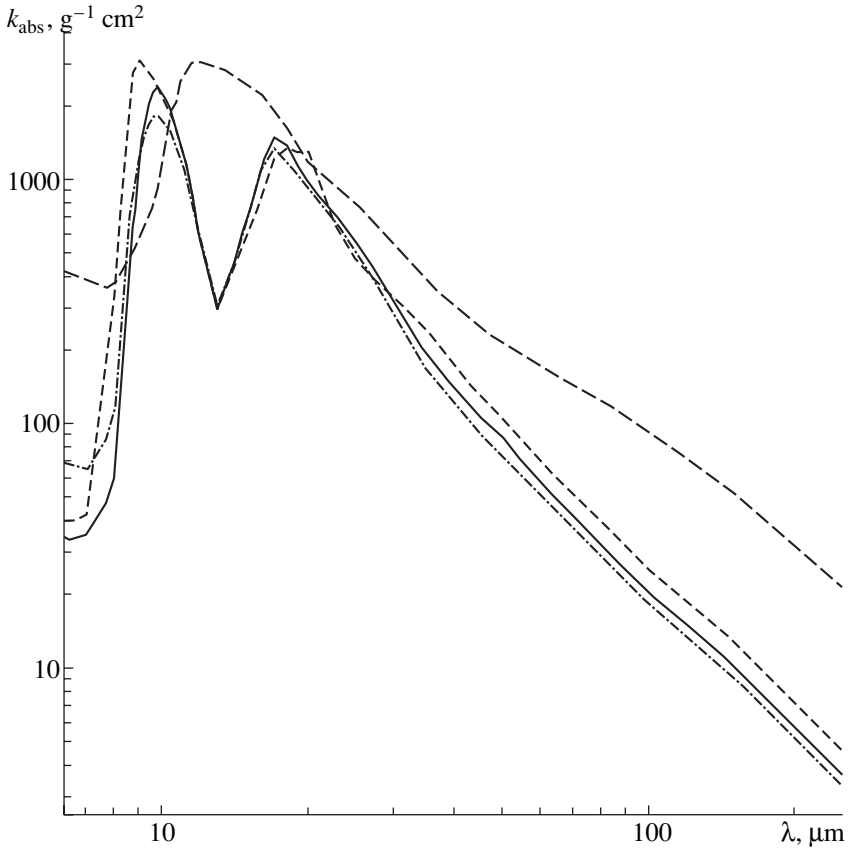

Fig. 2. Specific absorption coefficients for spherical grains (a_{gr} = 0.05 μm) of amorphous silicates composed of pyroxene $Mg_{0.4}Fe_{0.6}SiO_3$ (short-dashed curve), olivine $Mg_{0.8}Fe_{1.2}SiO_4$ (dot–dashed curve), and $MgSiO_4$ (solid curve), as well as of amorphous aluminum oxide (long-dashed curve).

[8]. The first is due to grains of amorphous silicates and the second to grains of amorphous aluminum oxide (Al_2O_3). The composition of the dust grains creating the third band has not yet been definitely established. One of the most probable candidates is $MgAl_2O_4$ [14]. Figure 2 shows the specific absorption coefficient $k_{abs}(\lambda) = 3Q_{abs}(\lambda)/4a_{gr}\rho_{gr}$ as a function of wavelength for four kinds of spherical dust grains with a_{gr} = 0.05 μm. Among these are amorphous silicates with pyroxene ($Mg_xFe_{1-x}SiO_3$, x = 0.4) and olivine ($Mg_{2y}Fe_{2-2y}SiO_4$, y = 0.4, 0.5), as well as grains of amorphous aluminum oxide.

We calculated the efficiencies of absorption $Q_{abs}(\lambda, a_{gr})$ and scattering $Q_{sca}(\lambda, a_{gr})$ of spherical dust grains with radius a_{gr} using Mie theory, and the refractive indices of the corresponding substances were taken from [15, 16]. We can see from Fig. 2 that the peak in $k_{abs}(\lambda)$ occurs at ~9.4 μm for pyroxenes and at ~9.8 μm for olivines. This difference is sufficient for us to conclude that the dust grains in red-giant envelopes consist of olivine [15]. Our calculations show that R Cas is no exception in this respect. Note also that an enhanced iron content in the silicates is mainly manifest as an increased absorption coefficient at 1–9 μm (Fig. 2). This modifies the blue wing of the silicate emission band: as the iron content increases, the wing becomes flatter, i.e., the ratio F(9.8 μm)/F(9 μm) decreases.

Figure 3 presents the specific absorption and scattering coefficients computed for grains of $Mg_{0.8}Fe_{1.2}SiO_4$ with a_{gr} = 0.01 and 0.1 μm; i.e., for fairly small and large silicate grains. We can see that the optical depth of the dust envelope in the middle and far infrared is completely determined by the absorption coefficient, and scattering does not play a significant role in the object's emission. Furthermore, small and large grains have nearly identical absorption coefficients in this spectral range. The reason is that, at λ > 5 μm, even large (for red-giant dust envelopes) dust grains are "Rayleigh" particles; i.e., $a_{gr} < 0.05\lambda$. At the same time, the absorption coefficient of a "Rayleigh" particle does not depend on its radius, and is determined solely by the index of refraction of the substance of which it is made.

Thus, if we replace small grains with large ones in the model dust envelope, its optical depth in the middle and far infrared will not change. Therefore, changes of the radiation flux of the optically thin dust envelope $F(\lambda) \propto B(\lambda, T_{gr}(a_{gr}))\tau(\lambda)$ are due only to changes of the

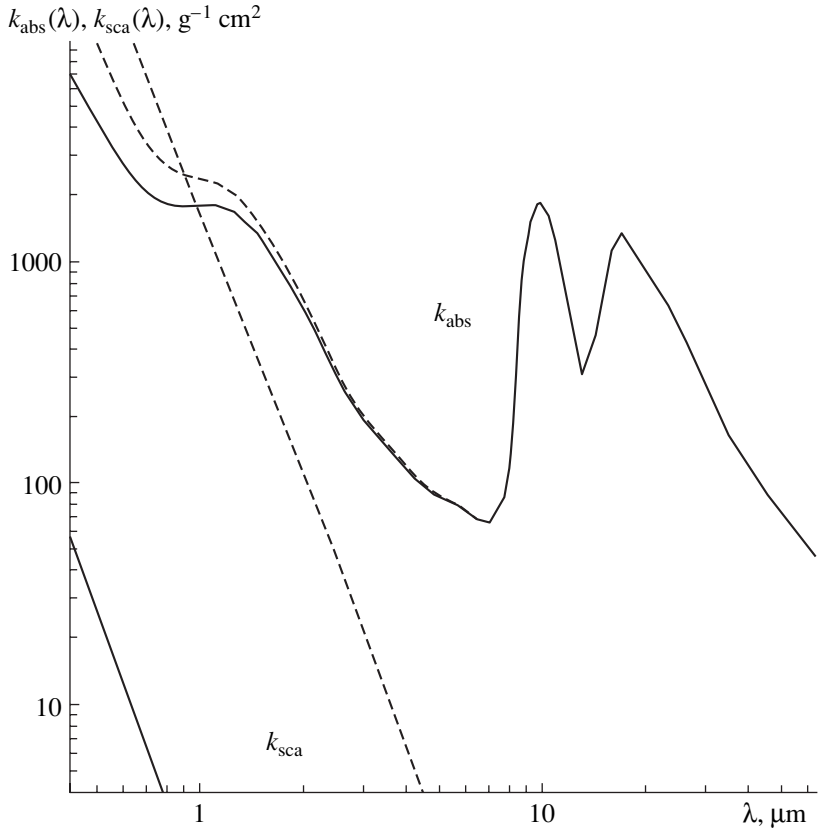

Fig. 3. Specific absorption and scattering coefficients for spherical grains of amorphous olivine ($Mg_{0.8}Fe_{1.2}SiO_4$) with a_{gr} = 0.01 μm (solid curves) a_{gr} = 0.1 μm (dashed curves).

grain temperature. However, our calculations show that these changes do not exceed 3% if a dust grain of $Mg_{0.8}Fe_{1.2}SiO_4$ is embedded in the radiation field of an R Cas-type star and the grain radius varies from 0.01 to 0.1 μm. In some layers of the dust envelope, these changes will be somewhat greater due to multiple scattering by large grains, which are good "reflectors." Nevertheless, these changes do not exceed 7% if $\tau(J) \le 0.1$.

As a result, the radiation flux will not change significantly as the dust temperature varies. The maximum change (~10%) will be observed at the silicate-band peak. Thus, to bring the calculated flux into agreement with the observed flux, we must change the optical depth by 10%. It is clear that such a change is small from the point of view of the estimated envelope parameters (for example, its mass). Therefore, when modeling the dust envelope of R Cas, it does not make sense to compose it of grains of different sizes, because this will not significantly change the parameter estimates. Moreover, there are no criteria for doing this. From the point of view of the dust grains' size, the optical is the most informative spectral range. However, as already noted, we cannot confidently represent the spectral energy distribution of R Cas itself in the optical, and, accordingly, we cannot tell how and to what extent it is distorted by the dust envelope. In our calculations, we adopted a_{gr} = 0.05 μm.

To conclude our discussion of the input model parameters, we emphasize that the parameters of the dust envelope, such as its optical depth and the index α in the dust-density distribution $n_d \propto (R_*/r)^\alpha$, are determined by fitting the calculated energy distribution in the far infrared to the observed distribution. These parameters determine the envelope mass and the mass-loss rate of the star. In turn, the chemical composition of the dust envelope is determined by the spectral shape of the 10-μm emission band. Thus, only analysis of the combined energy distribution from 1–200 μm can provide reasonably comprehensive information about the structure of the envelope of R Cas, which is precisely what motivated us to perform these calculations.

4. RESULTS

Figure 1 shows the spectral energy distributions of R Cas and of two dust-envelope models. We calculated theoretical energy distributions assuming temperatures of ~1000 K (model M1) and 1250 K (model M2) for the silicate grains of $Mg_{0.8}Fe_{1.2}SiO_4$ at the inner envelope boundary. In both models, we added to the silicate grains 43% (54%) and 57% (46%) by number (mass) of

grains of amorphous aluminum oxide. Both dust envelopes have identical outer radii of $R_{out} = 0.025$ pc.

In models M1 and M2, respectively, $R_{in}/R_* \approx 4.7$ and 3.0, $\tau(J) \approx 0.066$ and 0.077, $\alpha \approx 1.80$ and 1.75, and the dust mass within $[R_{in}, R_{out}]$ is $M_{dust} \approx 8.2 \times 10^{-6} M_\odot$ and $6.9 \times 10^{-6} M_\odot$. It is more appropriate to specify the model optical depth in the far infrared, in which case this parameter will not depend on the size of the dust grains filling the model envelope. For example, $\tau(50\ \mu m) \approx 5 \times 10^{-3}$ in models M1 and M2. The value $\alpha < 2$ implies that the mass-loss rate of R Cas has been decreasing with time as $\dot{M}(t) \propto t^{0.2}$ (in model M1) and $\dot{M}(t) \propto t^{0.25}$ (model M2), where time is counted backwards from the present. During the last ~2500 years (this time is equal to the R_{out}/V_{env} ratio), the mass-loss rate has decreased by factors of ~3.8 and ~5.9 in models M1 and M2, respectively.

The change in the mass-loss rate depends strongly on the inner radius of the dust envelope. This explains the wide scatter of the estimated variations of $\dot{M}(t)$ in models M1 and M2. In turn, as noted above, the inner radii of optically thin dust envelopes cannot be estimated with certainty. Based on analyses of the spectral energy distributions of red giants with optically thick dust envelopes, we give preference to model M1, with a temperature of ~1000 K for the silicate grains at the inner boundary of the dust envelope of R Cas.

Phases in the evolution of a Mira when its mass-loss rate decreases occur after each helium flare, and are associated with the temporary decrease of the luminosity. For a Mira such as R Cas with a main-sequence mass of $3M_\odot$, the interval between flares is ~10^5 years, with 10% of this period falling in the phase with reduced bolometric luminosity and mass-loss rate. The mass-loss rate decreases by more than an order of magnitude [19], while the effective temperature does not change significantly. It was shown in [19] that, in Miras with periods exceeding 100 days, $\dot{M} \propto L_{bol}^{4.2}/T_{eff}^2$. In this case, the luminosity of the Mira R Cas has decreased by a factor of ~1.5 during the last 2500 years.

It is usually believed that the gas-to-dust ratios M_{gas}/M_{dust} for oxygen-rich Miras are ≈200 [17, 18]. In this case, the mean mass-loss rate $\dot{M}$ of R Cas over the last 2500 years has been $6.6 \times 10^{-7} M_\odot$/yr and $5.5 \times 10^{-7} M_\odot$/yr in models M1 and M2, respectively. However, in our model, almost half the dust envelope by mass consists of aluminum oxide. The solar abundance of aluminum is an order of magnitude lower than those of silicon, magnesium, or iron. If the chemical composition of the atmosphere of R Cas with respect to these elements is solar, this implies that a considerable amount of silicon, magnesium, and iron in the stellar envelope remains in the gas phase. Accordingly, the ratio M_{gas}/M_{dust} we adopted earlier must be increased by an order of magnitude.

An emission "hump" is visible in the spectrum of R Cas at 13 μm (Fig. 1), which is not reproduced by the mixture of silicate and aluminum-oxide dust grains. As noted above, this spectral band is currently identified with grains of $MgAl_2O_4$ (spinel). Their absorption coefficient has a very sharp peak at 12.95 μm [14]. At this wavelength, it exceeds the absorption coefficient of the mixture of dust grains of olivine and aluminum oxide by an order of magnitude. Therefore, as our estimates show, it is sufficient to add to the mixture of dust grains less than 1% of spinel grains by number in order for the observed emission "hump" to appear in the model spectrum at 13 μm. These will not appreciably contribute to the dust-envelope emission at any other wavelength.

The predicted luminosity of the Mira R Cas according to the period–luminosity relation exceeds its mean luminosity estimated from its mean bolometric flux and parallax distance by a factor of more than three. Therefore, it is possible that the estimated distance of R Cas will be refined with time. In this connection, we should note that, in calculations of the radiation of a star surrounded by a dust envelope, one input parameter related to the luminosity is the flux at the inner boundary of the dust envelope $L_{bol}/4\pi R_{in}^2 = F_{bol}(D/R_{in})^2$, where D is the distance to the star. Thus, if the estimated distance to the star changes, the envelope's linear dimensions and related parameters can be recalculated subject to the condition D/R_{in} = const. In particular, the estimated optical depth will not change, and the estimated mass-loss rate will change as $\dot{M} \propto D$.

To conclude, we note that the optical depth and chemical composition of the dust envelopes of Miras are important parameters of models for their condensation. Together with the dust density distribution in the envelope, they enable us to estimate the mass-loss rate, which is a key parameter determining the duration of the Mira's stay on the upper asymptotic giant branch. At this stage, cyclic variations associated with thermal helium flares are superimposed on the star's monotonic evolution, and analysis of the dust envelope's spatial structure tells us at what phase of this cyclic process the Mira is currently located. In turn, these parameters of the dust envelopes can be estimated from model calculations using only the energy distribution from the near to far infrared and the spectrum of the star near 10 μm.

REFERENCES

1. P. N. Kholopov, N. I. Samus', V. P. Goranskiĭ, *et al.*, *General Catalogue of Variable Stars* (Nauka, Moscow, 1985), Vol. 1, p. 236.
2. J. E. Isles and D. R. B. Saw, J. Br. Astron. Soc. **99**, 121 (1989).
3. A. É. Nadzhip, A. M. Tatarnikov, V. I. Shenavrin, *et al.*, Pis'ma Astron. Zh. **27** (2001) (in press) [Astron. Lett. **27** (2001) (in press)].
4. D. Morrison and T. Simon, Astrophys. J. **186**, 193 (1973).
5. W. Hagen, Publ. Astron. Soc. Pac. **94**, 835 (1982).

6. M. Rowan-Robinson, T. D. Lock, D. W. Walker, and S. Harris, Mon. Not. R. Astron. Soc. **222**, 273 (1986).
7. T. Onaka, T. de Jong, and F. J. Willems, Astron. Astrophys. **218**, 169 (1989).
8. Truong-Bach, R. J. Sylvester, M. J. Barlow, *et al.*, Astron. Astrophys. **345**, 925 (1999).
9. T. Miyata, H. Kataza, Y. Okamoto, *et al.*, Astrophys. J. **531**, 917 (2000).
10. G. Weigelt, K.-H. Hofmann, and M. Scholz, private communication (2000).
11. M. P. Egan, C. M. Leung, and G. F. Spagna, Comput. Phys. Commun. **48**, 271 (1988).
12. C. W. Engelke, Astron. J. **104**, 1248 (1992).
13. K. H. Hinkle, W. W. G. Scharlach, and D. N. B. Hall, Astrophys. J., Suppl. Ser. **56**, 1 (1984).
14. T. Posch, F. Kerschbaum, H. Mutschke, *et al.*, Astron. Astrophys. **352**, 609 (1999).
15. J. Dorschner, B. Begemann, Th. Henning, *et al.*, Astron. Astrophys. **300**, 503 (1995).
16. B. Begemann, J. Dorschner, Th. Henning, *et al.*, Astrophys. J. **476**, 199 (1997).
17. G. R. Knapp, Astrophys. J. **293**, 273 (1985).
18. J. Alcolea and V. Bajarrabal, Astron. Astrophys. **245**, 499 (1991).
19. T. Blocker, Astron. Astrophys. **297**, 727 (1995).

Translated by G. Rudnitskiĭ

Astronomy Reports, Vol. 45, No. 7, 2001, pp. 517–526. Translated from Astronomicheskiĭ Zhurnal, Vol. 78, No. 7, 2001, pp. 602–612.

Wolf–Rayet Stars and Cosmic Gamma-ray Bursts

K. A. Postnov and A. M. Cherepashchuk

Sternberg Astronomical Institute, Universitetskiĭ pr. 13, Moscow, 119899 Russia

Received November 14, 2000

Abstract—The observational properties of cosmic gamma-ray bursts and of Wolf–Rayet (WR) stars and their CO cores at the end of their evolution are analyzed. WR stars do not have hydrogen envelopes, facilitating the transformation of the energy of collapse into observable gamma rays. Of the ~90 well-localized gamma-ray bursts, 21 have optical identifications, of which 16 have measured redshifts (z = 0.4–4.5). The distribution of gamma-ray bursts in energy $N(\Delta E)$ has a large scatter, from 3×10^{51} to 2×10^{54} erg. There is some evidence that the distribution $N(\Delta E)$ is bimodal if we include the gamma-ray burst GRB 980425, which is associated with the peculiar type Ic supernova SN 1998bw in the nearby elliptical galaxy ESO 184–G82, for which $\Delta E_\gamma \approx 10^{48}$ erg. These characteristics of gamma-ray bursts are reminiscent of the distribution of final masses for the CO cores of WR stars, which uniformly covers a broad range: $M_{CO} = (1–2)M_\odot$–$(20–44)M_\odot$. The possible bimodality of the gamma-ray burst energy distribution ($E_1 = 10^{48}$ erg; $\Delta E_2 = 3 \times 10^{51}$–$2 \times 10^{54}$ erg) could be associated with the bimodal mass distribution for stellar relativistic objects ($M_{NS} = (1.35 \pm 0.15)M_\odot$; $M_{BH} = (4–15)M_\odot$). The fact that SN 1998bw is a "peculiar" type Ic supernova, not typical for the collapses of WR stars (which usually give rise to type Ib/c supernovae), could be related to the rotation of the collapsing CO core. This "drags out" the time for the collapse, leading to the formation of a neutron star, a decrease in the gamma-ray burst energy, and an increase in the fraction of kinetic energy transferred to the supernova envelope. The expected rate of collapse of the CO cores of WR stars in the Galaxy is $\sim 10^{-3}$ /yr. This is at least three orders of magnitude higher than the mean frequency of gamma-ray bursts per galaxy ($\sim 10^{-6}$–10^{-7}/yr). Two models for gamma-ray bursts with WR stars as progenitors are considered: the hypernova model of Paczynski (1998) and the pulsation instability CO-core collapse model proposed by Gershteĭn (2000). In both models, the rate of CO-core collapses can be brought into agreement with the observed rate of gamma-ray bursts by taking into account the anisotropy of the gamma radiation, associated with either a relativistic jet or the random character of the initial CO-core collapse due to instabilities. It is concluded that WR stars could be the progenitors of gamma-ray bursts. This hypothesis predicts the existence of two types of gamma-ray bursts, corresponding to the bimodal mass distribution for stellar relativistic objects, and of three types of optical afterglow, associated with collapses of the CO cores of WR stars that are single, in WR+O binaries, and in hypothetical WR+(A–M) systems. The paper also briefly examines a model of gamma-ray bursts as transient phenomena in the early stages of the evolution of galaxies ($z > 1$), when very massive stars ($M > 100M_\odot$) weak in heavy elements could form. Such massive stars should also lose their hydrogen envelopes and be transformed into massive WR stars, whose collapses could be accompanied by gamma-ray bursts. It is suggested that WR galaxies are the most probable candidates for the host galaxies of gamma-ray bursts. © *2001 MAIK "Nauka/Interperiodica".*

1. INTRODUCTION

The nature of cosmic gamma-ray bursts has not lost its urgency as a problem in modern astrophysics, in spite of the great deal of progress that has recently been made in this field. The current state of this problem has been described many times in the literature (see, for example, the reviews [1, 2] and references therein). Observations of X-ray [3], optical [4], and radio [5] afterglows from gamma-ray bursts carried this phenomenon from the specialized area of high-energy astrophysics to the wide field of all wavelengths accessible to astronomy. The high accuracy of the localization of optical and radio afterglows made it possible to begin searches for promising astronomical objects in the error boxes of gamma-ray bursts with afterglows, and to establish an unambiguous connection between the bursts and distant galaxies [6].

As of the end of September 2000, the state of gamma-ray burst statistics was the following [7]: of ~90 bursts localized with accuracy to within several arcminutes, X-ray afterglows were observed in 34, optical afterglows in 21, and radio afterglows in 14. In addition, X-ray afterglows have been detected in ~90% of bursts that have been observed with an X-ray telescope within a short time (several hours) after the burst. Redshifts have been determined for more than 15 bursts via optical spectroscopy of their afterglows or the host galaxies, making it possible to establish the burst luminosity and energy based on the observed flux (see below). The isotropic maximum luminosities of these bursts lie in a broad range from $\sim 10^{57}$ to $\sim 10^{59}$ photon/s in the BATSE 50–300 keV energy range [8], and the total energy released in this range is typically from $\sim 3 \times 10^{51}$ to $\sim 2 \times 10^{54}$ erg [9]. The burst GRB 980425, which is associated with the peculiar type Ic supernova SN 1998bw in

the nearby galaxy ESO 184-G82 ($z = 0.0085$), is thus far unique [10]. The energy released in this burst is $\Delta E \sim 10^{48}$ erg—four orders of magnitude lower than the characteristic value for other bursts, 10^{52} erg. The energy ΔE_x released in the 2–10 keV range in early X-ray afterglows varies from 1% to ~100% (on average, 10%) of the energy released in gamma rays ΔE_γ [11].

Based on the very successful relativistic fireball model [12] for the afterglows of gamma-ray bursts [12] (for more detail see also review [13]), the general opinion about the nature of gamma-ray bursts with afterglows is converging to the following picture. For some (not precisely known) reason, a "fireball" consisting of photons and leptons with a small admixture of baryons (with mass $\Delta M_b \sim 10^{-5} M_\odot$) forms in a medium (interstellar or intergalactic) and expands with relativistic Lorentz factor $\Gamma = 1/\sqrt{1-(v/c)^2} \sim 200$. The relativistic expansion speed and small number of baryons in the fireball are deduced from the observed non-thermal spectra of gamma-ray bursts and the short (about one millisecond) timescale for variability of the gamma radiation (the so-called compactness problem; see the detailed discussion in [14]). During the expansion, the initial thermal energy is transformed into kinetic energy of a relativistic shock, which is decelerated in the surrounding medium. Relativistic electrons accelerated in the shock front emit their kinetic energy in the form of synchrotron radiation, giving rise to an X-ray, optical, and radio afterglows. The so-called internal shock model [15] proposes that the gamma-ray burst itself arises during interactions between these shock waves, which are generated as part of the primary energy release of a "central engine." In spite of the simplicity and elegance of this model, it provides a far from adequate description of the observed properties of gamma-ray bursts (see, for example, the alternative models and critical comments in [16]).

The requirements for the "central engine" itself can be reduced to two main points:

(a) it must be able to supply ~10^{52} erg of energy over 10–100 s (the characteristic duration of "long" bursts, which are currently the only ones that can be accurately localized; little is known about short bursts with durations of about a second, except that they are uniformly distributed on the sky—an optical afterglow has been observed only from the short burst GRB 000301C, which had a duration of 2 s [17]);

(b) the average frequency of events must be about one per million years per average galaxy (assuming the emission is isotropic and the galaxies are single).

The beaming of the radiation lowers the energetic requirements and raises the event rate to various degrees: if the energy release occurs in a small cone with opening angle θ_γ, the energy inferred from the observed total flux F_γ will be a factor of $\theta_\gamma^2/4$ lower than the energy calculated using the isotropic formula $\Delta E_\gamma = 4\pi d^2 F_\gamma$.[1] The beaming can be formed by an external medium or magnetic field, or be specified by other initial conditions (see the detailed analysis in [18]).

These requirements for the central engine are satisfied by a number of astrophysical sources. The most popular models are the following.

(1) The merging of two neutron stars and/or black holes (proposed by Blinnikov *et al.* [19] in 1984). The fireball is formed during the annihilation of neutrino–antineutrino pairs.

(2) Core collapse in massive stars. In particular, in the hypernova model of Paczynski [20], energy is released during the formation of a rapidly rotating black hole with a mass of about ten solar masses in a strong magnetic field of ~10^{15} G via the Blandford–Znajek mechanism [21]. In models developed by the group of S. Woosley and his colleagues (see, for example, [22, 23], the fireball is formed by neutrino radiation from an accretion disk formed from a collapsing core around a black hole. The resulting collimated relativistic jet "ignites" the stellar envelope and generates gamma radiation.

(3) The electromagnetic model of Usov [24], in which the source of energy is the rotational energy of a young neutron star with a very strong magnetic field.

(4) The recently proposed model of Gershteĭn [25], in which gamma-ray bursts occur during the collapse of massive, non-rotating Wolf–Rayet stars. Internal shock waves are formed by an electron–positron plasma during the nonstationary, pulsational thermonuclear burning of matter near the proto-neutron star.

More and more astronomical observations of gamma-ray bursts and their afterglows in various wavelength ranges point toward a connection between gamma-ray bursts and the evolution of massive stars. The following facts support this view.

(1) The enhanced rate of star formation in galaxies identified as hosts of gamma-ray bursts, which sometimes exceed the star-formation rate in our Galaxy by an order of magnitude [26]. This follows from observations made using the most sensitive ground-based telescope and the Hubble Space Telescope [27].

(2) The high absorption along the line of sight to the sources of gamma-ray bursts $N_H \approx 10^{22}$–10^{23} cm^{-2}, derived from observations of X-ray and optical afterglows [28]. Such high densities are characteristic of giant molecular clouds.

[1] The total energy release is $E = \frac{1}{4\pi}\int E(\theta) d\Omega = \int \frac{E_0}{2} f(\theta) \sin\theta d\theta$ in the general case of an arbitrary, axisymmetrical directional beam for the radiation. The relativistic motion of the moving volume changes the appearance of the beam in the rest frame of the observer, but preserves the total energy released.

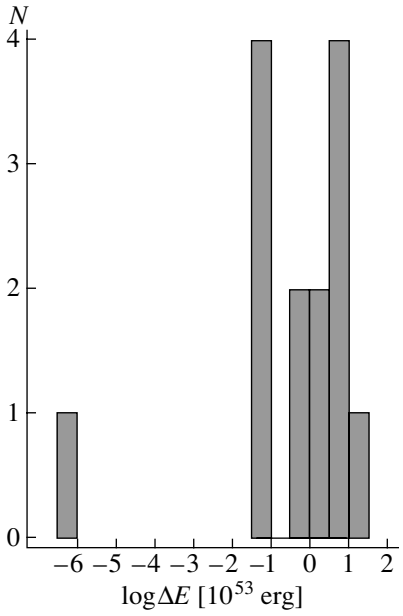

Fig. 1. Distribution of the total energy release ΔE (in units of 10^{53} erg/s) of gamma-ray bursts with known redshifts from Table 1.

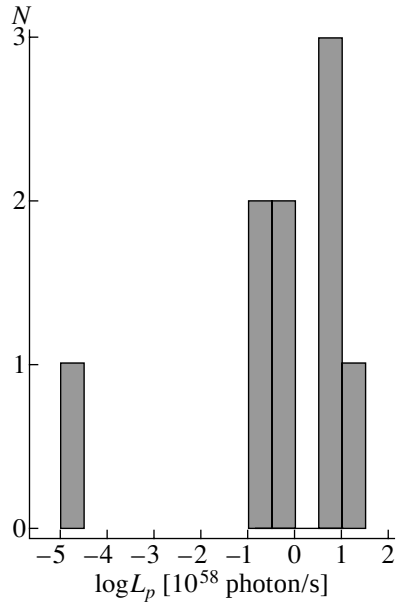

Fig. 2. Distribution of peak fluxes L_p (in units of 10^{58} photon/s) of gamma-ray bursts with known redshifts from Table 1.

(3) The distribution of gamma-ray bursts in the plane of the sky relative to the centers of their host galaxies systematically coincides with the distribution of massive stars [29].

(4) Observations of intense iron lines in the X-ray afterglows of several gamma-ray bursts [30, 31] suggest the presence of a dense medium enriched in heavy elements about 10^{15}–10^{16} cm from the burst location.

These facts lead us to conclude that at least these gamma-ray bursts are associated with the evolution of massive stars (either single or in binary systems).

The evolution of the most massive stars gives rise to Wolf–Rayet (WR) stars, due to the intense outflow of the stellar winds in the case of single stars, or to the overflow of the stars' hydrogen envelopes onto their companions during mass exchange in binary systems. In both cases, the helium core of the massive star is laid bare, and ends its evolution with collapse followed by the formation of a relativistic object. The compactness of the supernova progenitor could lead to peculiarity in the observed supernova explosion (type Ib or Ic). In addition, the absence of an extended hydrogen envelope around the compact progenitor could facilitate the transformation of the collapse energy into observable gamma radiation.

In the current paper, we analyze the observed distribution of isotropic energy release of gamma-ray bursts with known redshifts, and compare this with the distribution of final masses of the CO cores of WR stars and of the associated relativistic objects (neutron stars and black holes) implied by observations. We will show that the observed characteristics of WR stars (both single and in binaries) are consistent with the idea that WR stars could be sources of cosmic gamma-ray bursts. We briefly discuss the hypothesis that gamma-ray bursts are transient phenomena that occur in the early stages of formation of galaxies, associated with the evolution of very massive, metal-weak stars ($M > 100M_\odot$) in these stages.

2. THE ENERGETICS OF COSMIC GAMMA-RAY BURSTS

As noted in the Introduction, the energies released by gamma-ray bursts with known redshifts cover a broad range. The task of establishing the energies released by bursts encounters a number of problems, even in the case of bursts with known redshifts. First, due to the high background level, the total received flux yields only a lower limit to the energy release. Further, it is necessary to take into account the (time variable) spectrum and K correction. Finally, the data have been acquired using a variety of instruments (inhomogeneity of the sample). This last problem is removed for bursts recorded by BATSE on the Compton Gamma-Ray Observatory (six bursts with known z and fluxes [9]), and we will use these data below, taking into account the observed burst spectra. We also include in our sample several bursts with known redshifts recently recorded by BATSE, whose energy releases have been reported in original communications: GRB 991208, GRB 000131, GRB 000301C, GRB 000418, and GRB 000926. These data are collected in Table 1 and presented in Figs. 1 and 2 in the form of histograms. To determine the photometric distance $d_l(z)$, we assumed a

Table 1. Gamma-ray bursts with known energy

GRB	z	d_i^1, 10^{28} cm	F_γ, 10^{-5}, erg/cm^2 (10–2000 keV)	Ref.	ΔE_γ, erg	F_p^2, photon/s (50–300 keV)	L_p, 10^{58} photon/s
000926	2.066:	5.81	2.2	[32]	3.04		
000418[3]	1.118	2.73	1.3	[33]	~0.6	–	
000301C[4]	2.03	5.69	>0.05	[34]	~0.07	~5	6.7
000131	~4.5	14.75	1	[35]	5		
991208[5]	0.706	1.55	10	[36]	~1.8	–	
990712	0.430	0.85	–				
990705	0.84	1.91	?	[37]			
990510	1.619	4.30	2.26	[9]	2.0	8.16	7.3
990123	1.6	4.25	26.8	[9]	23	16.4	14
980703	0.967	2.28	2.26	[9]	0.75	2.6	0.86
980613[6]	1.096	2.66	0.17	[38]	0.072	0.63	0.27
971214	3.412	10.6	0.944	[9]	3.0	2.3	7.4
970828	0.958	2.25	9.6	[9]	3.1	–	
970508	0.835	1.90	0.317	[9]	0.08	1.2	0.29
970228[6]	0.695	1.52	~0.2	[38]	0.034	3.5	0.60
980425	0.0085	0.013	0.32	[10]	7×10^{-6}	0.96	2.1×10^{-5}

[1]Flat Universe, $\Omega_m = 0.3$, $\Omega_\Lambda = 0.7$, $H_0 = 60$ km s^{-1} Mpc^{-1}.
[2]Peak fluxes from [8].
[3]Total flux at 25–100 keV.
[4]Peak flux $F_p = 3.7\, F_{\rm crab}$, single-peaked profile, duration 10 s; no data on the total flux are available. For other indirect estimates of the total energy released, see [39].
[5]Total flux F_γ at energies > 25 keV.
[6]Total flux F_γ at energies > 20 keV.

flat cosmology with cosmological constant ($\Omega_m = 0.3$, $\Omega_\Lambda = 0.7$, $H_0 = 60$ km s^{-1} Mpc^{-1})

$$d_l(z) = (1+z)\frac{c}{H_0}\int_0^z \frac{dz}{\sqrt{\Omega_m(1+z)^3 + \Omega_\Lambda}}. \qquad (1)$$

For a known total flux F_γ in the limited energy interval of a detector, the energy release in the rest frame of the source is $\Delta E_\gamma = 4\pi d_l(z)^2 F_\gamma/(1+z)$. We include in the table data on the total fluxes of bursts from the BATSE catalog (50–300 keV) [9] and the peak photon luminosity of the bursts L_p (photon/s) [8]. This last quantity is less subject to selection effects, and characterizes the internal process of energy release. A separate row in the table shows data for the burst GRB 980425, with its anomalously low energy release, which illustrates the possibility of a bimodal energy distribution for the gamma-ray bursts.

We can see from Table 1 and Figs. 1 and 2 that the energy release of gamma-ray bursts ΔE covers the wide range from $\approx 2 \times 10^{54}$ erg to $\approx 3 \times 10^{51}$ erg, and even to $\sim 10^{48}$ erg. A group of four bursts with energy releases up to 10^{52} erg, and another group of nine bursts with energy releases above 10^{52} erg can clearly be distinguished. The burst GRB 980425 is isolated, with its anomalously low energy release. The broad range of energy releases for gamma-ray bursts with known redshifts (even excluding GRB 980425) is usually explained as reflecting a wide range of luminosity functions for the bursts $\phi(E)$ (see also [18, 40]), although alternative models with a universal characteristic energy release $E_0 \sim 5 \times 10^{51}$ erg and a complex directional beam $f(\theta)$ are also possible [41]. Here, we will assume that the luminosity function of the main group of gamma-ray bursts occupies no more than two and a half orders of magnitude, and that the energy distribution of the bursts may be bimodel (GRB 980425).

THE OBSERVED DISTRIBUTIONS OF THE MASSES OF WR STARS, THEIR CO CORES, AND RELATIVISTIC OBJECTS IN BINARY SYSTEMS

According to our current understanding of WR stars [42, 43], they are essentially the naked helium cores of initially very massive stars that have lost their hydrogen envelopes. Core collapse in WR stars leads to the for-

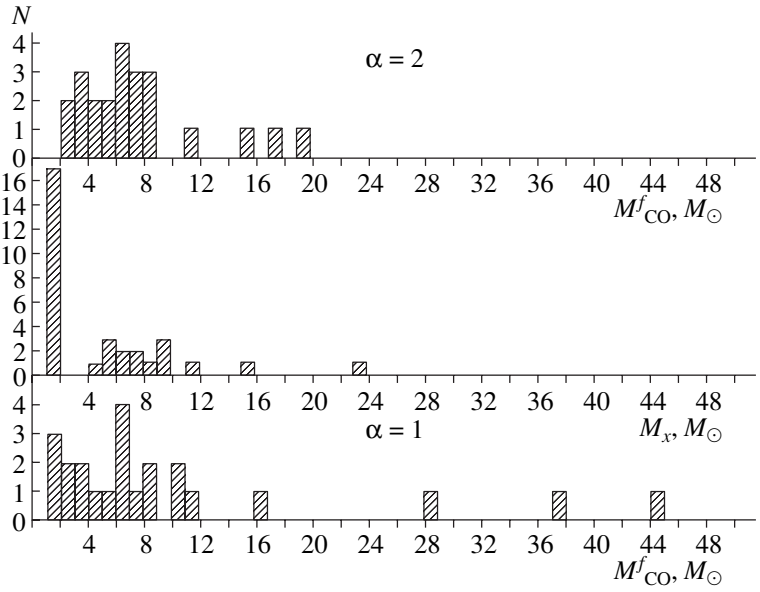

Fig. 3. Final masses of the CO cores of WR stars M_{CO} computed using the observed rate of mass loss via the stellar wind $\dot{M} \propto M^\alpha$ for $\alpha = 2$ (upper) and $\alpha = 1$ (lower). The distribution of masses of known neutron stars and black holes in binary systems is presented in the middle section of the figure. The figure is adopted from [49].

mation of relativistic objects (neutron stars and black holes), and can be accompanied by a supernova of type Ib (if helium absorption lines are present in the supernova spectrum at maximum brightness) or type Ic (if such helium lines are absent or very weak [44]). Final masses for the CO cores of WR stars with known masses, taking into account mass loss via the stellar wind, which depends on the WR mass, are computed in [49]:

$$\dot{M}_{WR} = kM^\alpha. \quad (2)$$

Here, $\alpha = 1$–2, with the preferred value of the spectral index from polarimetric determinations of $\dot{M}_{WR}$ for many WR stars being $\alpha = 1$ [45]. Allowing for the clumpiness of the WR wind [46–48] in [49] implies a coefficient of proportionality k that is a factor of three lower than values derived in earlier studies [50, 51]. This is supported by the fact that the value of $\dot{M}_{WR}$ derived from the secular increase in the orbital period of the eclipsing binary V444 Cyg (WN5+O6, $P \simeq 4\overset{d}{.}2$) using a dynamical method [52, 53] was $0.7 \times 10^{-5} M_\odot$/yr—a factor of three to four lower than the value of $\dot{M}_{WR}$ found for this same system based on radio observations [45]. It is natural to associate this difference with the influence of the clumpy structure of the WR wind, which, if not taken into account, leads to an overestimated $\dot{M}_{WR}$ in the analysis of the radio observations, since the observed radio flux depends on the square of the density n_e [48].

It is emphasized in [49] that, the use of more appropriate values for the spectral index α and proportionality coefficient k in (1) compared to those used in previous studies [50, 51], means that we do not observe a convergence of the final masses of the CO cores of WR stars M^f_{CO} to a single modest value of about several solar masses. On the contrary, M^f_{CO} is distributed continuously over the wide range $(1–2)M_\odot$–$(20–44)M_\odot$ (see Fig. 3). It is also stressed in [49, 54, 55] that the different distributions for the masses of WR stars and of the final (pre-collapse) masses of their CO cores, on the one hand (uniform), and of the observed masses of relativistic objects, on the other hand (bimodal) suggests that the type of object formed during a collapse (neutron star or black hole) depends not only on the mass of the progenitor, but also on other physical factors (rotation, magnetic field, etc.).

Figure 3 presents the distribution of final CO-core masses for well studied WR stars M^f_{CO} for $\alpha = 1$ and $\alpha = 2$ [see Eq. (1)], together with the observed distribution of masses for neutron stars and black holes in binaries M_x from [49]. It is clear that, in the most reasonable case $\alpha = 1$ for WR stars [45], the mass range M^f_{CO} derived observationally covers nearly one and a half orders of magnitude. It is important to note that, due to the relatively small rates of mass loss via the stellar wind $\dot{M}_{WR}$, these results are only weakly model dependent [49].

Table 2 presents the masses and orbital characteristics of WR stars in WR+O binaries from [49]. We can see that the orbital periods of systems with known masses for both the WR and O stars lie in the range $1\overset{d}{.}6$–2900^d, and that 7 of the 23 orbits (~30%) have appreciable eccentricities $e = 0.17$–0.84.

Table 2. Masses and orbital characteristics of WR and O stars in WR + O binaries [49]

System WR+ O	$m_{WR}, M_\odot$	$m_O, M_\odot$	Sp	P, days	e	i
HD 63099	7	11	WC5 + O7	14.305	0	64
γ^2 Vel	21	39	WC8 + O9I	78.5002	0.40	70
HD 90657	17	36	WN4 + O5	8.255	0	57
HD 92740	55.3	20.6	WN7 + O6.5–8.5	80.343	0.56	70
HD 94305	19	40	WC6 + O6–8V	18.82	0	70:
HD 94546	9	26	WN4 + O7	4.9	0	74
HD 97152	11	19	WC7 + O7V	7.886	0	43
HDE 311884	48	57	WN6 + O5V	6.34	0	70
HD 152270	5	14	WC7 + O5	8.893	0	45
CV Ser	14	29	WC8 + O8-9V–III	29.707	0	67
HD 186943	16	35	WN4 + O9V	9.5550	0	56
HD 190918	13	29	WN5 + O9.5I	112.8	0.48	15
V444 Cyg	9.3	27.9	WN5 + O6	4.212424	0	78.7
HD 193793	27:	50:	WC7 + O5V	2900	0.84	44:
CX Cep	20	28.3	WN5 + O5V	2.1267	0	74
HD 211853	14:	26:	WN6 + O+?	6.6884	0	78
CQ Cep	17	20	WN6–7 + O9II–Ib	1.641246	0	78
B22	12:	35:	WC6 + O5-6V–III:	14.296	0.17	71:
B32	5	30	WC4 + O6V–III:	1.91674	0	29
AB8	14	52	WO4 + O4V	16.644	0.19	41
HD 5980	8:	27:	WN4 + O7I	19.266	0.49	89
AB6	8	47	WN3 + O7	6.681	0	68
HD 193928	40	30	WN6 + O	21.64	0.02	68

The fraction of WR+O binaries among Galactic WR stars is no more than 42%. According to [49, 54, 56] apart from (WR+O) binaries, there should also exist WR+(A–M) binaries with low-mass A–M companions among WR stars. Such WR+(A–M) binaries could be the progenitors of low-mass X-ray binaries with neutron stars and black holes [54]. Taking into account this hypothetical class of WR binaries, the fraction of WR binary systems in the Galaxy with nonrelativistic companions could exceed 50%. Data for the Large and Small Magellanic Clouds suggest that the total fraction of WR binaries in other galaxies is comparable [49]. There also exist WR+C binary systems with relativistic companions (one example is Cyg X-3).

According to the most recent spectropolarimetric data [57], ~20% of WR stars exhibit rapid axial rotation. This could mean that, during the supernova explosion, the rapid rotation of the WR core "drags out" the time for the collapse, so that the ejected carbon–oxygen envelope receives a larger fraction of the energy than in the ordinary type Ib supernovae associated with the explosions of massive helium (WR) stars. This could explain why GRB 980425 is associated with the peculiar type Ic supernova SN 1998bw, rather than with an ordinary type Ib/Ic supernova. Model calculations indicate that the observed optical light curve of this supernova demands an unusually high kinetic energy for the envelope, $\sim 6 \times 10^{51}$–10^{52} erg [58, 59].

4. WOLF–RAYET STARS AS POSSIBLE SOURCES OF GAMMA-RAY BURSTS

Let us list arguments that, in our view, support the model of WR stars as gamma-ray burst sources.

(1) *Energetics.* The observed energy release is $E_1 \approx 10^{48}$ erg, $\Delta E_2 \simeq 10^{51}$–$10^{54}$ erg and the range of masses for the CO cores of WR stars before collapse is $M_{CO}^f \simeq (2\text{–}40)M_\odot$. The total energy released during the collapse is $E_G \sim GM_c^2/R_c$, where M_c is the mass of the compact remnant and R_c is its radius. In a collapse to a black hole without significant ejection of mass (which is natural for the collapse of the compact CO cores of WR stars), the available energy given the observed range of masses for the compact remnants is 10^{53}–10^{56} erg; i.e., conversion of 1% of the collapse energy into kinetic energy of shock waves, with the subsequent radiation of energy, is sufficient to explain the observed broad luminosity function of bursts [25]. Note that, during

collapse to a black hole without ejection of mass, $R_c \propto M_c \propto M_{CO}$, and the energy range of the gamma-ray bursts will be proportional to the mass range of the collapsing cores, as is observed (Figs. 1, 3). In view of the absence of powerful hydrogen envelopes around WR stars, the transformation of the released energy into gamma radiation could be facilitated [25], and the collapse could be accompanied by directly observable manifestations of this radiation.

(2) *The large scatter in the energy* of gamma-ray bursts (~2.5 orders of magnitude) is consistent with the appreciable scatter in the final masses of the CO cores of WR stars (1.5 orders of magnitude).

(3) *Bimodality of the distributions of the energies of gamma-ray bursts and the masses of relativistic objects.* Low-energy gamma-ray bursts associated with peculiar type Ic supernova (such as GRB 980425) could result from the collapse of CO cores with large angular (rotational) momenta, leading to the ejection of envelopes and the formation of neutron stars, while the collapse of CO cores with lower angular momenta form black holes with higher energies, proportional to the mass of the CO core. The rarity (one of ten) of low-energy gamma-ray bursts could be an observational selection effect, and could also reflect the fact that the fraction of rapidly rotating WR stars is relatively small (~20% [57]).

(4) *The association of gamma-ray bursts with star-forming regions in their host galaxies* is natural in all models in which the bursts are the result of core collapse in massive stars.

(5) *Variety of optical afterglows.* As was first noted in [60], various optical effects associated with the irradiation of the secondary star with hard electromagnetic radiation (the reflection effect) are possible for gamma-ray bursts in binary systems. These could be manifest as deviations from a power-law flux decay in the afterglows at times $\Delta t_{opt} = D/c$ (D is the distance to the optical component and c is the speed of light), which indeed are observed for some gamma-ray bursts (for example, in GRB 980326 three weeks after the burst [61]). In particular, we have for the parameters of the WR+O binary V444 Cyg with orbital period $P = 4^d.2$, $D \approx 40R_\odot$, and the time delay is $\Delta t_{opt} \approx 100$ s; for the parameters of the CV Ser system, $\Delta t_{opt} \approx 300$ s. Note that an unusually bright optical afterglow ($V \simeq 9^m$) in the burst GRB 990123 was observed 50 s after the onset of the gamma-ray burst [62]. Another example is the peculiar achromatic variations of the optical afterglow of GRB 000301C [39, 63]. The observed two peaks separated by about three days could be a manifestation of binarity (the orbital period) of the system in which the gamma-ray burst occurred (for example, due to modulation of the stellar wind before collapse of the orbital motion). The alternative explanation of the light curve as a result of gravitational microlensing [64] is much less likely. Note that orbital periods of several days are typical of WR+O systems (Table 2).

Modeling of observed gamma-ray burst afterglows [65] shows that some afterglows (GRB 990123, GRB 990510) can be adequately described assuming a surrounding medium with constant density, while others (GRB 970228, GRB 70508) require that the wind of the progenitor fall off with the inverse square of the distance from the star. The case of a surrounding medium with nearly constant density could correspond to massive O+O or WR+O binary systems, in which there are intense collisions of the powerful stellar winds. Therefore, the evidence for a constant-density medium should not be taken as an argument against models in which gamma-ray bursts are associated with core collapse in massive stars.

These arguments provide a firm basis to seriously consider WR stars as possible progenitors of gamma-ray bursts. However, a successful explanation of the phenomenon of gamma-ray bursts requires that the burst rate be in agreement with the frequency of core collapse in WR stars.

5. DISCUSSION

5.1. The Problem of the Frequency of Events

It is difficult to estimate the true frequency of gamma-ray bursts from existing observations due to selection effects. The careful analysis of non-trigger BATSE gamma-ray bursts performed by Stern *et al.* [66] indicates that the total number of bursts per year is 1200–1300 (for a threshold total flux $F_{tr} = 0.1$ photon/cm^2). According to these data, the rate of gamma-ray bursts per year in a unit co-moving volume is a factor of four higher than the rate calculated for a BATSE threshold of 0.5 photon/cm^2 [40], and is

$$\mathcal{R}_{GRB} \sim 10^{-9}\ \mathrm{yr}^{-1}\ \mathrm{Mpc}^{-3},$$

that is, about 10^{-7} per year per average galaxy with mass $10^{11}M_\odot$. This is several orders of magnitude lower than the total rate of type Ibc supernovae ($\mathcal{R}_{SNIbc} \sim 3 \times 10^{-5}$ yr^{-1} Mpc^{-3} [67]). It is usually thought (see, for example, [8]) that this discrepancy is due to both beaming of the gamma-ray bursts (jets) and the fact that not every type Ib/c supernova gives rise to a gamma-ray burst. However, note the following.

(1) Mean estimates of the frequency of gamma-ray events per galaxy do not take into account the strong evolution of the star-formation rate in galaxies (i.e., essentially, the intrinsic rate is underestimated relative to the rate of supernovae, which often explode in distant galaxies due to the general increase in the star-formation rate with redshift).

(2) Due to the steep power-law dependence of the initial mass function, the supernova rate is determined from the lower limit to the mass of stars that end their evolution in supernova explosions (usually taken to be $\sim 8M_\odot$). The initial mass function for very massive stars is poorly known, especially in sites of star formation.

Let us present a simple estimate of the mean rate of formation of WR stars in the Galaxy. We will take the star-formation rate to be constant. The rate of formation of solar-type stars $\mathcal{R}_\odot$ is about one star per year, and the total number of such stars in the Galaxy is $N_\odot \simeq 10^{11}$. The number of WR stars is estimated to be 10^3–5×10^3 (we adopt $N_{\rm WR} = 2 \times 10^3$). Since the lifetime of solar-type stars is $\Delta t_\odot \simeq 10^{10}$ yr, and the mean lifetime of a WR star is $\Delta t_{\rm WR} \simeq 5 \times 10^5$ yr, we estimate the rate of formation of WR stars as

$$\mathcal{R}_{\rm WR} = R_\odot \frac{N_{\rm WR}}{N_\odot}\frac{\Delta t_\odot}{\Delta t_{\rm WR}} \sim \frac{1}{1000}\ {\rm yr}^{-1}. \quad (3)$$

It is obvious that WR stars are born on average 10 000 times more often than gamma-ray bursts, and we must explain this discrepancy. There are two possible solutions to this problem: (a) postulate the existence of narrow (opening angles of several degrees) jets, or (b) assume spherically symmetrical energy release, but invoke "hidden parameters" of the collapse (rotation, magnetic field, etc.).

The question of jets in gamma-ray bursts is not yet resolved, since the observed breaks in the power-law light curves of burst afterglows, which can be interpreted as evidence for jets [68], can also be explained in other ways (see, for example, [69]). We also wish to draw attention to the fact that three WO stars are known of 200 Galactic WR stars [49]. Accordingly, their birth rate in the Galaxy is nearly two orders of magnitude lower, i.e., about $1/10^5$ yr^{-1}. These are the most compact WR stars; one is known to have a mass of $\sim 14 M_\odot$ [49]. If we suppose that it is precisely during the collapses of these stars that gamma-ray bursts originate, the requirement for collimated jets is appreciably reduced.

Let us further consider the two gamma-ray burst models that invoke WR stars: the hypernova model of Paczynski [20] and the model of Gershteĭn [25]. In the hypernova model [20], the rapidly rotating core of a massive star in a binary collapses, with the formation of a Kerr black hole with a mass of about $10 M_\odot$. The efficient extraction of the rotational energy of the black hole via the Blandford–Znajek mechanism requires a strong magnetic field of 10^{15}–10^{16} G. Essentially, this combination of exotic collapse parameters leads to the observed rarity of gamma-ray bursts. In this model, narrow jets form naturally [solution (a) above].

In the model of Gershteĭn [25], a nonrotating WR star collapses into a black hole, and the energy release is spherically symmetrical. As we have seen, this can explain the observed range of energies (via the connection with the masses of the collapsing CO cores); but it remains unclear why on average only 1 of 10 000 collapses leads to the formation of a gamma-ray burst. It is possible that, due to the extreme complexity of the process of formation of a relativistic object, the product of the collapse (formation of a neutron star or black hole) depends somewhat randomly on many parameters [70], and solution (b) is realized.

5.2 Gamma-ray Bursts as a Transient Galactic Phenomenon

There is another way to explain the observed association of cosmic gamma-ray bursts with star-forming regions in distant galaxies and their low rate of formation per galaxy. Powerful gamma-ray bursts could be transient (temporary) phenomena that occur only in the early stages of galactic evolution, similar to the phenomenon of activity in galactic nuclei. An epoch of active star formation in young galaxies is observed at large redshifts $z \sim 1$–2 [71]. In addition, much pre-galactic material at redshifts $z > 2$ was in the form of giant clouds, manifest as absorption lines in the spectra of quasars (the "Lyman α forest"). In the early stages of galactic evolution, very massive stars could form (100–$500 M_\odot$), which collapse into massive black holes. Such stars cannot form from material enriched in heavy elements, due to pulsation instabilities (see [72] and references therein). However, given the low metallicity of matter at the epoch of primary star formation, they could have formed at that time. The generation of gamma-ray bursts during the collapse of such stars is considered in [73], leading to the conclusion that it is not possible for such collapses to give rise to powerful gamma-ray bursts. However, the physical processes in these stars are far from fully understood, and it seems reasonable to think that such massive stars devoid of hydrogen envelopes in the WR stage could be progenitors of gamma-ray bursts. In the framework of this hypothesis, the low energy release of GRB 980425 in a nearby galaxy could be a natural consequence of the lower masses of collapsing stars in star-forming regions at the current epoch. This hypothesis can easily be tested by observations of powerful gamma-ray bursts in nearby galaxies or in galaxies with normal metal contents. The existing spectroscopic data for the host galaxies of gamma-ray bursts suggest that they have relatively low metallicities [74], although it is too early to draw firm conclusions about this.

We also note that, among the multitude of starburst galaxies, a subset of so-called Wolf–Rayet galaxies can be distinguished, which have very high ratios of the numbers of WR and O stars and are relatively deficient in metals [75]. If gamma-ray bursts are associated with massive stars, it is natural to expect them to occur first and foremost precisely in these galaxies. The morphologies of these galaxies are close to irregular or show signs of interaction, underlining their similarity to the host galaxies of some gamma-ray bursts (GRB 990123, for example). It will be possible to elucidate whether distant host galaxies of gamma-ray bursts ($z > 1$) are Wolf–Rayet galaxies from their infrared spectra, which should display broad He II 4686 Å emission.

6. CONCLUSION

The observed broad (and possibly bimodal) distributions of the energies of gamma-ray bursts and of the final masses of the CO cores of WR stars, the association of identified gamma-ray bursts with galaxies showing active star formation, and the variety of the observed optical afterglows all provide evidence in favor of a link between WR stars and the phenomenon of gamma-ray bursts. The observed rarity of gamma-ray bursts could be due to the stochastic nature of the collapses of the CO cores of WR stars. The possible bimodality of the gamma-ray burst energy distribution could reflect the bimodality of the masses of relativistic objects (neutron stars and black holes) formed during the core collapse. We emphasize again that, in contrast to ordinary stars, WR stars are devoid of powerful hydrogen envelopes. This is precisely why WR stars are preferred as progenitors of gamma-ray bursts, since the absence of a hydrogen envelope should facilitate the transformation of the energy of the collapse into the observed gamma radiation.

The proposed association with WR stars yields several verifiable predictions.

(1) Two types of gamma-ray bursts are possible: more energetic bursts with a broad luminosity function, associated with the collapse of CO cores into black holes, and less energetic bursts with a narrower luminosity functions, associated with collapse into neutron stars (GRB 980425?).

(2) Three types of optical afterglow are possible: one type from collapsed single WR stars and two types from collapsed WR stars in binaries (WR+O and WR+(A–M) systems). In these last two cases, it is natural to expect deviations from a single power-law decay of the optical flux due to the reflection of hard radiation off the secondary (at times of 10–1000 s) and the ejection of the envelope of the secondary when it is heated by this hard gamma radiation (at times of tens of days; the mini-supernova effect [60]). In the case of collapse in a binary system, the optical afterglow may be modulated by the orbital period of the system.

(3) The host galaxies of gamma-ray bursts should include WR galaxies with low metal contents and broad He II 4686 Å emission in their infrared spectra.

In conclusion, we note that, along with new observations of gamma-ray bursts and their afterglows, the elucidation of the nature of the bursts requires the detailed development of physical models for the core collapse [20, 23, 25]. Studies of regions of intense star formation using a variety of methods are also important (see, for example, [76]), together with clarification of the initial mass function of the stars forming in such regions.

ACKNOWLEDGMENTS

The authors thank S.S. Gershteĭn, S.I. Blinnikov, T.A. Lozinskaya, Yu.N. Efremov, D.Yu. Tsvetkov, and M.E. Prokhorov for discussions. This work was partially supported by the Russian Foundation for Basic Research (project codes 99-02-16205 and 00-02-17164).

REFERENCES

1. B. I. Luchkov, I. G. Mitrofanov, and I. L. Rozental', Usp. Fiz. Nauk **167**, 743 (1996) [Phys. Usp. **39**, 695 (1996)].
2. K. A. Postnov, Usp. Fiz. Nauk **169**, 545 (1999).
3. E. Costa, F. Frontera, J. Heise, *et al.*, Nature **387**, 783 (1997).
4. J. van Paradijs, P. J. Groot, T. Galama, *et al.*, Nature **386**, 261 (1997).
5. D. A. Frail, S. R. Kulkarni, S. R. Nicastro, *et al.*, Nature **389**, 261 (1997).
6. K. C. Sahu, M. Livio, L. Petro, *et al.*, Nature **387**, 476 (1997).
7. J. Greiner, http://www.aip.de/People/JGreiner/grbgen.html.
8. D. Q. Lamb, astro-ph/0005028 (2000).
9. P. Kumar and T. Piran, Astrophys. J. **535**, 152 (2000).
10. T. Galama, P. M. Vreeswijk, J. van Paradijs, *et al.*, Nature **395**, 670 (1998).
11. J. Heise, Talk presented on the 2nd Workshop GRBs in the Afterglow Era, Rome, 2000.
12. M. J. Rees and P. Meszaros, Mon. Not. R. Astron. Soc. **258**, 41 (1992).
13. T. Piran, Phys. Rep. **314**, 575 (1999).
14. S. I. Blinnikov, Surv. High Energy Phys. **15**, 37 (2000); astro-ph/9911138.
15. M. J. Rees and P. Meszaros, Astrophys. J. Lett. **430**, L93 (1994).
16. V. V. Usov, in *Gamma-Ray Bursts: The First Three Minutes*, Ed. by J. Poutanen and R. Svensson; Astron. Soc. Pac. Conf. Ser. **190**, 153 (1999).
17. B. L. Jensen, J. U. Fynbo, J. Gorosabel, *et al.*, Astron. Astrophys. (in press); astro-ph/0005609.
18. T. J. Loredo and I. Wasserman, Astrophys. J. **502**, 108 (1998).
19. S. I. Blinnikov, I. D. Novikov, T. V. Perevodchikova, and A. G. Polnarev, Pis'ma Astron. Zh. **10**, 422 (1984) [Sov. Astron. Lett. **10**, 177 (1984)].
20. B. Paczynski, Astrophys. J. Lett. **499**, L45 (1998).
21. R. D. Blandford and R. L. Znajek, Mon. Not. R. Astron. Soc. **179**, 433 (1977).
22. S. E. Woosley, Astrophys. J. **405**, 273 (1993).
23. A. MacFadyen and S. Woosley, Astrophys. J. **524**, 262 (1999).
24. V. V. Usov, Nature **357**, 472 (1992).
25. S. S. Gershteĭn, Pis'ma Astron. Zh. (2000) [Astron. Lett. (2000)]; astro-ph/0005078.
26. P. M. Vreeswijk, A. Fruchter, L. Kaper, *et al.*, Astrophys. J. (2000) (in press); astro-ph/0009025.
27. A. Fruchter, http://www.stsci.edu/fruchter/GRB/.
28. T. Galama and R. A. M. J. Wijers, astro-ph/0009367 (2000).
29. J. Bloom, S. R. Kulkarni, and S. G. Djorgovski, Astrophys. J. (2000) (in press); astro-ph/0010176.
30. L. A. Antonelli, L. Piro, M. Vietri, *et al.*, Astrophys. J. Lett. **545**, L39 (2000); astro-ph/0010221.

31. L. Piro, Talk presented on the 2nd Workshop GRBs in the Afterglow Era, Rome, 2000.
32. J. P. U. Fynbo, P. Moller, T. Dall, *et al.*, GCN807 (2000).
33. J. Bloom, C. Diercks, S. G. Djorgovski, *et al.*, GCN661 (2000).
34. S. M. Castro, C. Diercks, S. G. Djorgovski, *et al.*, GCN605 (2000).
35. M. Andersen, J. Hjorth, H. Pedersen, *et al.*, Astron. Astrophys. **364**, 54 (2000); astro-ph/0010322.
36. S. G. Djorgovski, A. Dierks, J. S. Bloom, *et al.*, GCN481 (1999).
37. S. Holland, Talk presented on the 2nd Workshop GRBs in the Afterglow Era, Rome, 2000.
38. M. S. Briggs, D. L. Band, R. M. Kippen, *et al.*, Astrophys. J. **524**, 82 (1999).
39. S. Sagar, V. Mohan, S. B. Pandy, *et al.*, astro-ph/0004223 (2000).
40. M. Schmidt, in *Gamma-ray Bursts*, Ed. by R. M. Kippen, R. Mallozzi, and G. Fishman (American Institute of Physics, New York), AIP Conf. Proc. (2001) (in press).
41. V. M. Lipunov, K. A. Postnov, and M. E. Prokhorov, Astron. Zh. **78**, 276 (2001) [Astron. Rep. **45**, 236 (2001)].
42. B. Paczynski, in *Wolf–Rayet and High Temperatures Stars (IAU Symposium 49)*, Ed. by M. Barry and J. Sahada (D. Reidel, Dordrecht, 1973), p. 143.
43. P. S. Conti, Mem. Soc. R. Sci. Liege **9**, 193 (1976).
44. A. V. Fillipenko, in *Thermonuclear Supernovae*, Ed. by P. Ruíz-Lapuente, R. Canal, and J. Isern (Kluwer, Dordrecht, 1997), p. 795.
45. A. F. J. Moffat, in *Wolf–Rayet Stars: Binaries, Colliding Winds, Evolution (IAU Symposium 163)*, Ed. by K. A. van der Hucht and P. M. Williams (D. Reidel, Dordrecht, 1995), p. 213.
46. A. M. Cherepashchuk, J. A. Eaton, and Kh. F. Khaliullin, Astrophys. J. **281**, 774 (1984).
47. A. F. J. Moffat, L. Drisson, R. Lamontagne, and C. Robert, Astrophys. J. **334**, 1038 (1988).
48. A. M. Cherepashchuk, in *Wolf–Rayet Stars and Interrelation with other Massive Stars in Galaxies (IAU Symposium 143)*, Ed. by K. A. van der Hucht and B. Hidayat (Kluwer, Dordrecht, 1991), p. 280.
49. A. M. Cherepashchuk, Astron. Zh. **78**, 145 (2001) [Astron. Rep. **45**, 120 (2001)].
50. N. Langer, Astron. Astrophys. **220**, 135 (1989).
51. S. E. Woosley, N. Langer, and T. A. Weaver, Astrophys. J. **411**, 823 (1993).
52. Kh. F. Khaliullin, Sov. Astronomy **18**, 229 (1974).
53. A. M. Cherepashchuk, in *Wolf–Rayet Stars: Binaries, Colliding Winds, Evolution (IAU Symposium 163)*, Ed. by K. A. van der Hucht and P. M. Williams (D. Reidel, Dordrecht, 1995), p. 262.
54. A. M. Cherepashchuk, in *Modern Problems of Stellar Evolution (Proceedings of an International Conference in Honour of Professor A. G. Massevitch)*, Ed. by D. S. Wiebe (Zvenigorod, 1998), p. 198.
55. A. M. Cherepashchuk, in *Thermal and Ionization Aspects of Flows from Hot Stars: Observations and Theory*, Ed. by H. J. G. L. M. Lamers and A. Sapar (Tartu, 2000), p. 249.
56. A. M. Cherepashchuk, Space Sci. Rev. **93** (3–4), 473 (2000).
57. T. J. Harries, D. J. Hillier, and I. D. Howarth, Mon. Not. R. Astron. Soc. **296**, 1072 (1998).
58. K. Iwamoto, P. A. Mazzali, K. Nomoto, *et al.*, Nature **395**, 672 (1998).
59. S. E. Woosley, R. G. Eastman, and B. P. Schmidt, Astrophys. J. **516**, 788 (1999).
60. S. I. Blinnikov and K. A. Postnov, Mon. Not. R. Astron. Soc. **293**, L29 (1998).
61. J. S. Bloom, S. R. Kulkarni, S. G. Djorgovski, *et al.*, Nature **401**, 453 (1999).
62. C. Akerlof, R. Balsano, S. Barthelemy, *et al.*, Nature **398**, 400 (1999).
63. N. Masetti, C. Bartolini, S. Bernabei, *et al.*, Astron. Astrophys. **359**, L23 (2000); astro-ph/0004186.
64. P. M. Garnavich, A. Loeb, and K. Z. Stanek, Astrophys. J. Lett. **544**, L11 (2000); astro-ph/0008049.
65. R. A. Chevalier and Z.-Y. Li, Astrophys. J. **536**, 195 (2000).
66. B. E. Stern, Ya. Tikhomirova, M. Stepanov, *et al.*, Astrophys. J. Lett. **540**, L21 (2000).
67. E. Cappellaro, M. Turatto, D. Yu. Tsvetkov, *et al.*, Astron. Astrophys. **322**, 431 (1997).
68. J. Rhoads, Astrophys. J. **525**, 737 (1999).
69. B. Zhang and P. Meszaros, Astrophys. J. (2001) (in press); astro-ph/0011133.
70. E. Ergma and E. P. J. van den Heuvel, Astron. Astrophys. **331**, L29 (1998).
71. P. Madau, H. C. Ferguson, M. E. Dickenson, *et al.*, Mon. Not. R. Astron. Soc. **283**, 1388 (1996).
72. I. Baraffe, A. Heger, and S. E. Woosley, Astrophys. J. (2000) (in press); astro-ph/009410.
73. C. L. Fryer, S. E. Woosley, and A. Heger, Astrophys. J. (2000) (in press); astro-ph/0007176.
74. S. G. Djorgovski, Talk presented on the 2nd Workshop GRBs in the Afterglow Era, Rome, 2000.
75. P. S. Conti, Astrophys. J. **377**, 115 (1991).
76. Yu. N. Efremov, Usp. Fiz. Nauk **170**, 899 (2000).

Translated by D. Gabuzda

Astronomy Reports, Vol. 45, No. 7, 2001, pp. 527–537. Translated from Astronomicheskiĭ Zhurnal, Vol. 78, No. 7, 2001, pp. 613–624.

Observations of Five Supernovae in 1995–1997

D. Yu. Tsvetkov[1], N. N. Pavlyuk[1], and E. P. Pavlenko[2]

[1]*Sternberg Astronomical Institute, Universitetskiĭ pr. 13, Moscow, 119899 Russia*

[2]*Crimean Astrophysical Observatory, p/o Nauchnyĭ, Crimea, 334413 Ukraine*

Received October 1, 2000

Abstract—We present the results of photometric observations of the type Ia supernovae SN 1995al, 1996bo, 1996bk, the type Ib/c supernova SN 1997X, and the type II supernova SN 1996an. The photometric characteristics of SN 1995al are close to the average for type Ia supernovae. Our analysis has revealed possible peculiarities in the light-curve shape and deviations from the average photometric parameters for SN 1996bk and 1996bo. Sn 1996an probably belongs to type IIP. The light curve of SN 1997X resembles that of the type Ic supernova SN 1994I. Light-curve parameters and absolute magnitude estimates are presented. © *2001 MAIK "Nauka/Interperiodica".*

The present work represents a continuation of our program of systematic observations of supernovae. We carried out photometric observations of SN 1995al, 1996an, 1996bk, 1996bo, and 1997X from November 1995–March 1997 at the Sternberg Astronomical Institute (SAI) and Crimean Astrophysical Observatory (CrAO). Figure 1 presents images of these supernovae.

1. OBSERVATIONS AND REDUCTION

Our observations of the supernovae and surrounding comparison stars were made using the following telescopes and equipment.

(1) For photographic observations of the supernovae, we used the 50-cm meniscus telescope of the SAI Crimean Laboratory with the standard combinations of emulsions and filters: ZU-21 or NT-1AS emulsion with a BS-8 filter for the *B* band and Kodak 103aD or A-600 emulsion with a ZhS-17 filter for the *V* band.

(2) For video observations of the supernovae, we used the CrAO 50-cm meniscus telescope with *B, V,* or *R* filters or without any filter. The equipment is described in [1]. The images were recorded on photographic film.

(3) For photoelectric observations of SN 1995al and its comparison stars, we used the 60-cm reflector of the SAI Crimean Laboratory with the *UBV* photoelectric photometer designed by V.M. Lyutyĭ.

(4) For CCD observations of SN 1996an, its comparison stars, and the parent galaxies of the supernovae, we used the 60-cm reflector of the SAI Crimean Laboratory and the SAI 70-cm reflector and 30-cm refractor in Moscow. ST-6, ST-7, and ST-8 CCD cameras with various filter sets approximately reproducing the Johnson–Cousins *BVRI* system were used. SN 1996an was also observed by V.V. Vlasyuk and V.O. Chavushian with the 1-m telescope of the Special Astrophysical Observatory (SAO) equipped with an ISD017A CCD chip and *BVRI* filters.

We reduced the photographic plates and films taken with the video equipment using several methods. It is apparent from Fig. 1 that all the program supernovae are located in regions of their parent galaxies with strong and non-uniform backgrounds, complicating the reduction of the images.

Most of the images were digitized using an automatic microdensitometer or a device with an ST-7 CCD camera as a light detector. We reduced the digitized images in the IRAF package. Each photograph's characteristic curve was plotted using the comparison-star images and, for the video photographs, also using a printed artificial photometric standard. The first brightness estimate for a supernova was made by measuring the central density on its image after subtracting the average measured or interpolated background of the galaxy. We then used the characteristic curve to translate the densities into intensities. A CCD image of the galaxy taken after the supernova was no longer visible was transformed to achieve the best fit to the photographic image by varying the pixel size and moving and rotating the galaxy image. Further, we normalized the galaxy image and subtracted it from the image of the galaxy with the supernova. We determined the supernova's magnitude via aperture photometry relative to comparison stars.

Some of the plates and films were also measured with an MF-2 microphotometer with a constant-size diaphragm; the supernova brightnesses were estimated from the characteristic curves after the subtraction of the averaged or interpolated backgrounds for their parent galaxies.

We were able to derive measurement errors by comparing the brightness estimates obtained using different methods. The main sources of error were uncertainties in measuring or interpolating the galaxy's average

1063-7729/01/4507-0527$21.00 © 2001 MAIK "Nauka/Interperiodica"

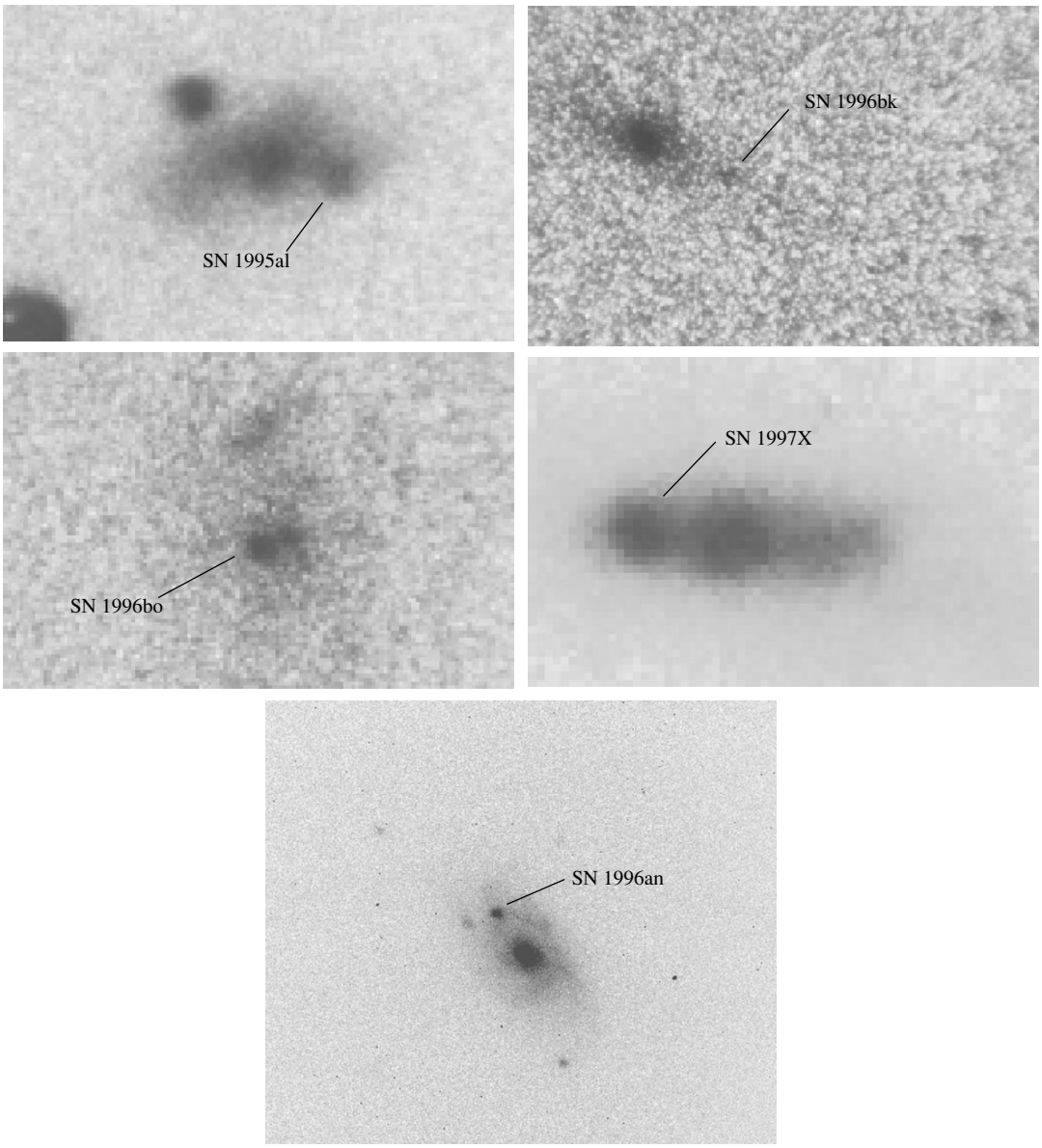

Fig. 1. Images of the program supernovae. Presented for SN 1995al, 1996bk, and 1996bo are photographs taken with the SAI 50-cm telescope ($2' \times 1'.4$ field); for SN 1997X, a video image taken with the CrAO 50-cm telescope ($37'' \times 26''$); and for SN 1996an, a CCD image obtained with the SAI 60-cm telescope ($4'.2 \times 3'.7$). In all images, north is up and east to the left.

background, and the impossibility of completely removing the galaxy images, due to the different structure of the photographic and CCD images and nonlinear effects in the photographic emulsions that were not completely eliminated in our reduction of the digitized images. The best accuracy, about $0^m.1$, was achieved only in the most favorable cases of rather high contrast between the supernova and galaxy images, with the supernova brighter than the detection limit by 2 to 3 magnitudes. For most of our observations, the uncertainties are $\sim 0^m.2$–$0^m.3$, though they can be as high as $0^m.5$ for some photographs.

We obtained photoelectric observations of the comparison stars in the usual way relative to standards from the catalog [2], selected to be within 3° of the supernovae. The accuracy in the resulting magnitudes was from $0^m.01$ to $0^m.1$ for stars fainter than $14^m.5$–15^m.

Our CCD observations of the comparison stars were made on nights with stable transparency. Landolt's standards [3], as well as standards around the program stars selected from [2], were observed on each night. On some nights, we also observed the cluster M 67 [4], to improve the accuracy of the coefficients for reduction from the instrumental to the standard system. We reduced the observations with the IRAF package using

Table 1. Comparison star magnitudes

Star	α	δ	*U*	*B*	*V*	*R*
3021–1	$9^h50^m40^s.35$	33°30′36″.1	10.81	10.72	10.32	–
3021–2	9 51 01.50	33 32 36 .7	12.02	11.87	11.23	11.00
3021–3	9 51 25.49	33 32 58 .6	13.77	13.77	13.25	–
3021–4	9 51 16.00	33 34 50 .2	15.18	14.73	13.83	–
3021–5	9 51 21.83	33 29 22 .5	14.79	14.73	14.14	–
3021–6	9 50 58.55	33 33 27 .5	–	15.18	14.52	14.22
3021–7	9 50 43.49	33 36 59 .7	16.10	15.38	14.63	–
3021–8	9 51 02.46	33 34 54 .5	–	16.72	16.05	15.71
3021–9	9 51 06.09	33 34 03 .7	–	17.37	16.36	15.80
1084–1	2 46 39.20	–7 36 42 .0	–	13.13	12.29	–
1084–2	2 46 22.14	–7 31 52 .5	–	14.89	14.07	–
1084–3	2 46 21.21	–7 34 59 .6	–	14.81	14.29	–
1084–4	2 46 25.50	–7 35 10 .1	–	15.67	14.66	–
1084–5	2 45 36.19	–7 32 21 .8	–	16.87	16.05	–
1084–6	2 46 05.14	–7 33 36 .4	–	18.01	16.86	16.14
5308–1	13 47 06 .75	60 54 05 .7	13.65	13.13	12.17	–
5308–2	13 47 03 .28	61 01 00 .6	15.47	14.22	13.11	–
5308–3	13 47 12 .57	60 58 12 .5	15.50	14.74	13.78	–
5308–4	13 46 55 .80	60 56 06 .3	15.11	15.11	14.33	–
5308–5	13 46 47 .82	60 59 48 .5	17.3	15.95	14.74	–
673–1	1 48 34 .20	11 32 35 .3	10.89	10.81	10.18	–
673–2	1 48 21 .31	11 22 34 .2	13.92	13.79	13.11	–
673–3	1 48 10 .92	11 27 16 .2	14.29	14.21	13.53	–
673–4	1 48 25 .91	11 28 14 .8	15.18	14.58	13.61	–
673–5	1 48 10 .46	11 24 46 .3	15.47	15.10	14.21	–
4691–1	12 48 00 .31	–3 21 53 .8	–	15.87	14.80	14.27
4691–2	12 48 13 .55	–3 16 20 .8	–	16.46	15.29	14.64
4691–3	12 48 11 .73	–3 15 20 .8	–	–	16.26	15.74
4691–4	12 48 08 .90	–3 20 01 .9	–	–	16.67	15.85

For star 1084–6 $I = 15.51$.

standard techniques. The errors in the resulting magnitudes are from $0^m.05$ to $\sim 0^m.2$ for stars fainter than 15^m in the *B* filter.

The results for the comparison stars are collected in Table 1; the stars are identified by the NGC catalog numbers of the corresponding galaxies plus the star's number in the order of decreasing *V* brightness for the given galaxy. The coordinates are given for epoch J2000.

When reducing the observations of SN 1995al, 1996bk, and 1996bo, we also used the comparison star magnitudes from Riess *et al.* [5] and from Tanabe *et al.* [6]. For stars in common around NGC 3021, our results are in good agreement with those from [5, 6]: three stars from [5] give $\overline{\Delta B} = -0^m.02$, $\overline{\Delta V} = -0^m.09$, and four stars from [6] give $\overline{\Delta V} = -0^m.03$ (these are the average differences between our magnitudes and those published by the other authors).

2. RESULTS OF OBSERVATIONS OF THE SUPERNOVAE

The results of our observations are presented in Table 2.

(1) SN 1995al in NGC 3021 was discovered visually by Pesci and Mazza on November 1, 1995 [7]. The supernova's coordinates are $\alpha = 9^h50^m55^s.99$, $\delta = 33°33'09''.4$

Table 2. Observations of the supernovae

JD 2450000+	Telescope, equipment	*B*	*V*	*R*	JD 2450000+	Telescope, equipment	*B*	*V*	*R*
SN 1995al					SN 1996bo				
47.5	60-cm, phe	14.70	13.87	–	392.4	50-cm, pg	16.25	–	–
47.6	50-cm, pg	14.73	–	–	392.4	″	16.36	–	–
48.5	″	14.66	–	–	393.3	″	16.34	–	–
68.3	″	16.40	–	–	395.3	″	16.68	–	–
68.4	″	16.28	–	–	396.3	″	16.86	–	–
68.5	″	16.34	–	–	396.4	″	–	16.10	–
70.4	″	16.25	–	–	400.3	″	17.43	16.30	–
101.3	50-cm, TV	16.76	16.11	15.74	401.3	″	17.64	–	–
133.3	″	17.11	16.75	16.61	401.4	″	–	16.15	–
211.4	″	–	18.6	–	402.3	″	17.85	–	–
SN 1996an					402.4	″	–	16.45	–
307.5	50-cm, pg	16.65	–	–	403.4	″	17.79	16.42	–
309.5	″	16.62	–	–	404.4	″	17.90	–	–
309.7	60-cm, CCD	–	–	14.82	405.5	″	–	16.65	–
310.5	50-cm, pg	16.55	–	–	SN 1997X				
311.5	″	16.63	15.68	–	495.5	50-cm, TV	17.0	15.52	14.73
312.5	″	16.93	–	–	509.4	″	–	16.01	15.74
402.4	50-cm, TV	–	18.63	17.84	510.4	″	–	16.36	15.96
430.4	″	–	–	17.92	518.4	″	–	17.0	16.6
462.2	1-m, CCD	20.60	18.98	17.99			*U*	*I*	
463.2	″	20.53	19.13	18.16	SN 1995al				
SN 1996bk					47.5	60-cm, phe	14.90	–	–
392.5	50-cm, pg	17.32	–	–	SN 1996an				
393.5	″	17.45	–	–	463.2	1-m, CCD	–	17.39	–
395.5	″	17.52	–	–					
401.5	″	18.03	–	–					
402.6	″	18.05	–	–					
403.5	″	18.06	–	–					
404.6	″	–	16.54	–					

(2000), and it is 15″ west and 2.″9 south of the galaxy's center [8].

The results of spectroscopic observations of SN 1995al were published in [9–12]. They show SN 1995al to be a typical type Ia supernova. In terms of its line intensity and expansion velocity, determined from Doppler shifts of absorption lines, it is virtually indistinguishable from the well-studied "normal" type Ia supernova SN 1981B. CCD photometry of SN 1995al was obtained by Tanabe *et al.* [6] and Riess *et al.* [5].

Our observations of SN 1995al began on November 25, 1995. We obtained a photoelectric *UBV* brightness estimate with the 60-cm reflector of the SAI Crimean Laboratory. Two diaphragms, 14.″3 and 27.″5, were used, enabling us to subtract the galaxy's background with good accuracy. In November and December 1995, we observed SN 1995al photographically with the 50-cm telescope of the SAI Crimean Laboratory, and from January–May 1996, we carried out *BVR* video observations with the CrAO 50-cm telescope. We estimate the errors of our photoelectric estimates to be $\sim 0^m.1$, and of the photographic magnitudes to be $\sim 0^m.15$–$0^m.2$. In January–February 1996, the uncertainty of our video observations was about $0^m.2$; the last *V* brightness estimate, for May 1996, is based on images taken without a filter, and its error could be as high as $0^m.5$.

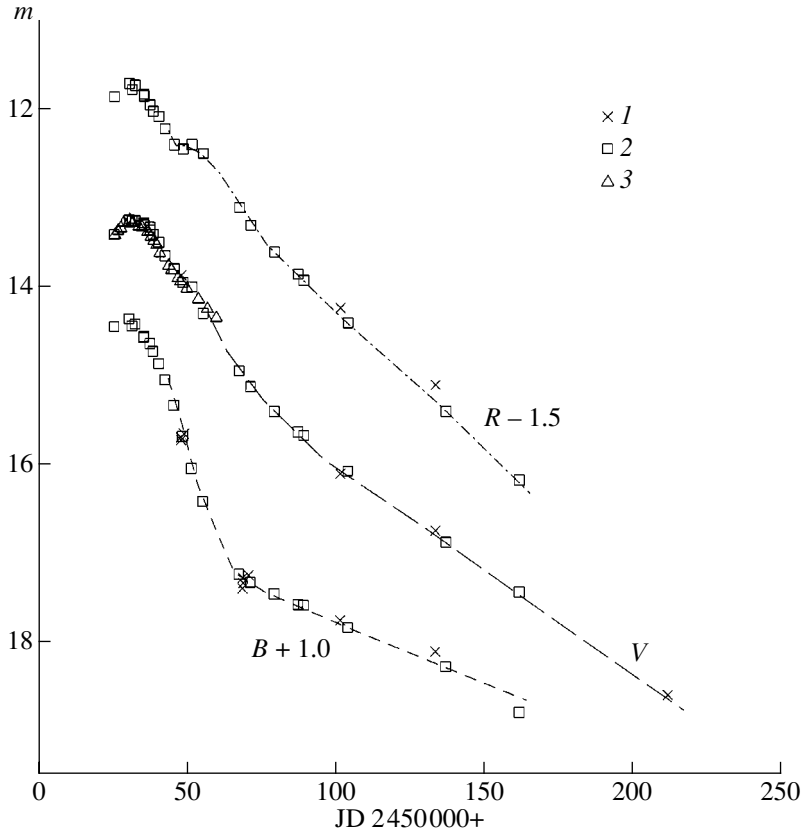

Fig. 2. *B*, *V*, and *R* light curves of SN 1995al constructed using (*1*) our data and (*2*, *3*) the data from [5, 6]. The *B* curve is displaced 1^m downwards and the *R* curve $1\overset{m}{.}5$ upwards.

Figure 2 shows the *BVR* light curves of SN 1995al. Results obtained by different authors are in good agreement. The shape of the light curves is characteristic of type Ia supernovae. SN 1995al was discovered prior to its brightness maximum, which was determined quite accurately: $B_{max} = 13\overset{m}{.}35$, $V_{max} = 13\overset{m}{.}25$, $R_{max} = 13\overset{m}{.}25$. The maximum *B* brightness occurred on JD 2450030; the maximum in *V* happened two days later, simultaneous with the *R* maximum. The inflection point [13] is at $B_K = 16\overset{m}{.}25$ on JD 2450064 and $V_K = 15\overset{m}{.}4$ on JD 2450076.

The rate of brightness decline after maximum was $\beta_B = 10.0$, $\beta_V = 5.2$; after the inflection, it was $\gamma_B = 1.4$, $\gamma_V = 2.4$ (in units of $\Delta m/100^d$ [14]). The value of Δm_{15} describing the rate of decline of the *B* brightness after maximum is about $1\overset{m}{.}0$ (in [15], it was estimated to be $0\overset{m}{.}94 \pm 0\overset{m}{.}05$). These parameters are close to the mean values for type Ia supernovae.

SN 1995al experienced virtually no absorption in our Galaxy [16]. There is some absorption in NGC 3021: a weak interstellar Na I D absorption line is apparent in the spectrogram from [8]. The *B*–*V* color curve demonstrates reddening by approximately $0\overset{m}{.}2 \pm 0\overset{m}{.}05$ compared to type I supernovae with no interstellar absorption. The absorption was estimated in [10, 15, 17], yielding the *E*(*B*–*V*) values $0\overset{m}{.}26$, $0\overset{m}{.}074$, $0\overset{m}{.}157$, and $0\overset{m}{.}246$. The average of these estimates is in good agreement with our result.

The distance to NGC 3021 in the Tully catalog [18], 25.1 Mpc, corresponds to the distance modulus $\mu = 32.0$, so that the absolute magnitudes of SN 1995al at maximum brightness are $M_B = -18\overset{m}{.}65$ and $M_V = -18\overset{m}{.}75$. Assuming $E(B–V) = 0\overset{m}{.}2$, we obtain $M_B^0 = -19\overset{m}{.}45$, close to the mean absolute magnitude for type Ia supernovae.

(2) SN 1996an in NGC 1084 was discovered by Aoki on July 27, 1996 during CCD observations. The discovery announcement [19] contains the supernova's brightness estimate (14^m), coordinates ($\alpha = 2^h46^m00\overset{s}{.}83$, $\delta = -7°34'20''.3$, J2000), and distance from the center of the galaxy (15″ east and 22″ north) [19]. Benetti *et al.* [20] observed SN 1996an spectroscopically on July 30. Lines of hydrogen, calcium, sodium, and other elements with typical P Cygni profiles were apparent in the spectrum; a narrow interstellar Na I D line was also detected. It was concluded that SN 1996an was a type II

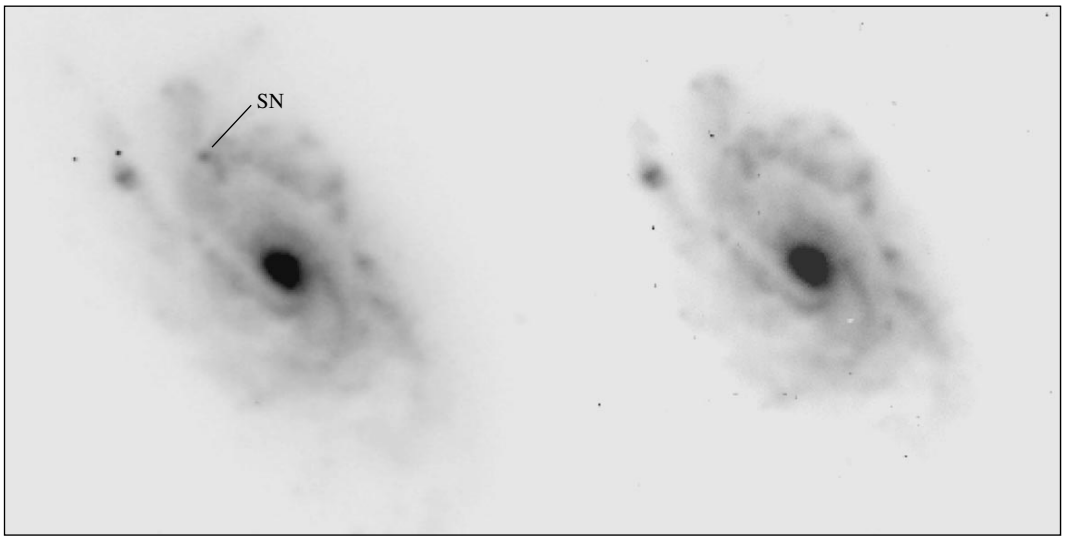

Fig. 3. Left: CCD image of NGC 1084 with the supernova SN 1996an taken with the SAO 1-m telescope on January 13, 1997. Right: CCD image of NGC 1084 retrieved from the ING archive.

supernova, discovered approximately two months after its outburst. Garnavich *et al.* [21] published the results of their *BVRI* CCD photometry of SN 1996an obtained on July 30. CCD photometry in the *V* band, as well as without a filter, was carried out at the Ouda Observatory in Japan (http://www.kusastro.kyoto-u.ac.jp/vsnet/etc/searchobs.cgi?text=SN1996an).

Our observations of SN 1996an began in August 1996. V.F. Esipov obtained images of the supernova in a system close to *R* using the 60-cm reflector of the SAI Crimean Laboratory with an ST-8 CCD camera. Photographic *B* and *V* observations with the 50-cm telescope were also carried out in August. Video observations in the *V* and *R* filters were conducted in November and December 1996. On January 13–14, 1997, *BVRI* CCD images of SN 1996an were obtained with the 1-m SAO telescope; the *R* image is displayed in Fig. 3, with a CCD image of NGC 1084 from the ING data archive (http://archive.ast.cam.ac.uk/ingarch/) shown for comparison. The supernova appeared in a spiral arm, at the edge of an H II zone. To eliminate the galaxy's background from the SAO images, we subtracted the ING archive image of NGC 1084. The brightness of the supernova was determined using aperture photometry, relative to the star 1084-6. The estimates are accurate to about $0\overset{m}{.}1$; the brightness estimate from CCD images taken in August 1996 has approximately the same uncertainty. The errors of the photographic photometry in August 1996 are about $0\overset{m}{.}1$–$0\overset{m}{.}15$, and those of the video observations about $0\overset{m}{.}2$–$0\overset{m}{.}3$.

Figure 4 shows the *BVR* observations of SN 1996an. The Ouda Observatory observations appear to have a considerable systematic error, while our data agree well with the results from [21]. We conclude that the supernova's brightness remained virtually constant during JD 2450294–342 (July 30–September 16, 1996). SN 1996an is apparently a type II P supernova, with an extended "plateau" in its light curve. According to [20], the outburst took place two months before the discovery, so that the total duration of the plateau should have been about 100 days, and the light curve of SN 1996an was probably similar to those of such type II P supernovae as SN 1969L, 1986I, and 1988A [22]. Observations of SN 1996an are compared to the *V*-band light curve of SN 1988A in Fig. 4; the agreement is quite good. The plateau *V* brightness of SN 1996an was $15\overset{m}{.}6$, and its *B*–*V* color index was about $1\overset{m}{.}0$. According to the Tully catalog [18], the distance to NGC 1084 is 17.1 Mpc, so that the distance modulus is $\mu = 31.2$, and the plateau absolute magnitude of SN 1996an is $M_V = -15\overset{m}{.}6$. There is virtually no absorption in the Galaxy [16]; there is no doubt that there is absorption in NGC 1084, since the interstellar Na I D line was detected [20]. Comparing the plateau *B*–*V* color index for SN 1996an with the analogous data for SN 1969L and 1988A, we derive the color excess $E(B–V) \sim 0\overset{m}{.}2$. In this case, the plateau absolute magnitude of SN 1996an is $M_V^0 \approx -16\overset{m}{.}2$, nearly coincident with the corresponding values for SN 1969L and 1988A. Thus, our data clearly indicate that SN 1996an is a type II P supernova, typical in all its parameters and similar to the well-studied objects SN 1969L, 1986I, and 1988A.

The bright Ia supernova SN 1963P was also observed in NGC 1084. Photographic *B*-band photometry was obtained by Bertola *et al.* [23]. It was shown in [24, 25] that Asiago Observatory photographic observations in the 1960s and 1970s often possessed considerable systematic errors, which are revealed when comparison star magnitudes are remeasured. We

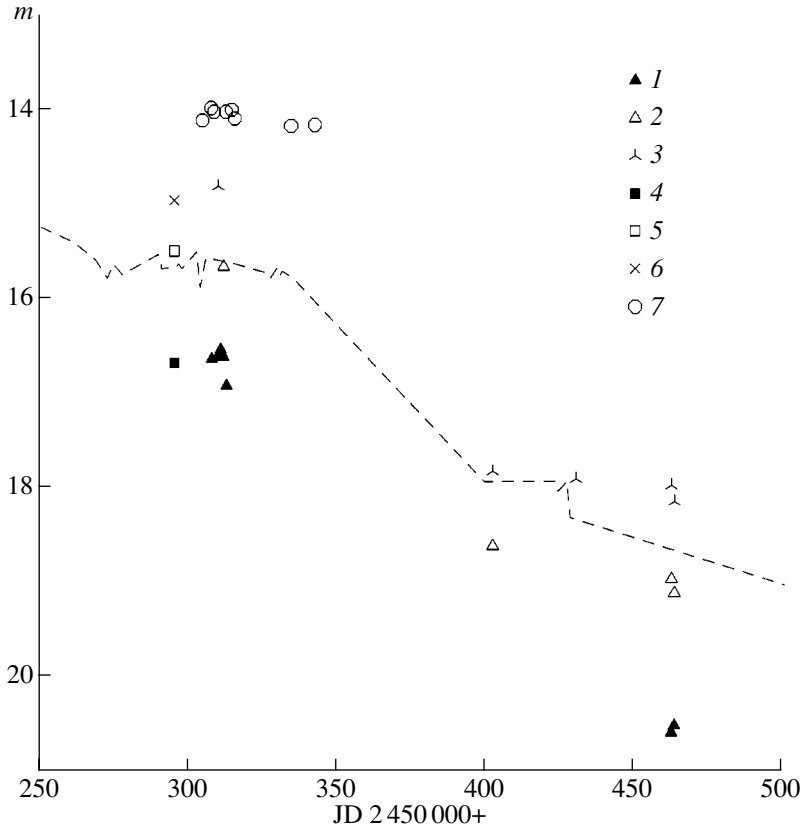

Fig. 4. *B*, *V*, and *R* light curves of SN 1996an constructed using our brightness estimates in the *B*, *V*, and *R* filters (*1*, *2*, *3*), the data of [21] for the same filters (*4*, *5*, *6*), and the Ouda Observatory *V*-band data (*7*). The dashed curve is the *V* light curve of SN 1988A.

measured the *B* magnitudes for nine comparison stars from [23] and found errors up to $0\overset{m}{.}5$, strongly dependent upon the magnitude. This dependence is represented fairly well by the second-order polynomial $\Delta B = -12.44 + 1.78B - 0.0615B^2$. Having corrected the observations of SN 1963P, we obtained the following parameters for its *B*-band light curve: $B_{\max} = 14\overset{m}{.}4$, $t_{B\max}$ = JD 2438303, $B_K = 17\overset{m}{.}2$, t_{Bk} = JD 2438331, $\beta_B = 11.5$, $\Delta m_{15} = 1.35$, in marked variance from those presented, for example, in [14]. The absolute magnitude of SN 1963P at maximum brightness for the adopted distance to NGC 1084 is $M_B = -16\overset{m}{.}8$, more than by 2^m fainter than the mean magnitude for type Ia supernovae. This could be explained by interstellar absorption in NGC 1084, but no data on the color index of SN 1963P or other characteristics making it possible to estimate the absorption are available.

(3) SN 1996bk in NGC 5308 was discovered visually by Mazza and Pesci [26] on October 12, 1996. The supernova's coordinates, $\alpha = 13^h46^m57\overset{s}{.}98$ and $\delta = 60°58'12\overset{''}{.}9$, and the CCD brightness estimate for October 13, 1996, $V = 14\overset{m}{.}05$, were published in [27]. Garnavich *et al.* [28] determined the supernova to be $10\overset{''}{.}5$ south and $17\overset{''}{.}9$ west of the galaxy's center. On October 15, they obtained a spectrum of SN 1996bk showing it to be a type Ia supernova one week after its maximum brightness. Riess *et al.* [5] carried out *BVRI* CCD photometry. Their visual brightness estimates of the supernova are collected in the VSNET data archive (http://www.kusastro.kyoto-u.ac.jp/vsnet/SNe/sn1996bk.html).

Our photographic observations of SN 1996bk were obtained on November 4–16, 1996 with the 50-cm telescope of the SAI Crimean Laboratory. We took six plates in *B* and one in *V*. The accuracy of our brightness estimates is no better than $0\overset{m}{.}2$ to $0\overset{m}{.}3$. The light curves are shown in Fig. 5. The good agreement between our data and those of Riess *et al.* [5] is evident.

This supernova was discovered after its brightness maximum. It is possible to determine the position of the inflection point ($B_K = 17\overset{m}{.}9$, t_{Bk} = JD 2450399, $V_K = 16\overset{m}{.}85$, t_{Vk} = JD 2450405) and the decline rate ($\beta_B = 10.6$, $\beta_V = 7.7$, $\gamma_B = 2.0$, $\gamma_V = 2.6$) directly from the observational data. According to Tully [18], the distance to NGC 5308 is 32.4 Mpc, so that the distance modulus is $\mu = 32.55$. Thus, the absolute magnitude of

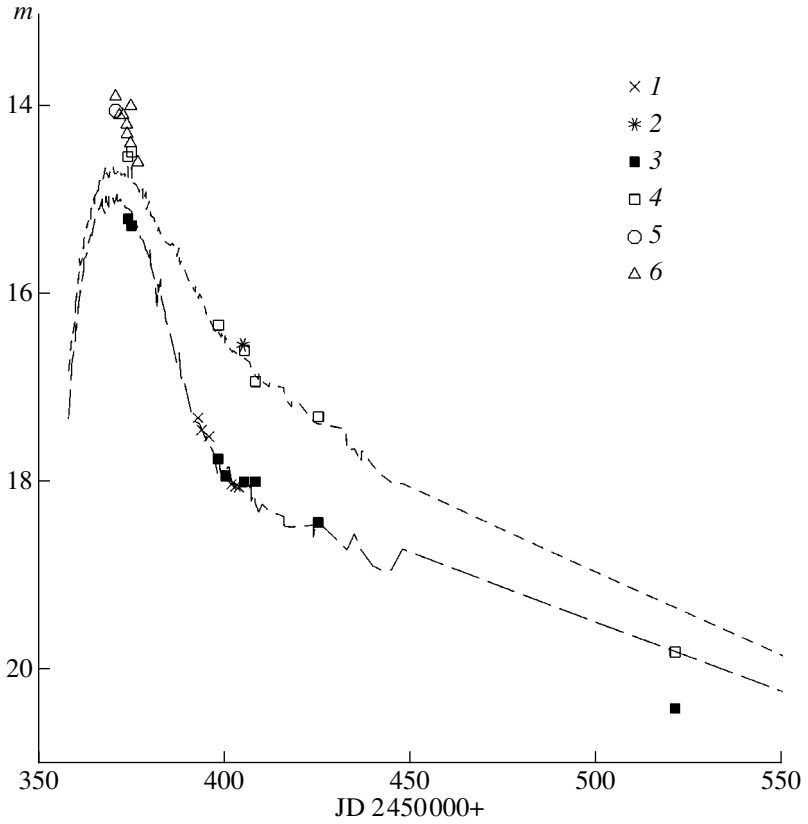

Fig. 5. *B* and *V* light curves of SN 1996bk constructed using our results for the *B* and *V* bands (*1*, *2*), the *B* and *V* estimates from [5] (*3*, *4*), the CCD *V* magnitude from [27] (*5*), and visual observations from the VSNET data archive (*6*). The dashed curves are the *B* and *V* light curves of SN 1994D.

SN 1996bk at the inflection point is $M_{Bk} = -14\overset{m}{.}65$, 2^m fainter than the mean magnitude of type Ia supernovae [13].

The supernova experiences no absorption in our Galaxy [16]. The *B*–*V* color curve for SN 1996k shows substantial reddening, estimated to be $E(B–V) = 0\overset{m}{.}4 \pm 0\overset{m}{.}15$. In this case, the *B*-band absorption in NGC 5308 is about $1\overset{m}{.}6$, and the inflection-point absolute magnitude of SN 1996bk is $M^0_{Bk} = -16\overset{m}{.}25$, fairly close to the mean value for type Ia supernovae. In our opinion, the reddening estimate of [17], $E(B–V) = 0\overset{m}{.}274$, is too low.

Figure 5 compares the light curves of SN 1996bk and SN 1994D. SN 1996D is one of the most comprehensively studied type Ia supernovae with a post-maximum decline rate [29] similar to that for SN 1996bk. We shifted the light curves relative to one another by aligning the inflection points. The agreement is rather good for the *B*-band curve, though the decline rate after the inflection was probably higher for SN 1996bk than for SN 1994D. However, the *V*-band light curves are substantially different. For SN 1996bk, the brightness drop from maximum to the inflection point was at least $2\overset{m}{.}8$, considerably exceeding the corresponding value for SN 1994D and other well-studied type Ia supernovae. Unfortunately the behavior of the *V* light curve immediately after maximum is based on visual observations and a single CCD estimate from [26], which could have significant systematic errors. For this reason, we are not able to make firm conclusions about whether the light curve of SN 1996bk is peculiar.

Assuming the *B* light curve does not differ from those typical of type Ia supernovae, we can estimate the position of maximum brightness by shifting the light curve of SN 1994D to fit the observations of SN 1996bk: $B_{\max} = 15\overset{m}{.}0$, $t_{B\max}$ = JD 2450370. For the adopted brightness, distance, and absorption, the absolute magnitude of SN 1996bk at maximum was $M^0_B = -19\overset{m}{.}15$, fairly close to the mean for type Ia supernovae.

(4) SN 1996bo in NGC 673 was discovered on October 18, 1996 during CCD observations performed as part of the supernova search program of the Beijing Observatory [30]. The supernova was independently found by Armstrong [31] and Okazaki [32] on October 23 and 24. Its coordinates are $\alpha = 1^h48^m22\overset{s}{.}862$, $\delta = 11°31'15\overset{''}{.}13$, placing it $6\overset{''}{.}14$ east and $1\overset{''}{.}58$ south of the galaxy's center [33]. A spectrum taken on October 24 by Turatto *et al.*

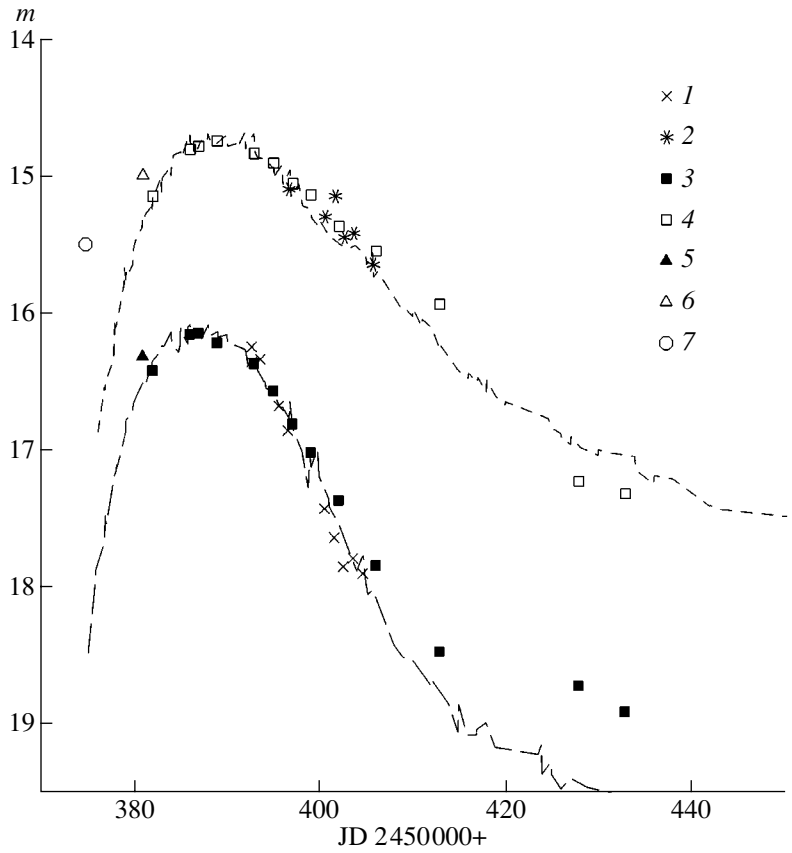

Fig. 6. *B* and *V* light curves of SN 1996bo constructed using our data (*1*, *2*) together with the *B* and *V* data from [5] (*3*, *4*), [34] (*5*, *6*), and the *V* estimate from [36] (*7*). The dashed curves are the *B* and *V* light curves of SN 1994D.

[34] shows SN 1996bo to be a type Ia supernova, similar to SN 1981B and SN 1992A, at a phase approximately one week prior to its brightness maximum. The spectrum reveals strong interstellar Na I D lines, providing evidence for substantial absorption. Brightness estimates in *BVR* filters are also presented in [34]. Riess *et al.* [5] carried out *BVRI* CCD photometry of SN 1996bo.

Our photographic observations of this supernova were obtained with the 50-cm telescope on November 4 to 17, 1996; we took ten plates in the *B* band and six in the *V* band. The uncertainties of our brightness estimates are from $0\overset{m}{.}1$ to $0\overset{m}{.}25$.

Figure 6 presents the light curves of SN 1996bo. It is obvious that the supernova was discovered before its brightness maximum, which can be reliably determined from the observations: $B_{\max} = 16\overset{m}{.}15$, $t_{B\max}$ = JD 2450387, $V_{\max} = 15\overset{m}{.}75$, $t_{V\max}$ = JD 2450389. The post-maximum rate of brightness decline is above average for type Ia supernovae: $\beta_B = 12.0$, $\beta_V = 6.5$, $\Delta m_{15} = 1.3$. The inflection point was at $B_K = 18\overset{m}{.}4$, t_{Bk} = JD 2450410.

The *B* brightness drop from maximum to inflection was only $2\overset{m}{.}25$, much less than is usual for type Ia supernovae. We compare the light curves of SN 1996bo and SN 1994D in Fig. 6. The brightness-decline rates after maximum are approximately the same for the two supernovae [29]. The *B* light curves near maximum are the same, but they deviate by more than $0\overset{m}{.}5$ after the inflection point. However, the *V* light curves do not show such a deviation. Only the supernova discovery brightness estimate from [30] appears much brighter than could be expected from the superposition of the light curves for SN 1996bo and SN 1994D.

As expected, the *B*–*V* color curve for SN 1996bo testifies to the presence of substantial reddening; our estimate is $E(B–V) = 0\overset{m}{.}45 \pm 0\overset{m}{.}1$. The Galactic absorption for this supernova is $A_{B\text{gal}} = 0\overset{m}{.}15$ [16], corresponding to $E(B–V)_{\text{gal}} \approx 0\overset{m}{.}04$, so that almost all the absorption occurs in NGC 673. This galaxy's radial velocity, 5296 km/s, corresponds for $H_0 = 75$ km s^{-1} Mpc^{-1} to the distance modulus $\mu = 34.25$, so that the absolute magnitude at the maximum was $M_B^0 = -19\overset{m}{.}9$, brighter than average for type Ia supernovae. The estimates of $E(B–V)$

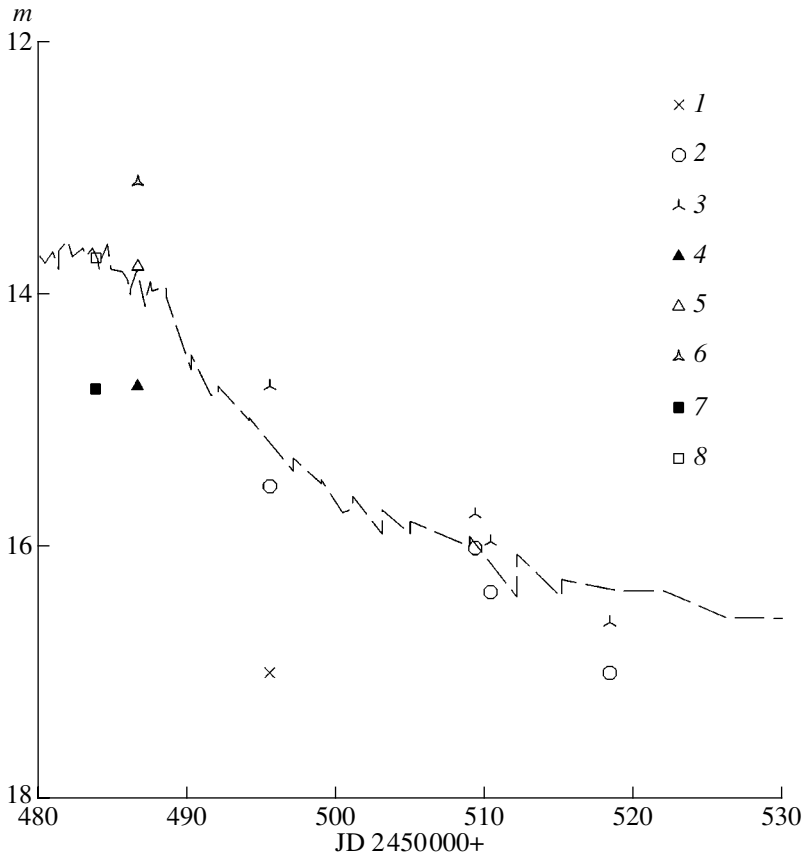

Fig. 7. Light curve of SN 1997X constructed using our *B, V, R* estimates (*1, 2, 3*), the data of [41] for the same filters (*4, 5, 6*), and the *B* and *V* estimates from [40] (*7, 8*). The dashed curve is the *V* light curve of SN 1994I.

from [17], $0\overset{m}{.}358$ and $0\overset{m}{.}385$, essentially coincide with our value, taking into account the value $E(B–V)_{\rm gal} = 0\overset{m}{.}08$ assumed in [17].

(5) SN 1997X in NGC 4691 was discovered by Aoki [35] on February 1, 1997. The supernova's coordinates are $\alpha = 12^{\rm h}48^{\rm m}14\overset{\rm s}{.}28$, $\delta = -3°19'58\overset{''}{.}5$, $7\overset{''}{.}2$ east and $0\overset{''}{.}3$ north of the galaxy's center [36]. The first spectroscopic observations [37–39] and *BVI* CCD photometry [40] of this supernova were obtained on February 4. The spectra showed that SN 1997X probably belonged to type Ic, and that about a week had elapsed since its maximum. Ca II and Fe II lines dominated in the spectrum; He I lines may also have been present. The spectrum resembled the spectra of the type Ic supernovae SN 1987M and 1994I. Munari *et al.* [41] obtained spectroscopic observations on February 7, 8, and 18, which confirm the presence of He I lines in the spectrum. From the intensity of the interstellar Na I D absorption lines, they estimate the color excess to be $E(B–V) = 0\overset{m}{.}18 \pm 0\overset{m}{.}02$. The spectrophotometric data were used to determine the supernova's brightness in the *UBVRI* bands.

Our observations of SN 1997X were obtained on February 15–March 10, 1997, using the video equipment of the CrAO 50-cm telescope both with *BVR* filters and without a filter. Due to the intense background of the galaxy, only the first *R* brightness estimate is accurate to about $0\overset{m}{.}1$; the uncertainties of most of our estimates are $0\overset{m}{.}2–0\overset{m}{.}3$, and the accuracy of the data for March 10 and of the *B* magnitude for February 15 is no better than $0\overset{m}{.}5$.

Figure 7 presents the results of the observations. The spectroscopic data and the lack of significant brightness variations on February 4–7 show that the most probable date of the brightness maximum is from February 2 to 6 (JD 2450483-86). Comparison of the observations with the light curve of the type Ic supernova SN 1994I [29] shows a good agreement. The brightness of SN 1997X at maximum was probably $B_{\rm max} = 14\overset{m}{.}7$, $V_{\rm max} = 13\overset{m}{.}7$. In this case, using the absorption estimate from [40] and the distance modulus $\mu = 31.76$ from [18], we obtain the absolute magnitude at maximum $M_B^0 = -17\overset{m}{.}8$, $M_V^0 = -18\overset{m}{.}6$. The *B*-band absolute maximum nearly coincides with the corre-

sponding value for SN 1994I [29], but SN 1997X was brighter in V by more than $0\overset{m}{.}5$.

3. CONCLUSIONS

Our study of the light curves of the three supernovae whose spectroscopic data identify them as typical type Ia objects shows that only one (SN 1995al) has all of its photometric characteristics close to the mean values for type Ia supernovae. Peculiarities can be noted in the light curves of SN 1996bk and SN 1996bo; though they could not be confirmed with complete certainty, they nevertheless remain probable. Of special interest is SN 1996bo, which had a high decline rate after maximum, and is distinguished by an enhanced luminosity and reduced B decline rate from the maximum to the inflection point. This combination of parameters disagrees with the relations established for the majority of type Ia supernovae (see, for instance, [14, 15]).

The light curve of the type Ib/c supernova SN 1997X had a similar shape to that of SN 1994I, a well-studied supernova of the same type. However, SN 1997X was substantially "redder" at maximum and had a much brighter V-band absolute magnitude than SN 1994I. Thus, we confirm the existence of considerable variations in the photometric features of type Ib/c supernovae.

The type II supernova SN 1996an was probably a IIP supernova typical in all its photometric properties; its position in the galaxy NGC 1084, at the edge of an H II region, suggests that the supernova progenitor was a young, massive star.

ACKNOWLEDGMENTS

This study is based in part on data from the ING archive. It was partially supported by the Ministry of Science and Technology (project MNTTs 370), INTAS (grant 95-0832) and the Russian Foundation for Basic Research.

REFERENCES

1. A. N. Abramenko, V. V. Prokof'eva, N. I. Bondar', *et al.*, Izv. Krym. Astrofiz. Obs. **78**, 182 (1988).
2. J.-C. Mermilliod, *The General Catalogue of Photometric Data*, http://obswww.unige.ch/gcpd.
3. A. U. Landolt, Astron. J. **104**, 340 (1992).
4. C. Chevalier and S. A. Ilovaisky, Astron. Astrophys., Suppl. Ser. **90**, 225 (1991).
5. A. G. Riess, R. P. Kirshner, B. P. Schmidt, *et al.*, Astron. J. **117**, 707 (1999).
6. K. Tanabe, S. Honda, K. Matsumoto, *et al.*, http:// www.kusastro.kyoto-u.ac.jp/vsnet/Mail/vsnet/msg00386.html.
7. S. Pesci and P. Mazza, IAU Circ. No. 6255 (1995).
8. C. Pollas, IAU Circ. No. 6255 (1995).
9. J.-Y. Wey, W.-D. Li, Y.-L. Qiu, *et al.*, IAU Circ. No. 6256 (1995).
10. K. Ayani and H. Kawakita, IAU Circ. No. 6256 (1995); http://www.kusastro.kyoto-u.ac.jp/vsnet/Mail/vsnet-alert/msg00266.html.
11. C. C. Anupama, Astron. J. **114**, 2054 (1997).
12. F. J. C. Bowers, W. P. S. Meikle, T. R. Geballe, *et al.*, Mon. Not. R. Astron. Soc. **290**, 663 (1997).
13. N. N. Pavlyuk, D. Yu. Tsvetkov, Yu. P. Pskovskiĭ, and O. S. Bartunov, Pis'ma Astron. Zh. **24**, 951 (1998) [Astron. Lett. **24**, 826 (1998)].
14. Yu. P. Pskovskiĭ, Astron. Zh. **61**, 1125 (1984) [Sov. Astron. **28**, 658 (1984)].
15. B. R. Parodi, A. Saha, A. Sandage, and G. A. Tammann, astro-ph/0004063.
16. D. Burstein and C. Heiles, Astron. J. **87**, 1165 (1982).
17. M. M. Phillips, P. Lira, N. B. Suntzeff, *et al.*, Astron. J. **118**, 1766 (1999).
18. R. B. Tully, *Nearby Galaxies Catalog* (Cambridge Univ. Press, Cambridge, 1988).
19. S. Nakano and M. Aoki, IAU Circ. No. 6442 (1996).
20. S. Benetti, M. Turatto, and G. van de Steene, IAU Circ. No. 6442 (1996).
21. P. Garnavich, A. Riess, and R. Kirshner, IAU Circ. No. 6444 (1996).
22. F. Patat, R. Barbon, E. Cappellaro, and M. Turatto, Astron. Astrophys., Suppl. Ser. **98**, 443 (1993).
23. F. Bertola, A. Mammano, and M. Perinotto, Asiago Contributions, No. 174 (1965).
24. D. Yu. Tsvetkov, Perem. Zvezdy **22**, 279 (1986).
25. F. Patat, R. Barbon, E. Cappellaro, and M. Turatto, Astron. Astrophys. **317**, 423 (1997).
26. P. Mazza and S. Pesci, IAU Circ. No. 6491 (1996).
27. J. Mackey, IAU Circ. No. 6491 (1996).
28. P. Garnavich, R. Kirshner, J. Huchra, and L. Macri, IAU Circ. No. 6491 (1996).
29. D. Yu. Tsvetkov and N. N. Pavlyuk, Pis'ma Astron. Zh. **21**, 678 (1995) [Astron. Lett. **21**, 606 (1995)].
30. W. Li, Q. Qiao, Y. Qui, and J. Hu, IAU Circ. No. 6497 (1996).
31. M. Armstrong, IAU Circ. No. 6497 (1996).
32. K. Okazaki, IAU Circ. No. 6498 (1996).
33. I. Sato, H. Fukushima, and N. Yamamoto, IAU Circ. No. 6499 (1996).
34. M. Turatto, S. Benetti, and M. Lemke, IAU Circ. No. 6497 (1996).
35. S. Nakano and M. Aoki, IAU Circ. No. 6552 (1997).
36. Y. Kushida and R. Kushida, IAU Circ. No. 6552 (1997).
37. N. B. Suntzeff, A. Clocchiatti, M. M. Phillips, and D.-W. Kim, IAU Circ. No. 6552 (1997).
38. P. Garnavich, R. Kirshner, and P. Berlind, IAU Circ. No. 6552 (1997).
39. S. Benetti, M. Turatto, I. Perez, and L. Wisotzki, IAU Circ. No. 6554 (1997).
40. R. Covarrubias, IAU Circ. No. 6552 (1997).
41. U. Munari, R. Barbon, A. Piemonte, *et al.*, Astron. Astrophys. **333**, 159 (1998).

Translated by N. Samus'

Astronomy Reports, Vol. 45, No. 7, 2001, pp. 538–552. Translated from Astronomicheskiĭ Zhurnal, Vol. 78, No. 7, 2001, pp. 625–641.

Interpretation of Light Curves of IP Peg in a Model with Shockless Interaction between the Gas Stream and Disk

T. S. Khruzina[1], A. M. Cherepashchuk[1], D. V. Bisikalo[2], A. A. Boyarchuk[2], and O. A. Kuznetsov[3]

[1]*Sternberg Astronomical Institute, Universitetskiĭ pr. 13, Moscow, 119899 Russia*

[2]*Institute of Astronomy, Russian Academy of Sciences, ul. Pyatnitskaya 48, Moscow, 109017 Russia*

[3]*Keldysh Institute of Applied Mathematics, Russian Academy of Sciences, Miusskaya pl. 4, Moscow, 125047 Russia*

Received December 8, 2000

Abstract—We have analyzed light curves of the eclipsing cataclysmic variable IP Peg. A model with a shockless interaction between the gaseous stream and disk (i.e., an elliptical disk with a "hot line") can describe the main characteristic features of the light curve of the interacting close binary better than a classical model with a "hot spot" at the outer boundary of a circular accretion disk. In particular, the hot-line model can reproduce the luminosity increase observed at phases $\varphi \sim 0.1$–0.2 and $\varphi \sim 0.5$–0.6, which is not possible in the standard hot-spot model. The advantages of the hot-line model are particularly striking for the IR light curves of IP Peg: the discrepancy χ^2 between the theoretical and observed light curves is 49 for the model with a shockless interaction between the gaseous stream and disk, and 2681 for the standard hot-spot model. © *2001 MAIK "Nauka/Interperiodica".*

1. INTRODUCTION

A three-dimensional gas-dynamical model of the gas flows in interacting close binary systems (CBSs) was considered in [1–3]. These calculations showed that, in the steady-state case, a gaseous stream flowing from the inner Lagrange point (L_1) and the accretion disk form a structure with a single morphology, since the point of tangency between the stream and disk is free of discontinuities and shocks, so that a classical "hot spot" cannot be formed [4, 5]. At the same time, the interaction between the gaseous stream and the intercomponent envelope of the CBS forms an extended shock wave along the edge of the stream: a "hot line" [1–3, 6]. This shock can explain the characteristic features of the light curves of cataclysmic variables [7], in particular, the occurrence of both regular and anomalous humps accompanying eclipses of the accretion disk by the donor star.

Here, we present the results of applying new procedures for light-curve synthesis [8] developed on the basis of three-dimensional gas-dynamical calculations [1–3, 7]. Unlike [7], we consider a more realistic model with an elliptical accretion disk with an extended bright region (hot line) along the stream emerging from L_1. Using IP Peg, a cataclysmic variable with a double eclipse, as an example, we have derived model parameters from the mean light curve. Models with an elliptical disk and hot line can fit the main features of the light curves of the interacting CBS better than classical models with a hot spot at the outer boundary of a circular accretion disk.

2. PHYSICAL JUSTIFICATION OF THE MODEL

Mass transfer between the components in a semi-detached binary is traditionally described according to the following scheme: (a) gas flows from the donor star through the inner Lagrange point L_1 and forms a stream; (b) stream material with excess angular momentum is unable to be accreted directly and forms a gaseous ring around the accretor; (c) this gaseous ring spreads out under the action of dissipative processes in the accretion disk, and some fraction of this material falls onto the surface of the accretor.

In the late 1960s, Gorbatskiĭ [4] and Smak [5] suggested that the interaction between the stream and accretion disk is accompanied by the formation of a shock wave, and a hot spot forms at the point of contact between the stream and disk. Over the last thirty years, this model has been widely applied in studies of cataclysmic binaries (see, for example, [9]), and has been used to explain the presence of humps in light curves, although many observational properties of these systems have remained beyond its scope.

In recent years, gas-dynamical models for the mass transfer in semi-detached CBSs have been radically revised [1–3, 7]. Three-dimensional gas-dynamical calculations [1–3, 6] have shown that, in a steady-state flow regime, the gaseous stream and accretion disk undergo a shockless interaction, and do not form a classical hot spot. These calculations indicate that the stream–disk system has a single morphology, and that the transition from the stream to the disk is free of dis-

1063-7729/01/4507-0538$21.00 © 2001 MAIK "Nauka/Interperiodica"

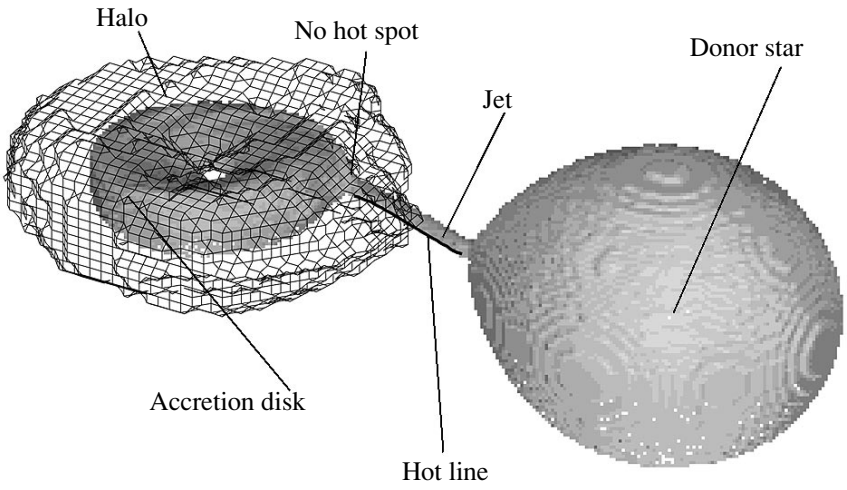

Fig. 1. The structure of mass transfer in a CBS. The white spot in the center of the disk indicates the location of the accretor.

continuities and shocks. In addition, the flow pattern in CBSs is substantially more complicated than implied by the above simple scheme. In addition to the stream and accretion disk, a gaseous "halo" forms around the accretion disk and intercomponent envelope of the system. The gas of the intercomponent envelope flows around the accretor and collides with the stream from L_1, forming a shock front along the edge of the stream (the hot line). Figure 1 presents a schematic of the basic elements of the calculated flow structure for the cataclysmic binary IP Peg: the density iso-surface at the $\rho = 10^{-3}\rho(L_1)$ level and the contours of the halo corresponding to $\rho = 10^{-4}\rho(L_1)$.

Models for mass transfer in CBSs with a hot line instead of a hot spot are fairly universal. Variations of the viscosity, radiative energy-loss rate, and other conditions of the gas flows in CBSs [10–12] do not qualitatively affect the basic conclusion of the three-dimensional gas-dynamical calculations: in a steady-state mass-transfer regime, classical models with a hot spot, usually considered to be the region where the gaseous stream collides by the outer boundary of the disk, must be replaced by models with a hot line formed outside the disk, along the gaseous stream, due to the interaction of the stream with the intercomponent envelope. It was shown in [7] that the hot line can adequately explain the presence of humps in CBS light curves.

To study the structure of the disk and circum-disk formations during outbursts, we should observe systems with highly inclined orbital planes, in which the eclipse of the accretion disk by the secondary star can be seen. We have chosen the CBS IP Peg, which has a so-called double eclipse; i.e., at the moment of lower conjunction of the donor star, this star consecutively eclipses not only the white dwarf, but also the asymmetrical accretion structure surrounding it. The classical model can describe the double-eclipse profile reasonably well; however, it cannot reproduce some parts of the curves outside of eclipse, especially at epochs of outburst, when an anomalous hump appears in the light curve.

3. MATHEMATICAL MODEL OF THE SYSTEM

The hot-line model is in better agreement with the observations than the hot-spot model [7], but also needs refinement. Comparison of synthetic and observed light curves will enable the determination of a number of parameters, which can then be used to improve gas-dynamical models for mass transfer in semi-detached binaries. A detailed gas-dynamical model and correct mathematical representation via a photometric model will open fresh opportunities for analysis of the rich observational data available for interacting CBSs. It will also make it possible to determine more accurately the physical characteristics and evolutionary statuses of different types of interacting CBSs. This is particularly important in the context of prospects for the launch of UV satellite observatories (for example, SPECTR-UV), which will provide opportunities for detailed observations of interactions between gaseous structures in CBSs. Here, we use a simplified blackbody hot-line model.

The mathematical model used to synthesize the theoretical light curves and estimate the parameters of the interacting CBS [8] is based on the three-dimensional structure of the gaseous flows in these systems suggested by the results of [1–3, 10–12]. The basic assumptions of the photometric model can be formulated as follows.

(1) The donor star (secondary) fills its Roche lobe entirely; i.e. we take into account both its tidal and rotational deformation.

(2) The surface of the donor star is divided into 648 area elements. For each, the radiation intensity directed toward the observer is calculated taking into

account gravitational darkening, limb darkening, and the effect of heating by radiation from the white dwarf. For each phase, we consider only areas facing the observer, taking into account their eclipse by all components of the system, including the donor star.

(3) The white dwarf (primary) is spherical and located at one focus of the elliptical accretion disk. The surface of the white dwarf is also divided into 648 area elements. The effective temperature of these areas is assumed to be the same over the entire surface of the star. We take into account limb darkening when calculating the radiation intensity directed toward the observer. Areas on the white dwarf can be eclipsed by the body of the star itself, the accretion disk, the donor star, and the hot line.

(4) The figure of the elliptical accretion disk is determined as follows [8]: (a) the lateral (outer) surface of the disk is specified by an ellipsoid with semi-axes a, b and c, with a and b in the orbital plane and $b^2 = a^2(1 - e^2)$, and with c perpendicular to the orbital plane; (b) the center of the white dwarf is located at one focus of the ellipsoid; (c) the inner surfaces of the disk result from subtracting from the ellipsoid those sections of the ellipsoid that fall on the inner regions of two paraboloids, specified by the parameter A_p.

The axes of the paraboloids determining the inner disk surface are perpendicular to the orbital plane. The parameter A_p depends on the angle of rotation ψ of the radius vector from the vertex of the paraboloid to the edge of the disk about the paraboloid axis. At the disk periastron, $\psi = 0$, and $\psi = \pi$ at apoastron. The coefficient $A_p(\psi)$ is

$$A_p(\psi) = \frac{Ab^2}{a^2(1 + e\cos\psi)} = \frac{A(1 - e^2)}{1 + e\cos\psi}, \qquad (1)$$

where A is constant. For $e = 0$, this coincides with the paraboloid constant $A_{\rm par}$ [13] describing the shape of the inner surfaces of a circular disk, $A_p(\psi) = A = \text{const}$. In the case of an elliptical disk, we obtain $A_p(\psi) = A(1 - e)$ at periastron ($\psi = 0$), and $A_p(\psi) = A(1 + e)$ at apoastron ($\psi = \pi$). The vertices of the paraboloids are shifted relative to the orbital plane of the CBS by $z_0 = \dfrac{R_w^2}{A^2(1 - e)^2}$: these are below and above the orbital plane for the upper and lower paraboloids, respectively. For this choice of z_0 with $\psi = 0.0$ (at disk periastron), the paraboloids will intersect the orbital plane at a distance R_w from the white dwarf's center, where R_w is the radius of the white dwarf. We assumed that the inner (for example, upper) surface of the disk is formed by that part of the paraboloid with non-negative z coordinates. The lines of intersection of the ellipsoid describing the lateral part of the disk and the paraboloids describing its inner parts specify the upper and lower disk boundaries. These are located a distance h from the orbital plane:

$$h = \pm c\left(\sqrt{\frac{c^2A^4}{4b^4} - \frac{1}{b^2}\left[\frac{R_w^2}{(1 - e)^2} - a^2\right]} - \frac{cA^2}{2b^2}\right). \qquad (2)$$

The orientation of the disk is specified by the angle α_e between the radius vector from the white dwarf's center to the disk periastron and the line connecting the CBS components. α_e can vary from 0 to 2π, and increases in the direction of the orbital motion of the components. A detailed description of modeling of a geometrically thick elliptical accretion disk is presented in [13].

When calculating the temperature of an area element on the disk surface, we took into account the dependence on the distance r between the center of the element and the white-dwarf surface. The temperatures of areas on the disk near the white-dwarf surface were taken to be equal to the temperature T_{bw} of the surface layer located near the equator of the star, with $T_{bw} \geq T_w$. In [8, 13], the temperatures of areas on the disk were specified by the temperature of the white dwarf T_w. However, observations indicate that, in many cataclysmic variables, the temperature of the inner part of the disk substantially exceeds T_w. In addition, the observed radiation flux from the white dwarf is relatively small, and is not able to provide the observed heating of the secondary. The heating of the disk is associated with the transformation of the gravitational energy of matter into heat in the course of its motion toward the surface of the white dwarf. It is generally assumed that the disk surface temperature T_g varies with distance from the center of the white dwarf r according to the law

$$T_g = T_{bw}\left(\frac{R_w}{r}\right)^{\beta_g}. \qquad (3)$$

To first approximation, the parameter β_g is usually taken to be $\beta_g = 3/4$ [14], assuming that each point of the disk surface radiates as a blackbody. In reality, however, the radial temperature distribution turns out to be flatter than a 3/4 law, especially during outbursts. Apart from the above relation, the temperature of a disk area element can increase by several percent due to heating by radiation from the white dwarf and secondary.

(5) The hot line along the stream is described by a section of an ellipsoid with semi-axes a_v, b_v and c_v extended toward the inner Lagrange point L_1 (Fig. 2). The lateral surface of this ellipsoid coincides with the tangent line to the elliptical disk independent of its orientation, while its center is located in the orbital plane inside the disk at some distance from its edge. Figure 2 presents a schematic of the basic CBS elements used in the photometric model for an orbital inclination $i = 0°$ (the view from above). The arrows in the graphs indicate the direction of gas motion in the disk. A detailed

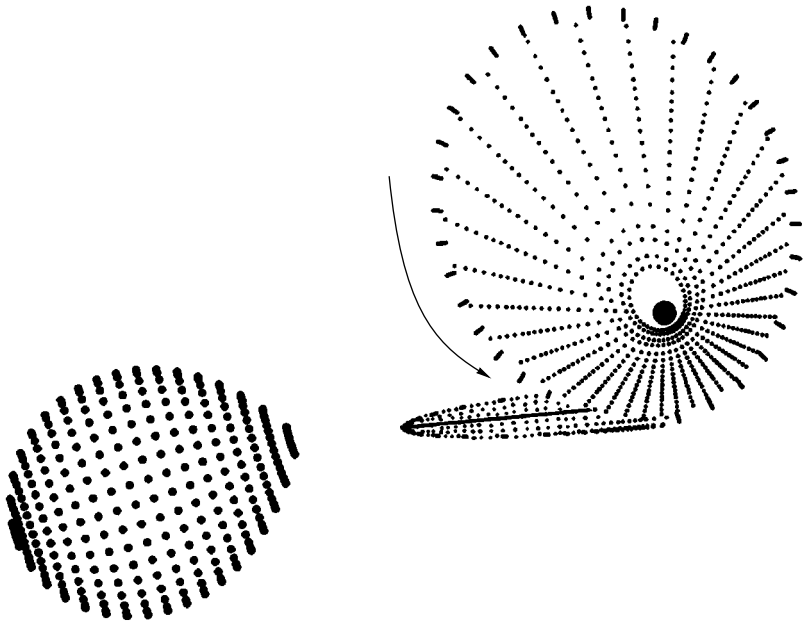

Fig. 2. Schematic of the basic elements of a CBS in the photometric model at orbital phase $\varphi = 0.8$, for orbital inclination $i = 0°$ (view of the system from above). The arrow indicates the direction of gas motion in the disk. The thick curve marks a conventional boundary between the windward and leeward sides of the hot line.

description of the construction of the figure of the hot line and synthesis of the CBS light curve is given in [8].

De-excitation of the shock at the surface of the hot line can occur both at the shock front, i.e., on the side of the incident flow (which we will call the "windward" side), and on the opposite ("leeward") side, depending on the physical parameters and optical depths of the interacting streams (their velocity, density, etc.). In Fig. 2, the thick curve indicates a conventional boundary between the windward and leeward sides of the hot line at the surface of the truncated ellipsoid. Our photometric model assumes that areas on the hot-line surface emit blackbody radiation. This assumption is valid only when the optical depth of the hot line exceeds unity. The temperature of the *i*th area element on the hot-line surface is calculated separately for each of its sides in accordance with the following relation adopted in the model:

$$T_i(y) = T_{\min} + T_{\max}\cos\left(\frac{\pi}{2}\Delta y_i\right), \qquad (4)$$

where y is the coordinate along the major axis of the hot-line ellipsoid, and

$$\Delta y_i = \frac{y_i - y_{\max}}{y_{\min} - y_{\max}}. \qquad (5)$$

For the adopted temperature law, the temperature increment reaches its maximum ($T_i(y) = T_{\min} + T_{\max}$) at the point with coordinate $y_{\max}$, and is equal to zero ($T_i(y) = T_{\min}$) at the point with coordinate $y_{\min}$. We take the minimum temperature to be the temperature of matter a distance r from the white-dwarf center, according to the temperature distribution (3). If $y_{\min}$ and $y_{\max}$ are close to each other, the shock is de-excited within a small region similar to a classical hot spot, but this region is located on the hot line rather than on the disk. The rest of the hot line remains relatively cool ($T \sim 1500$–2000 K). Figure 3 presents the temperature distribution along the major axis of the hot-line ellipsoid from the windward (curve *1*) and leeward (curve *2*) sides. The D indicates the y coordinate of the point of tangency of the hot-line ellipsoid and the lateral surface of the accretion disk, and P indicates the y coordinate of the pole of this ellipsoid. Unlike the case considered in [8], our model supposes that the maximum temperature on the windward side of the hot line $T_{\max}$ is reached at the point of tangency of the stream and the lateral disk surface (in [8], $y_{\max}^{(1)}$ was a free parameter). The maximum temperature of the hot line on the leeward side is shifted toward the point with y coordinate

$$y_{\max}^{(2)} = y_{\max}^{(1)} - dy, \qquad (6)$$

with the displacement dy being a free parameter. Despite the fact that the temperature on the windward side of the hot line is higher than it is on the leeward side, the radiating area there is half that on the leeward side. In addition, the contribution of the windward side of the hot line to the total flux from the system depends not only on the temperature contrast at the surface of the truncated ellipsoid, but also on the position of the

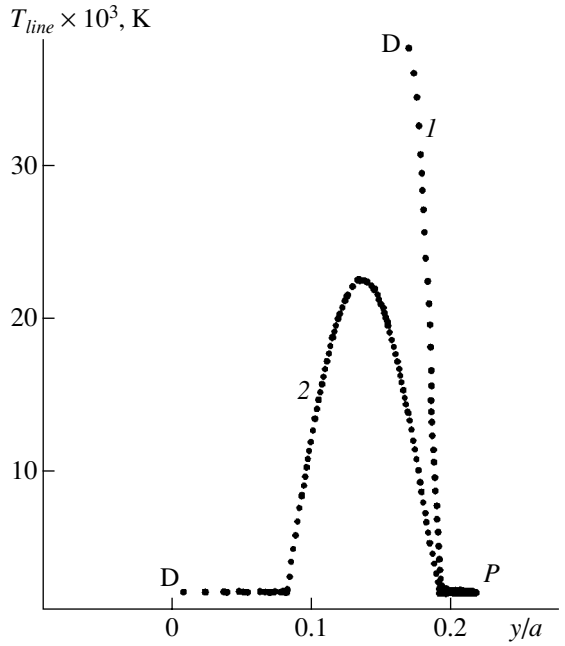

Fig. 3. Temperature distribution along the major axis *Y* of the ellipsoid describing the hot line on the windward (curve *1*) and leeward sides (curve *2*). The D indicates the *y* coordinates of points of tangency between the body of the hot line and the lateral surface of the disk; the *P* indicates the *y* coordinate of the pole of the ellipsoid describing the hot line. The maximum temperature is $T^{(1)}_{\max} = 35370$ K on the windward side of the line and $T^{(2)}_{\max} = 22400$ K on the leeward. The parameters of the de-excitation region are $a_v = 0.088a_0$, $b_v = 0.217a_0$, $c_v = 0.014a_0$, $y_{\min} = 0.19a_0$, and $dy = 0.033a_0$. Other parameters of the CBS correspond to Case 2 from Table 1.

disk and the compactness of the de-excitation zone. The hottest areas on the windward side of the hot line may be obscured from the observer by the lateral surface of the disk or by the donor star.

(6) The parameters of the problem are: the mass ratio of the components $q = M_w/M_2$ (M_w and M_2 are the masses of the white dwarf and donor star); the orbital inclination of the system *i*; the effective temperature of the donor star T_2, without taking into account heating by hot radiation of the white dwarf; the radius and effective temperature of the white dwarf R_w and T_w; the temperature T_{bw} of the surface layer at the equator of the white dwarf, where the accretion occurs; the parameters *e*, *a*, *A*, α_e describing the size, shape, and orientation of the elliptical disk; and, finally, parameters describing the shape of the hot line (a_v, b_v, c_v), the temperature distribution at its surface $y_{\min}$ and *dy* [see (5)], and the temperature itself $T_{\max}$ on both the windward and leeward sides. Thus, in general, the number of unknown parameters reaches 17. In our study, we use the classical temperature distribution along the disk radius 3/4 [14]; otherwise we would have another free parameter. Therefore, it makes sense to try to use the hot-line model to determine the parameters of CBSs whose basic parameters *q*, *i*, T_2, T_w, R_w, *a*, and *A* have independent estimates from other sources.

To estimate the adequacy of the fit of an observed light curve, we calculate the residual

$$\chi^2 = \sum_{j=1}^{n} \frac{(m_j^{\text{theor}} - m_j^{\text{obs}})^2}{\sigma_j^2}, \qquad (7)$$

where m_j^{theor} and m_j^{obs} are the theoretical and observed stellar magnitudes at orbital phase *j*, σ_j^2 is the dispersion of the observations at point *j*, and *n* is the number of points in the curve.

We estimate the model parameters from the CBS light curve using the Nelder–Meade method to minimize the residual functional χ^2 [15]. The solution of the problem or corresponding confidence interval for the obtained parameters is usually taken to be represented by the set of parameters for which the residual is lower than some critical significance level of the distribution $\chi^2_{\eta, N}$. Here, η is the chosen probability for rejecting a correct solution and *N* is the number of normal points in the light curve. If none of the resulting solutions has a residual below the chosen significance level $\chi^2_{\eta, N}$, the effect of varying a particular parameter can be estimated by specifying some arbitrary limiting residual instead of the critical residual—for example, by increasing the minimum residual by about 10%.

A detailed description of the light-curve synthesis, the method used to determine the parameters of the problem, and the results of some model calculations are presented in [8].

4. THE IP Peg SYSTEM

Dwarf novae are a subclass of cataclysmic variables with short outbursts lasting several days, during which the luminosity of the system increases by 3^m–5^m. The outbursts may recur after several weeks or several years, depending on the type of the system.

Variability of IP Peg was detected by Lipovetskiĭ and Stepanyan [16]. Goranskij *et al.* [17] demonstrated that the system is an eclipsing dwarf nova with period $P = 3^h.8$ displaying sharp and deep eclipses, as well as a pronounced orbital hump in its light curve. During its outbursts, which recur with an interval of ~100 days, the brightness of IP Peg increases by approximately $2^m.5$, and its out-of-eclipse *V* magnitude varies from $14^m.7$ in the inactive state (outside eclipse) to ~$12^m.3$ during outburst.

The results of photometric observations of IP Peg are presented in [18–23] and of spectral observations in [24–27]. In the recent spectral observations [28, 29],

Balmer line emission was detected, which comes from the polar regions of the donor star and is the result of heating by the hot radiation of the white dwarf. These spectral observations also provide some evidence that spiral waves can exist in the accretion disk during outbursts in the system.

The presence of the secondary is manifest in the ellipsoidal variability, which can clearly be seen in the infrared. Szkody and Mateo [18] estimated the orbital inclination $i \sim 75°$ and distance $d \sim 130$–142 pc of the system from the *K*-band light curve. According to the color indices, the spectral type of the secondary is M4V. The mass–radius relation indicates that the star is near the main sequence.

Based on the duration of the ingress and egress of eclipses of the components of the IP Peg system by the red dwarf derived from high-speed photometric observations during the main minimum, Wood and Crawford [19] estimated the component mass ratio to be $2.04 < q < 2.86$ and the orbital inclination to be $80.^\circ9 < i < 90°$. Their preferred value was $q \simeq 2.04$ for $i \simeq 80.^\circ9$.

Based on H_β and H_γ observations of the system in the inactive stage, Marsh [24] determined the half-amplitudes of the radial velocity curves for the components to be $K_w = 173 \pm 17$ km/s for the white dwarf and $K_2 = 301 \pm 19$ km/s for the secondary (from absorption lines). In the determination of K_2, possible shifts of the centers of absorption lines due to heating of the donor star by radiation from the inner regions of the disk were taken into account. As a result, the component mass ratio was somewhat lower than that obtained by Wood and Crawford [19]: $q \simeq 1.67 \pm 0.1$. The orbital inclination was estimated to be $i = 79° \pm 0°.9$, the distance between the components to be $a_0/R_\odot = 1.50 \pm 0.08$, and the mass and radii of the components to be $M_w/M_\odot = 1.14 \pm 0.15$, $M_2/M_\odot = 0.67 \pm 0.12$, $R_w/R_\odot = 0.0058 \pm 0.0021$, and $R_2/R_\odot = 0.498 \pm 0.032$. The estimated temperature of the white dwarf was $T_w \leq 15000$ K, based on the flux variations during the egress of the star from eclipse. Martin *et al.* [26] obtained $K_2 = 298 \pm 8$ km/s for the half-amplitude of the radial velocity curve of the secondary, based on observations of He I line emission within a few days of outburst. They also derived component parameters close to those obtained by Marsh [24]: $q = 1.70 \pm 0.11$, $i > 68°$, $K_2 = 298 \pm 8$ km/s, $M_w/M_\odot = 1.15 \pm 0.10$, $M_2/M_\odot = 0.67 \pm 0.08$, and $R_2/R_\odot = 0.502 \pm 0.024$.

Wolf *et al.* [21] detected appreciable variations of the disk radius during outburst. Prior to the outburst, the radius was rather small ($R_d \sim 0.24a_0$); it increased to $\sim 0.37a_0$ on the descending branch after the outburst maximum, and then gradually fell to $\sim 0.26a_0$. After a second outburst, the disk radius again increased to $\sim 0.34a_0$, and then decreased to $\sim 0.28a_0$ after several days. Analysis of the temperature distribution along the disk radius during the outburst indicated that the temperature profile was rather flat, and only on the edge of the disk did it correspond to a "3/4" law. In the inactive state, the temperature variations were close to a classical "3/4" law. The disk temperature during the outburst was ~8000 K in inner regions and ~4500 K at the edge [23]. The IR (1.45–1.85 μm) observations of the system in its inactive state of Froning *et al.* [30] showed that the bulk of the disk has a flat surface-brightness distribution and low brightness temperature (~3000 K). The disk radius suggested by the IR observations is $R_d \sim 0.32a_0$.

The light curve of the system has a pronounced pre-eclipse hump with amplitude $\Delta B \sim 1^m$ [17], which begins near orbital phase $\varphi \sim 0.65$ and reaches its maximum at phases $\varphi \sim 0.8$–0.9. This hump is usually interpreted as the radiation of a hot spot at the boundary of the disk. It is considerably less pronounced in lines than in the continuum. The emission-line light curve displays a nearly *V*-shaped eclipse of the accretion disk by the secondary. The average temperature of a classical hot spot is 11000–13000 K [24]. Szkody [32] obtained a high blackbody temperature of ~20000 K for the spot from IUE spectra. For a spot temperature $T_{sp} = 12000$ K, the vertical size of the hot spot is roughly double the thickness of the outer edge of the disk. The maximum of the hump falls at phase $\varphi \sim 0.85$, which means that the shock front is not perpendicular to either the gas flow (the predicted maximum is located at phase $\varphi \sim 0.78$) or the disk ($\varphi \sim 0.95$), but instead is located somewhere between these values. Along with the regular orbital hump, Wolf *et al.* [33] detected a second hump in the light curve near phase $\varphi \sim 0.4$ in the inactive state of the system, with an amplitude half that of the first hump, which they explained as radiation of the hot spot above the upper edge of the disk. The azimuth of the hot spot in the IR differs both from that specified by the theoretical path of the gaseous flow and from that in the optical [30].

High-time-resolution spectroscopy of IP Peg indicated the presence of a large-scale bright azimuthal structure in the outer parts of the disk during outburst [27, 29, 35–38]. Doppler tomography of IP Peg suggests that these formations are the same as the spiral waves in the accretion disk discovered by Sawada *et al.* [34]. Note that spectra obtained at the end of outburst or in the inactive state do not display spiral waves. Morales-Rueda *et al.* [38] detected a large-scale asymmetry in the system during an outburst, roughly on the line connecting the components, along with the spiral structure in the disk. The asymmetry is manifest in a shift of emission-line eclipses by 0.015–0.045 of the orbital period to phases earlier than the white dwarf eclipse. The hot-line region between the system components may well prove to be this asymmetrical structure.

5. THE *V*-BAND LIGHT CURVE OF IP PEG

5.1. The Hot-Line Model for the Inactive State of IP Peg

To demonstrate the adequacy of the hot-line model for the IP Peg system in its inactive state, we used the light

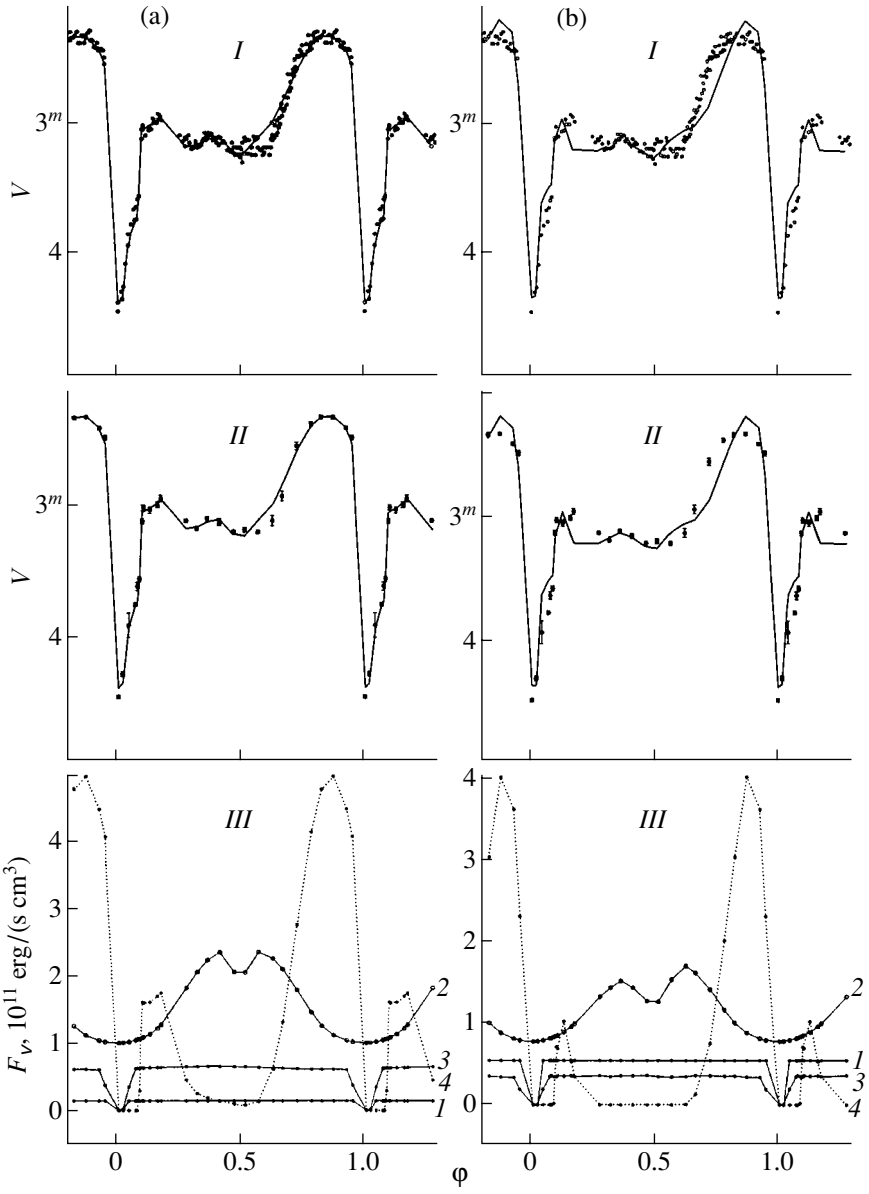

Fig. 4. IP Peg (*I*) observations and (*II*) mean light curve in the *V* filter in the inactive state. The solid curves indicate light curves synthesized with the best-fit parameters (Table 1, "case 1") for the (a) hot-line model and (b) the classical hot-spot model. The graphs *III* present the contribution of the system's components to the total radiation: (*1*) the white dwarf, (*2*) donor star, (*3*) disk, and (*4*) area of energy release (for (a) a hot line or (b) hot spot).

curve of IP Peg in the *V* band obtained during an international coordinated campaign to observe dwarf novae [22]. The light curve combines observations for three nights from December 6 to 26, 1988 corresponding to the inactive state of the system (a regular outburst was detected five days after the latest observation), and provides fairly good coverage of the orbital period [Fig. 4 (plots *I*, *II*)].

The mean light curve is represented by 26 normal points. The critical significance level for $\eta = 0.001$ and number of degrees of freedom $N = 26$ was $\chi^2_{0.001,\,26} = 54.1$.

When estimating the parameters of IP Peg, the intervals of variation for some of them (q, i, R_w, T_w, T_2, a) were restricted using values derived from observations in other studies. Table 1 presents these intervals and the values obtained for the other parameters. In Fig. 4a (graph *I*), the points indicate observations of IP Peg, and the solid curve marks the theoretical light curve synthesized with the parameters given in Table 1 ("case 1"). The theoretical curve fits the observations of the system in the main minimum very well; the time of egress from the white-dwarf eclipse and the amplitude of the brightness jump are approximated well, as is the anomalous hump near $\varphi \sim 0.4$. The fit for out-of-eclipse observations near orbital phases $\varphi \sim 0.6$–0.75 is somewhat worse: the discrepancy between the theoretical

Table 1. Parameters of IP Peg (from *V* observations)

Parameter	Generally accepted value	Classical model (I)	Hot-line model (II)		
			inactive state		active state
			case 1	case 2	
$q = M_w/M_2$	1.56–2.86	2.47	1.707	1.714	1.708
i, deg	78–90	85.4	80.15	80.45	80.11
R_w/a_0	0.0023–0.0056	0.0052	0.0061	0.0061	0.0062
R_2/a_0	0.295–0.373	0.316	0.344	0.344	0.344
T_w, K	≤15000	45965	16009	16188	16200
T_{bw}, K	40000–50000	45965	43246	40300	70045
T_2, K	3100–3400	3397	3424	3403	3445
Disk					
a/a_0	0.24–0.28	0.407	0.308	0.256	
a/a_0 (active)	~0.34–0.37				0.463
z/a	~0.02–0.04	0.031	0.041	0.039	
z/a (active)	~0.2				0.137
Model I: Spot					
Azimuth, deg	18–79	24.5			
R_{sp}/a_0		0.198			
T_{sp}, K	~12000–20000	4530			
Model II					
e		0	0.315	0.251	0.142
α_e, deg			43.8	271	57.4
a_v/a_0			0.041	0.088	0.112
b_v/a_0			0.204	0.217	0.178
c_v/a_0			0.019	0.014	0.098
$\langle T^{(1)} \rangle$, K			17146	13500	–
$T^{(1)}_{\max}$, K			21637	35370	–
$\langle T^{(2)} \rangle$, K			10872	12120	5723
$T^{(2)}_{\max}$, K			21618	20405	6180
χ^2		1199	172	231	1210

Model I is the classical hot-spot model [39], Model II is the hot-line model [8]. The large residual obtained for the light curve in the active state is due to the low rms errors of the normal points.

and observed curves reaches $\Delta m = 0\overset{m}{.}1$. We can see from Fig. 4a (graph *III*), which presents the relative contributions of the system components to the total flux, that the shape and amplitude of the hump at phases $\varphi \sim 0.6$–0.9 is determined primarily by the radiation of the hot line. The white dwarf's contribution is insignificant, mainly due to the small size of the star. The accretion disk is rather cool: the temperature of its inner regions does not exceed 10000–15000 K, and the temperature at the outer edge is $T \sim 2200$–2700 K. The disk has appreciable eccentricity, $e \sim 0.13$, and its orientation is $\alpha_e \sim 44°$. The temperature distribution over the hot-line surface indicates that the areas of energy release are rather compact on both the windward and leeward sides. The temperature of the hot line in the zone of energy release exceeds the disk temperature in adjacent regions by a factor of ~ten. At the maximum, this temperature increases to ~24100 K on the windward side in the shock region, and to ~23400 K on the leeward side. The average hot-line temperatures are ~17150 K and ~10900 K, respectively. The surface of the truncated ellipsoid describing the shape of the hot line is cool near its *y* pole; its temperature is comparable to that of the outer parts of the disk (~2200 K). Note that this is one of a series of solution obtained with approximately the same goodnesses of fit, but over a

broader interval of possible values for q, i, R_w, T_w, T_2, and a. We have chosen this solution because it is in agreement with the results of spectral studies.

The minimum residual for the solution $\chi^2 = 172$ exceeds the critical value $\chi^2_{0.001,\,26} = 54.1$. Note that, in our photometric model, neither the radiation of the stream from L_1 nor that of the circumstellar envelope was taken into account. Also, a set of simplifying assumptions was used. Therefore, the excess of the solution residual over the critical value is natural. To estimate the impact of various parameters on the solution, we used a limit for the residual $\chi^2 = 189$ rather than the critical limit, thereby increasing the minimum residual by 10%. For most of the parameters, the allowed intervals of their variation were within 1–2% of their best-fit values. For the maximum temperatures of the hot line on the windward and leeward sides, the resulting errors are 7.5 and 2.8%, respectively; we have for the parameter dy $\Delta dy \sim 10\%$, and also $\Delta e \sim 3\%$, $\Delta a_v \sim 5.2\%$, $\Delta q \sim 4.8\%$, and $\Delta\alpha_e \sim 12\%$ of the best-fit values for the set of parameters used.

Table 1 ("case 2") contains another solution for the light curve of IP Peg in its inactive state. Here, the eccentricity of the disk is somewhat higher than in the previous case, $e \sim 0.25$, and the orientation $\alpha_e \sim 270°$. This model is characterized by an appreciable difference between the temperatures of the hot line on the windward and leeward sides (Fig. 3): at the maximum, it increases to ~37000 K (±4000 K) on the windward side, and to ~22000 K (±700 K) on the leeward side. The amplitude of the corresponding temperature variation is indicated in parentheses, for an increase of the residual by 10% (to $\chi^2 = 254$) and for the best-fit values of the other parameters. The average hot-line temperatures are ~13500 and ~12120 K, respectively. Figure 5 presents the theoretical light curve and the contributions of the components to the total radiation flux.

5.2. The Classical Hot-Spot Model

When a classical model with a circular disk and a hot spot [39] is used to interpret the IP Peg *V*-band light curve, the consistency between the theoretical curve and the observations becomes appreciably worse [Table 1, Fig. 4b (graphs *I*, *II*)]. We have not been able to adequately fit the out-of-eclipse brightness of the system: at phases $\varphi \sim 0.15$–0.35 and $\varphi \sim 0.65$–0.95, the discrepancy between the theoretical and observed curves reaches $\Delta m = 0\overset{m}{.}25$. In addition, the main minimum with the double eclipse is also fit substantially worse than it is with the hot-line model: at phases $\varphi \sim 0.08$–0.12, the discrepancy between the theoretical and observed curves reaches $\Delta m = 0\overset{m}{.}2$. In the classical model, the amplitude and shape of the hump at phases $\varphi \sim 0.6$–0.9 are also specified primarily by the radiation of a rather extended hot spot (Fig. 4b, graph *III*) with radius $\sim 0.2a_0$. The contribution of the disk and white dwarf to the total radiation flux remain insignificant. The contribution of the radiation from the outflowing component is somewhat asymmetrical about orbital phase $\varphi = 0.5$, due to our allowance for heating of the surface of the donor star by the high-temperature radiation of the hot spot (this heating is asymmetrical about the line connecting the centers of mass of the stars). The classical model requires a supplementary source of radiation to provide the broader hump at phases $\varphi \sim 0.6$–0.9, which cannot be fit with a single hot spot. Thus, the hot-line model is preferable to the classical model as a description of IP Peg's light curve in its inactive state.

5.3. The Hot-Line Model for the Active State of IP Peg

The hot-line model was initially proposed for steady-state flow regimes in CBSs. In outburst, the flows in IP Peg are undoubtedly not steady, so that non-steady-state gas-dynamical models should be used to analyze the light curve in the active state. Nevertheless, we attempted to analyze the light curve of IP Peg at an outburst maximum using the hot-line model. The resulting solution may be useful for determining the domain of applicability for the hot-line model.

We used the *V*-band light curve of IP Peg obtained by Webb *et al.* [31] (Fig. 6) on September 28, 1997 (curve No. 4558) at the very maximum of an outburst. The out-of-eclipse brightness of the system increased by almost a factor of 7.5 (by $2\overset{m}{.}2$) compared to the inactive state of the system. The curve is represented by 28 normal points with errors from $0\overset{m}{.}01$–$0\overset{m}{.}02$ for out-of-eclipse brightness to $0\overset{m}{.}07$ at the minimum of the curve. For this light curve, we appreciably restricted the allowed values for the parameters $q = 1.707 \pm 0.002$, $i = 80\overset{\circ}{.}1 \pm 0\overset{\circ}{.}3$, $R_w/a_0 = 0.0061 \pm 0.0001$, $T_2 = 3424 \pm 30$ K, and $T_w = 16009 \pm 200$ K to the indicated limits. The remaining parameters were varied freely. In addition, we introduced a supplementary free parameter: the power-law index β_g in dependence (3). We assumed that this index may differ from the classical value 3/4 during outburst. This is required by the fact that increasing the disk radius alone during the outburst, even from the inactive-state value $a \sim 0.63R_{L1}$ to the boundary of the critical Roche lobe, is unable to yield the observed increase of the *V* flux. The spectral data indicate that the radiation intensity from the area of energy release (either the hot spot or hot line) varies only little. A fairly good agreement between the theoretical and observed light curves was reached for $\beta_g = 0.6$.

The sixth column of Table 1 contains the resulting parameters of the system; Figs. 6a and 6b present the theoretical curve constructed using these parameters. The out-of-eclipse flux of the system (Fig. 6c) is $F_V \sim 3.2a_0^2$ erg s^{-1} cm^{-3}, which is a factor of ~4.6 higher than at the maximum of the orbital hump in the inactive

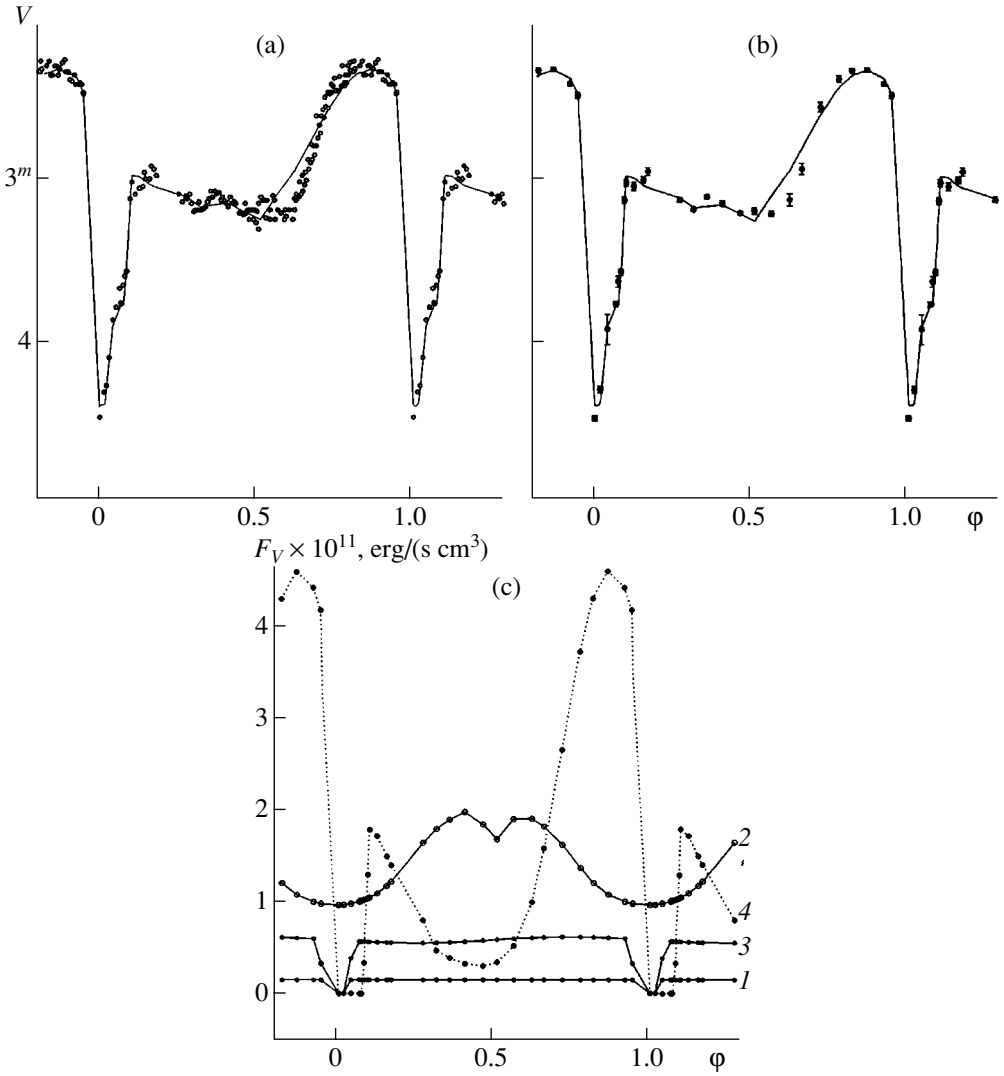

Fig. 5. IP Peg (a) observations and (b) the mean light curve in the *V* filter in the inactive state. The solid curves indicate light curves synthesized with the best-fit parameters (Table 1, "case 2") for the hot line model; (c) contributions of the system's components to the total radiation: (*1*) the white dwarf, (*2*) donor star, (*3*) disk, and (*4*) hot line.

state (Fig. 4c). The low value of the *V* flux (40% lower than observed) may be due to the fact that this model neglects additional sources of radiation, such as the radiation of spiral waves in the accretion disk. Their contribution is no less than ~15% of the total luminosity of the disk, and the temperature in the spiral regions reaches 20000 K [35]. The presence of spiral waves during outburst could also be responsible for the fluctuations of the out-of-eclipse flux (Figs. 6a, 6b). A more complicated model describing the "spiral" distribution of the temperature over the disk is required to test this hypothesis. It is also possible that this discrepancy reflects the non-Planckian character of the radiation from the gaseous structures in CBSs. In this connection, we stress once again that our CBS model can only be used to calculate relative flux variations. The calculation of absolute fluxes and colors requires that the real spectra of gaseous structures in CBS be taken into account, which we plan to do in future studies.

It is notable that, with the parameters used, the hot line model essentially coincides with the classical hot-spot model. With the given size and orientation of the truncated ellipsoid describing the hot line, we obtain only a modest bulge on the lateral surface of the disk instead of a line. The windward side of the hot line is entirely submerged in the disk, and radiation is observed only from the leeward side. This is probably a result of the non-steady-state character of the flow during outburst. The hot-line model is only valid for a steady-flow regime. During outburst, the collision of the expanding disk with the stream results in the formation of a shocked region analogous to a hot spot. The observations appear to be consistent with this picture.

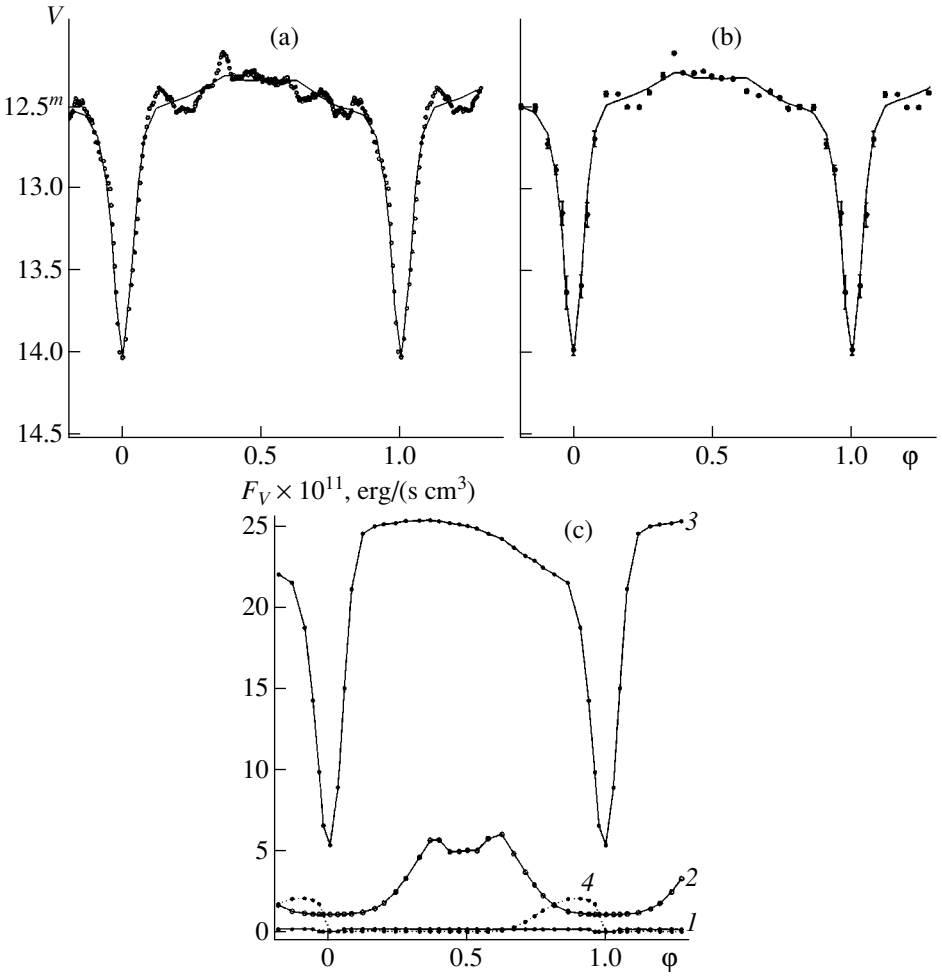

Fig. 6. IP Peg (a) observations and (b) mean light curve in the *V* filter in the maximum of a burst. Solid lines indicate light curves synthesized with the best-fit parameters (Table 1) within the "hot line" model; (c) the contribution from the system components to its total radiation: from the (*1*) white dwarf, (*2*) the donor star, (*3*) the disk and (*4*) the energy release area.

6. THE INFRARED LIGHT CURVE OF IP Peg

The advantages of the CBS model taking into account the extended shock in the region of the collision between the gaseous stream and the matter flowing around the accretion disk were most obvious when we considered the IR light curve of the IP Peg system in its inactive state. We studied the light curve of IP Peg obtained by Froning *et al.* [30] on September 28–30, 1994 in the *H* filter (λ = 1.45–1.85 μm). The nearest outbursts were observed on October 25, 1993 and December 7, 1994. The shape of the light curve was essentially the same on all nights, which enabled combination of all observations into a single curve (Fig. 7a). Attempts to fit this curve using only the ellipsoidal variations of the secondary and a fairly broad range of possible parameter values were unsuccessful [30]. There is apparently a supplementary source of radiation in the system, with intensity comparable to that of a red dwarf at IR wavelengths. This source varies dramatically with orbital phase. It can be neither the accretion disk, whose contribution does not exceed 8% of the total flux (according to various estimates), nor a classical hot spot, which can be observed only in a narrow interval of orbital phases. It is even less likely to be the white dwarf, whose contribution in the IR is negligibly small.

The results of our interpretation of the IP Peg light curve in the *H* filter in both a classical hot-spot model and a hot-line model are presented in Table 2. Analyzing the light curve in the hot-line model, we restricted the allowed intervals for the parameters $q = 1.707 \pm 0.003$, $i = 80°.1 \pm 0°.5$, $R_w/a_0 = 0.0061 \pm 0.0001$, $T_2 = 3420 \pm 50$ K, and $T_w = 16000 \pm 350$ K within the indicated limits, as was done for the *V*-band light curve during outburst. The remaining parameters were varied freely, including the power-law index β_g in (3). Figures 7a and 7b present the observed light curves and the theoretical curves synthesized using the parameters from Table 2. This figure indicates excellent agreement between the curves: both the amplitudes of the bright-

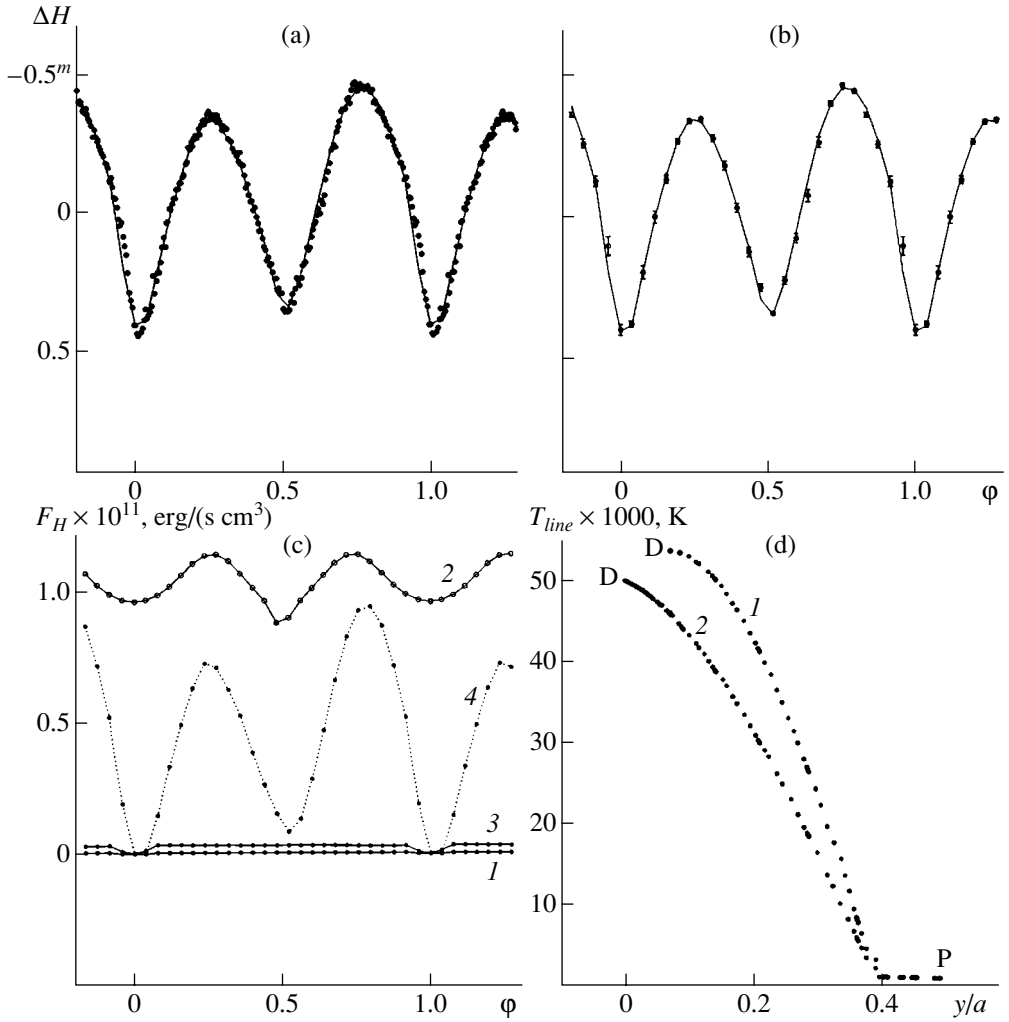

Fig. 7. IP Peg (a) observations and (b) mean light curve in the *H* filter in the inactive state. The solid curves indicate light curves synthesized with the best-fit parameters (Table 2) for the hot-line model; (c) contribution of the system's components to its total radiation: (*1*) the white dwarf, (*2*) donor star, (*3*) disk, and (*4*) hot line; (d) temperature distribution along the major axis *Y* of the ellipsoid describing the hot line on the windward (curve *1*) and leeward (curve *2*) sides, obtained from the analysis of the IP Peg light curve in the inactive state. The maximum temperature is $T^{(1)}_{\max} = 50720$ K on the windward side of the line and $T^{(2)}_{\max} = 48100$ K on the leeward side. The parameters of the de-excitation region are $a_V = 0.018a_0$, $b_V = 0.502a_0$, $c_V = 0.014a_0$, $y_{\min} = 0.39a_0$, and $dy = 0.13a_0$.

ness maxima and the depths and widths of the minima are well fit.

The size of the accretion disk (more exactly, of the part that is optically thick in the near-IR) is small: $R_d/a_0 \sim 0.12$–0.22 ($a/a_0 \simeq 0.17$, $e \simeq 0.29$). Its contribution to the total flux is 1.5–2%; its out-of-eclipse flux is essentially constant and does not appreciably affect the light-curve shape. The radial temperature dependence of the disk, indeed, deviates from the "3/4" law (we find from the solution $\beta_g = 0.69$); however, due to the small contribution of the disk radiation to the total flux, this should not be considered a firm conclusion. The brightness temperature of the inner part of the disk reaches 9000–13000 K; the brightness temperature in the outer regions of the optically thick region of the disk decreases to 2000–3000 K.

As expected, the largest contribution to the total flux (~60% in quadrature) comes from the red dwarf, whose polar region is heated by hot radiation from the boundary layer of the white dwarf (Fig. 7c). The parameters of the donor star (mass, radius, and temperature) correspond to the values we obtained from the *V*-band light curve. More unexpected is the rather substantial contribution of the hot line to the near-IR light curve. Both the windward and leeward sides of the hot line are required to explain the residual radiation obtained by Froning *et al.* [30] after removing the ellipsoidal variability of the donor star from the light curve. The brightness temperature of the hot line (Fig. 7d) at the $\tau \sim 1$ level

Table 2. Parameters of IP Peg (in the inactive state) from *H* observations

Parameter	Generally accepted values	Classical model (I)	Hot-line model (II)
$q = M_w/M_2$	1.56–2.86	2.146	1.705
i, deg	78–90	80.33	80.34
R_w/a_0	0.0023–0.0056	0.0063	0.0061
R_2/a_0	0.295–0.373	0.325	0.344
T_w, K	≤15000	38145	16349
T_{bw}, K	40000–50000	38145	23620
T_2, K	3100–3400	3477	3468
Disk			
a/a_0	~0.33	0.57	0.17
z/a	~0.02–0.04	0.028	0.0047
β_g	≤0.75	0.75	0.69
Model I: Spot			
Azimuth, deg	~60	80	
R_{sp}/a_0	0.1–0.15	0.144	
T_{sp}, K	~10000	17130	
Model IU			
e			0.288
α_e			66.6
a_v/a_0			0.018
b_v/a_0			0.502
c_v/a_0			0.014
$\langle T^{(1)} \rangle$, K			27880
$T^{(1)}_{\max}$, K			50720
$\langle T^{(2)} \rangle$, K			25300
$T^{(2)}_{\max}$, K			48100
χ^2		2681	49

reaches 54000 K on the windward and 50000 K on the leeward side; the opaque part of the line is fairly narrow and extended. This can explain the substantial flux of the *H* radiation at orbital phases $\varphi \sim 0.1$–0.4, and this is precisely the part of the orbital light curve that cannot be fit with the classical hot-spot model.

When we compare the calculated model parameters in the visible (Table 1) and IR (Table 2), it is clear that they are in good agreement, given that the analyzed light curves were obtained at different times and probably at different phases of activity of the system. The only parameter that changes appreciably is the temperature of the hot line, which roughly doubles in the transition from optical to IR wavelengths. This may be due to the deviation of the hot-line radiation from a blackbody law. If we suppose that bremsstrahlung and recombination radiation contribute significantly to the total radiation of the hot line, an increase in the brightness temperature in the transition toward longer wavelengths is natural. The intensity of thermal bremsstrahlung and recombination radiation increases by more than a factor of two when the frequency decreases from $\nu = 10^{15}$ Hz to $\nu = 10^{14}$ Hz; i.e. in the transition from optical to IR frequencies. At the same time, the specific intensity of a blackbody with temperature $T > 10^4$ K decreases in the transition from $\nu = 10^{15}$ Hz to $\nu = 10^{14}$ Hz. This means that the fraction of non-thermal radiation significantly increases in the shift from the *V* to the *H* band, increasing the model brightness temperature of the hot line.

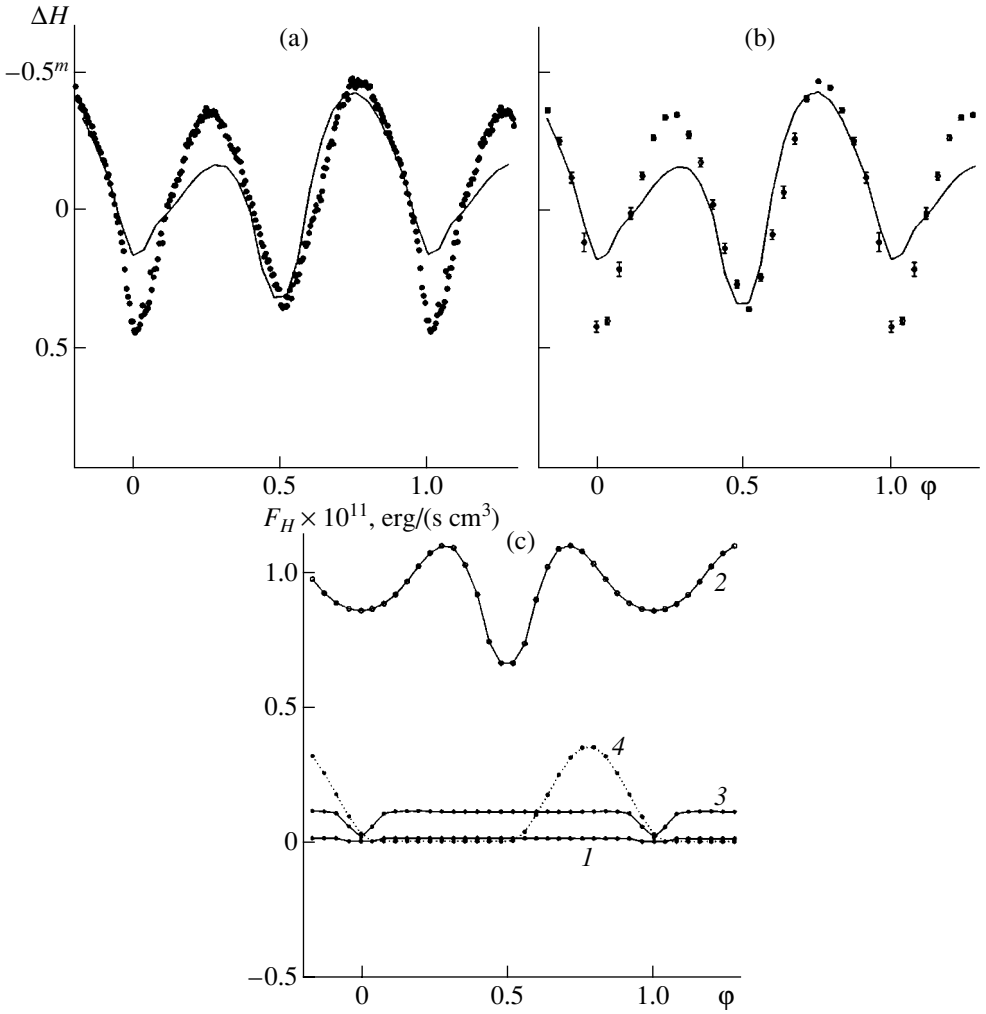

Fig. 8. IP Peg (a) observations and (b) mean light curve in the *H* filter in the inactive state. The solid curves indicate light curves synthesized with the best-fit parameters (Table 2) for the classical hot-spot model; (c) contribution of the system's components to the total radiation: (*1*) the white dwarf, (*2*) donor star, (*3*) disk, and (*4*) hot spot.

In the classical model, the allowed parameter intervals were appreciably broader than in the previous model, however we were not able to find an acceptable fit (Table 2). While the classical model provides a more or less reasonable fit for the light curve at orbital phases $\varphi \sim 0.4$–0.9, primarily due to the radiation of the hot spot (Fig. 8c), the agreement becomes quite poor at phases $\varphi \sim 0.9$–0.4 (Figs. 8a, 8b). The disk's contribution to the total flux is small (~7%), despite the fact that its optically thick part is very large ($R_d \sim 0.57a_0 \simeq 0.99R_{L1}$). This is consistent with the results of [18, 30]. The disk is rather cool: the brightness temperature at its outer edge is ~1500 K, the radial temperature distribution corresponds to $\beta_g \simeq 0.75$, the temperature of the bulk of the disk is 3500–2000 K.

In the classical model, the size of the hot spot at near-IR wavelengths ($r \sim 0.144a_0$) is roughly the same as that estimated by Froning *et al.* [30]; however, the azimuth of the spot (~80°) is closer to that obtained at visible wavelengths (Table 2). The contribution of the spot to the total flux is ~22% at phases $\varphi \sim 0.75$. As in the hot-line model, the main contribution to the total flux is made by the late-type star (up to ~70% at $\varphi \sim 0.75$ and up to 90% at $\varphi \sim 0.25$).

7. DISCUSSION

Our interpretation of the eclipsing light curve of the cataclysmic variable IP Peg in the framework of two alternative models indicates that the hot-line model can fit the observed light curves in the quiescent state better than the hot-spot model. For example, the hot-line model provides a better fit of the widths of humps in the light curves, the shapes of eclipses, and the details of the out-of-eclipse brightness variations. This is due, in particular, to the fact that the projection onto the plane of the sky of the area of a classical hot spot with its quasi-flat surface varies rapidly during its orbital motion, resulting in the appearance of relatively narrow

humps in the eclipse light curve. In the hot-line model, the bright interaction region is an extended semi-transparent structure, whose projection onto the plane of the sky varies more smoothly with orbital phase. In addition, since the hot line supposes the de-excitation of hot plasma both forward, in the direction of orbital motion, and backward (depending on the optical depths of the interaction region and the gas stream), the hot-line model can produce broader humps in the eclipse light curve, in better agreement with the observations.

Relatively bright regions of the hot line are also observable at phases $\varphi \sim 0.5$–0.6, when a classical hot spot at the outer boundary of the disk would be invisible. Finally, if the luminosity of the hot line on the windward side exceeds that of the lateral surface of the disk, this will result in the observed increase of the flux from the system at phases $\varphi \sim 0.1$–0.2, which is completely ruled out in the classical model.

The interpretation of the IR light curves of IP Peg demonstrates convincingly the advantages of the flow model with a hot line. The residual χ^2 for the fit of the theoretical to the observed light curves for the model with a shockless interaction between the gaseous stream and the disk is 49, whereas $\chi^2 = 2681$ for the standard hot-spot model.

ACKNOWLEDGMENTS

This study was supported by the Russian Foundation for Basic Research (project codes 99-02-17619, 99-02-17589, 00-02-16471), and also by Presidential grants of the Russian Federation (99-15-96022, 00-15-96722, 00-15-96553).

REFERENCES

1. D. V. Bisikalo, A. A. Boyarchuk, O. A. Kuznetsov, and V. M. Chechetkin, Astron. Zh. **74**, 880 (1997) [Astron. Rep. **41**, 786 (1997)].
2. D. V. Bisikalo, A. A. Boyarchuk, O. A. Kuznetsov, and V. M. Chechetkin, Astron. Zh. **74**, 889 (1997) [Astron. Rep. **41**, 794 (1997)].
3. D. V. Bisikalo, A. A. Boyarchuk, V. M. Chechetkin, *et al.*, Mon. Not. R. Astron. Soc. **300**, 39 (1998).
4. V. G. Gorbatskiĭ, Astrofizika **3**, 245 (1967).
5. J. Smak, Acta Astron. **20**, 312 (1970).
6. M. Makita, K. Miyawaki, and T. Matsuda, Mon. Not. R. Astron. Soc. **316**, 906 (2000).
7. D. V. Bisikalo, A. A. Boyarchuk, O. A. Kuznetsov, *et al.*, Astron. Zh. **75**, 40 (1998) [Astron. Rep. **42**, 33 (1998)].
8. T. S. Khruzina, Astron. Zh. **78**, 298 (2001) [Astron. Rep. **45** (4), 255 (2001) in press].
9. B. Warner, *Cataclysmic Variable Stars* (Cambridge Univ. Press, Cambridge, 1995).
10. D. V. Bisikalo, A. A. Boyarchuk, O. A. Kuznetsov, *et al.*, Astron. Zh. **75**, 706 (1998) [Astron. Rep. **42**, 621 (1998)].
11. D. V. Bisikalo, A. A. Boyarchuk, V. M. Chechetkin, *et al.*, Astron. Zh. **76**, 905 (1999) [Astron. Rep. **43**, 797 (1999)].
12. D. V. Bisikalo, A. A. Boyarchuk, O. A. Kuznetsov, and V. M. Chechetkin, Astron. Zh. **77**, 31 (2000) [Astron. Rep. **44**, 26 (2000)].
13. T. S. Khruzina, Astron. Zh. **77**, 510 (2000) [Astron. Rep. **44**, 446 (2000)].
14. N. I. Shakura and R. A. Sunyaev, Astron. Astrophys. **24**, 337 (1973).
15. D. M. Himmelblau, *Applied Nonlinear Programming* (McGraw-Hill, New York, 1972; Mir, Moscow, 1975), p. 163.
16. V. A. Lipovetskiĭ and Dzh. A. Stepanyan, Astrofizika **17**, 573 (1981).
17. V. P. Goranskij, S. Yu. Shugarov, E. I. Orlowsky, and V. Yu. Rahimov, Inf. Bull. Var. Stars, No. 2653 (1985).
18. P. Szkody and M. Mateo, Astron. J. **92**, 483 (1986).
19. J. Wood and C. S. Crawford, Mon. Not. R. Astron. Soc. **222**, 645 (1986).
20. J. H. Wood, T. R. Marsh, E. L. Robinson, *et al.*, Mon. Not. R. Astron. Soc. **239**, 809 (1989).
21. S. Wolf, K. H. Mantel, K. Horne, *et al.*, Astron. Astrophys. **273**, 160 (1993).
22. E. T. Harlaftis, T. R. Marsh, V. S. Dhillon, and P. A. Charles, Mon. Not. R. Astron. Soc. **267**, 473 (1994).
23. A. Bobinger, K. Horne, K.-H. Mantel, and S. Wolf, Astron. Astrophys. **327**, 1023 (1997).
24. T. R. Marsh, Mon. Not. R. Astron. Soc. **231**, 1117 (1988).
25. F. V. Hessman, Astron. J. **98**, 675 (1989).
26. J. C. Martin, M. T. Friend, R. C. Smith, and D. H. P. Jones, Mon. Not. R. Astron. Soc. **240**, 519 (1989).
27. T. R. Marsh and K. Horne, Astrophys. J. **349**, 593 (1990).
28. D. Steeghs, Mon. Not. R. Astron. Soc. **281**, 626 (1996).
29. D. Steeghs, E. T. Harlaftis, and K. Horne, Mon. Not. R. Astron. Soc. **290**, L28 (1997).
30. C. S. Froning, E. L. Robinson, W. F. Welsh, and J. H. Wood, Astrophys. J. **523**, 399 (1999).
31. N. A. Webb, T. Naylor, Z. Ioannou, *et al.*, Mon. Not. R. Astron. Soc. **310**, 407 (1999).
32. P. Szkody, Astron. J. **94**, 1055 (1987).
33. S. Wolf, H. Barwig, A. Bobinger, *et al.*, Astron. Astrophys. **332**, 984 (1998).
34. K. Sawada, T. Matsuda, and I. Hachisu, Mon. Not. R. Astron. Soc. **219**, 75 (1986).
35. E. T. Harlaftis, D. Steeghs, K. Horne, *et al.*, Mon. Not. R. Astron. Soc. **306**, 348 (1999).
36. A. Bobinger, H. Barwig, H. Fiedler, *et al.*, Astron. Astrophys. **348**, 145 (1999).
37. R. Baptista, E. T. Harlaftis, and D. Steeghs, Mon. Not. R. Astron. Soc. **314**, 727 (2000).
38. L. Morales-Rueda, T. R. Marsh, and I. Billington, Mon. Not. R. Astron. Soc. **313**, 454 (2000).
39. T. S. Khruzina, Astron. Zh. **75**, 209 (1998) [Astron. Rep. **42**, 180 (1998)].

Translated by K. Maslennikov

Astronomy Reports, Vol. 45, No. 7, 2001, pp. 553–563. Translated from Astronomicheskiĭ Zhurnal, Vol. 78, No. 7, 2001, pp. 642–654.

Optical Spectra of Three AGB Stars

V. G. Klochkova[1], G. Zhao[2], V. E. Panchuk[1], and N. S. Tavolganskaya[1]

[1]*Special Astrophysical Observatory, Russian Academy of Sciences, Nizhniĭ Arkhyz, Karachaevo-Cherkesskaya Republic, 357169 Russia*

[2]*Beijing Astronomical Observatory, 20A Datun Road, Chaoyang District, Beijing, 100012 People's Republic of China*

Received October 26, 2000

Abstract—The basic parameters and detailed chemical compositions of three asymptotic giant branch stars with similar effective temperatures and surface gravities have been determined using CCD spectra obtained with the échelle spectrometers of the SAO 6-m telescope. The metallicity and chemical composition of the optical counterpart of the OH/IR star IRAS 18123 + 0511 have been derived for the first time. The abundance $[X/H]_\odot$ of the iron group elements (V, Cr, Fe) is –0.45 dex. An overabundance of oxygen, $[O/Fe]_\odot = 1.44$ dex, is detected in the atmosphere of this star. The abundances of *s*-process heavy elements are not enhanced, and are instead underabundant with respect to the metallicity: the average value of $[X/Fe]_\odot$ for Y, Zr, Ba, La, Ce, Pr, Nd is –0.25. The derived abundances confirm that IRAS 18123 + 0511 is in the AGB stage of its evolution. The metallicity of the object, together with its radial velocity $V_r = 78.0$ km/s and Galactic latitude $|b| = 11°$, suggest that it belongs to the old disk population. The expansion velocity of the circumstellar envelope, $V_{exp} \approx 21$ km/s, is derived from the positions of circumstellar absorption bands. The set of parameters obtained for the low-metallicity, high-latitude supergiants BD + 18° 2757 and BD + 18° 2890 (with iron abundances $[Fe/H]_\odot = -2.10$ and –1.48, respectively) confirm that they are evolved halo stars, and probably UU Her-type stars. © *2001 MAIK "Nauka/Interperiodica".*

1. INTRODUCTION

For a number of years, we have used high-resolution spectra obtained on the 6-m telescope of the Special Astrophysical Observatory to study stars during a short stage in their evolution—the transition from the asymptotic giant branch (AGB) to planetary nebulae [1–10]. Stars in this transition stage are usually referred to as post-AGB objects or protoplanetary nebulae (PPN). The main aim of our program is to study the chemical-abundance peculiarities of these objects, which have passed through a series of energy sources, mixing, and dredge-up of material from layers with modified chemical composition to the surface. The history of the mass loss due to the strong stellar wind in the AGB and post-AGB stages, when a circumstellar gas–dust envelope having complex distributions of density and expansion velocity forms around the PPN, is a separate question.

An important role in this program is played by studies of stars in the previous (AGB) stage of evolution: their parameters can provide a reference point for comparative analyses of the parameters of the PPN studied. AGB stars have high absolute luminosities, so that even rather distant objects of this type can be observed with high spectral resolution. This makes it possible to study their chemical composition, which is important from the viewpoint of the evolution of the chemical composition of both our Galaxy and other galaxies. In the current paper, we report spectroscopic results for three cool stars that are close to the AGB stage.

In the AGB stage, intermediate-mass stars (3–8$M_\odot$) lose mass at a high rate, up to $10^{-4}M_\odot$/year. The extensive circumstellar envelope that is formed is manifested as a source of IR continuum, SiO, H_2O, and OH maser emission, and thermal CO emission.

Known types of AGB objects include Mira variables, carbon stars, and OH/IR stars. Miras have comparatively hot envelopes, are associated with H_2O masers and main-line OH masers, and are the descendants of stars that had mass-loss rates lower than $10^{-5}M_\odot$/year [11]. OH/IR stars are thought to correspond to the final phase of the evolution of oxygen-rich AGB stars that had mass-loss rates higher than $10^{-5}M_\odot$/year and are now rapidly evolving to the PPN stage.

Since OH masers emitting in the 1612-MHz line and having no associated H_2O or SiO masers are chronologically the nearest predecessors of PPN [11], comparisons with PPN require spectral observations of precisely this type of OH/IR star. In our spectroscopic study of supergiants with large IR excesses (PPN candidates), we obtained optical spectra of the OH/IR star IRAS 18123 + 0511 for the first time. This has enabled us to determine the fundamental parameters of the object, its detailed chemical composition, and its radial velocity; to identify interstellar and circumstellar features in its spectrum; and to draw fairly firm conclusions about its evolutionary status.

The source IRAS 18123 + 0511, first detected by IRAS, was not identified with any known object in the

Table 1. Parameters of the stars

Star	V	l	b	$T_{\rm eff}$, K	log$g$	[Fe/H]$_\odot$
BD + 18° 2757	9.83	354°	76°	4897	0.80	–2.4
BD + 18° 2890	9.77	16	65	5023	2.24	–1.8
IRAS 18123 + 0511	10.10	33	11			

optical. Iyengar and Parthasarathy [12] included IRAS 18123 + 0511 in their sample of 33 unidentified IRAS sources, but, in contrast to other objects in their program, they made no *BVRI* photometric observations of IRAS 18123 + 0511, and only an estimate of its V magnitude made using the Palomar plates is available (Table 1). Prior to our work, the optical counterpart of this IR source had not been investigated even photometrically.

According to its position in IR color–color diagrams for 25–60 μm and 12–25 μm, IRAS 18123 + 0511 belongs to group IIIa in the classification of van der Veen and Habing [13], which is made up primarily of AGB stars with extended oxygen-rich circumstellar envelopes. IRAS 18123 + 0511 was included in the 1612-MHz OH-line Arecibo survey of IRAS sources [14]. Significant flux in the 1612-MHz line was detected, but the line profile contains only one broadband feature centered at radial velocity V_{LSR} = 85.0 km/s. The parabolic shape of the profile suggests a considerable optical depth for the circumstellar envelope in the OH maser emission. Engels and Lewis [15] observed a sample of OH/IR stars in the 22-MHz H_2O maser line. Neither the water-maser band nor OH main lines were detected in IRAS 18123 + 0511, indicating that we are observing an extremely early phase of PPN formation, immediately following the termination of mass loss and the onset of the detachment of the envelope [11, 16].

For comparison with the parameters of IRAS 18123 + 0511, we obtained the spectra of two stars whose temperatures and luminosities indicate that they are in the AGB stage, but which have no IR excesses. We took both objects from the catalog of Bartkevicius [17], which contains an extensive list of luminous Galactic field stars. This list is of interest for studies of the evolution of the chemical composition of the Galaxy, since it contains a large sample of low-metallicity stars that are on the subgiant and giant branches, as well as the horizontal and asymptotic giant branches. We selected BD + 18° 2757 and BD + 18° 2890, whose basic parameters are listed in Table 1. The values of $T_{\rm eff}$, log$g$, and [Fe/H]$_\odot$ given in Table 1 were obtained by Tautvaisiene [18] based on measurements of photometric indices in the Vilnius system.

All three objects lie near the AGB, and have similar effective temperatures and luminosities, however there are appreciable differences in other parameters. For example, the supergiants BD + 18° 2757 and BD + 18° 2890 have no IR excess, probably because they have not reached the stage in their evolution when matter is ejected from their upper layers. In contrast, IRAS 18123 + 0511 is a rather strong IR source; in particular, as noted above, it is identified with a maser source emitting in the hydroxyl line [14].

These objects also have different positions in the Galaxy. BD + 18° 2757 and BD + 18° 2890 are located at high Galactic latitudes (Table 1), whereas IRAS 18123 + 0511 lies closer to the Galactic plane, suggesting these objects may belong to different Galactic populations.

In the following sections of this paper, we present the detailed chemical compositions of IRAS 18123 + 0511, BD + 18° 2757, and BD + 18° 2890. Our main aim was to determine the fundamental parameters of the stars and derive their detailed chemical compositions using a uniform approach and a homogeneous set of spectral observations. First and foremost, we were concerned with the abundances of lithium and *s*-process elements. In addition to the chemical compositions, we have derived radial-velocity data from various spectral features.

2. OBSERVATIONS, DATA REDUCTION, AND SPECTRAL ANALYSIS

We obtained the spectral data on the 6-m telescope of the Special Astrophysical Observatory with the PFES [19] and LYNX [20] échelle spectrometers in the primary focus and Nasmyth focus, respectively. The mean times for the observations are given in Table 2. The signal-to-noise ratios (S/N) for all spectra used in our analysis are appreciably greater than 100, yielding reliable equivalent-width measurements for weak lines, down to 3–5 mÅ.

The PFES échelle spectrometer is equipped with a 1160 × 1040 CCD array with pixel size 16 × 16 μm designed at the Special Astrophysical Observatory. The PFES spectrometer provides a spectral resolution of about 15000 simultaneously over the wavelength range 4550–7930 Å.

The resolution of the spectra obtained with the LYNX échelle spectrometer exceeds R = 25000. When used with the same CCD array (1160 × 1040 pixels), the spectrum from 4725–6325 Å (or 4000–4790 Å) can be recorded in a single integration, since the optical setup of the spectrometer enables rapid changing of the spectral interval, depending on the observational program.

We reduced the two-dimensional images (the standard procedures of subtracting the dark signal, removing cosmic-ray traces, subtracting scattered light, extracting the échelle orders) using the ECHELLE context of the MIDAS system (version 1998). We carried out spectrophotometric and position measurements on the one-dimensional spectra using the DECH20 package developed by Galazutdinov [21].

Since the LYNX and PFES échelle spectrometers simultaneously recorded a broad spectral range, we were able to determine the basic model parameters $T_{\rm eff}$ and $\log g$ using only spectral criteria free of the effects of interstellar and circumstellar reddening. It is especially difficult to take reddening into account in the case of objects with circumstellar envelopes, since some (poorly determined) fraction of the reddening is due to circumstellar absorption. For IRAS 18123 + 0511, the "spectroscopic" method for determining basic model-atmosphere parameters is currently the only one feasible, since, as noted above, no multicolor photometric or spectrophotometric data are available for this object. We derived its effective temperature from the condition that the neutral-iron abundances be independent of the excitation potentials of the corresponding lines. We chose the surface gravity based on the condition of ionization balance for the iron atoms, and the microturbulence velocity based on the condition that the derived iron abundances be independent of the line intensities. Figure 1 illustrates our choice of model parameters for spectrum s24503 of IRAS 18123 + 0511.

When determining the basic model-atmosphere parameters ($T_{\rm eff}$ and $\log g$) and calculating the chemical composition and synthetic spectra, we used the grid of cool-star model atmospheres of Gustafsson *et al.* [22], calculated in a hydrostatic approximation. The oscillator strengths *gf* of the spectral lines used to determine the model parameters and elemental abundances are given in [3, 9].

When deriving the parameters of a model atmosphere, it is important to limit the analysis to low- and moderate-intensity lines. The approximation of a stationary plane-parallel atmosphere begins to fail for the strongest spectral features. Furthermore, some strong absorption lines can form in the circumstellar envelope, and the intensity of the envelope component will be included in the intensity of the atmospheric component if the spectral resolution is not sufficient to distinguish these. At the same time, the amount of material in the

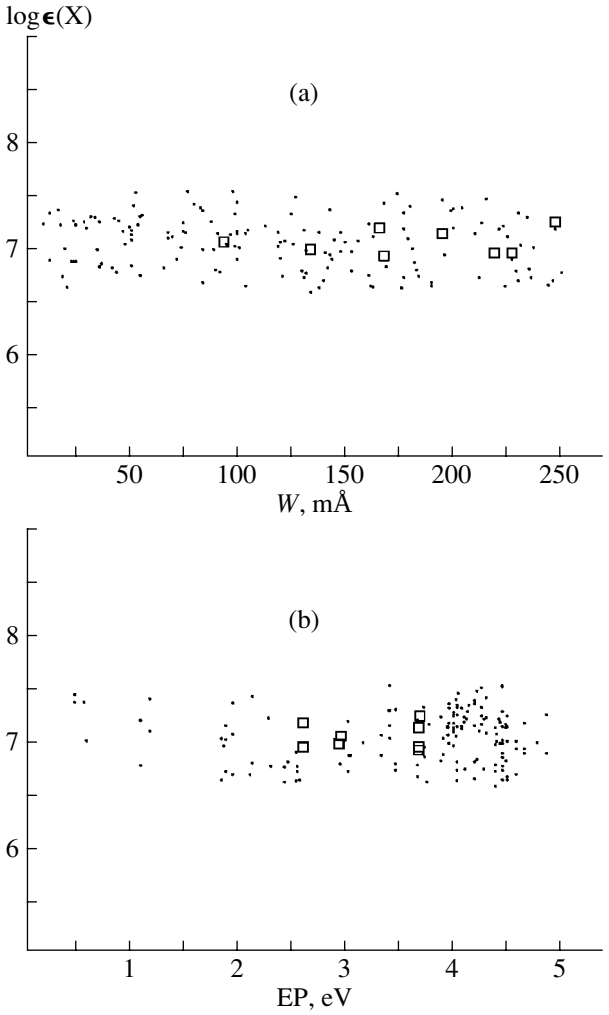

Fig. 1. Iron abundance $\log\epsilon$ in the atmosphere of IRAS 18123 + 0511, found from lines of neutral atoms (points) and ions (squares), as a function of (a) line equivalent width *W* and (b) the excitation potential EP of the transition lower level.

Table 2. Observation log and heliocentric radial velocities, measured from various features in the optical spectra

Star	Spectrum no.	JD 2451000+	$V_\odot$, km/s			
			metals	Hα	IS	DIB
IRAS 18123 + 0511	s24503	366.287	74.9	77.1	−5.1	54.2
	s25305	388.278	79.0	79.9	−2.8	64.8
	s25703	413.278	80.2	80.7	−4.5	52.3
BD + 18° 2757	s23217	246.385	−30.7	−30.4		
	s23601	334.309	−25.7	−24.3		
BD + 18° 2890	s23220	245.451	−35.8	−37.1		

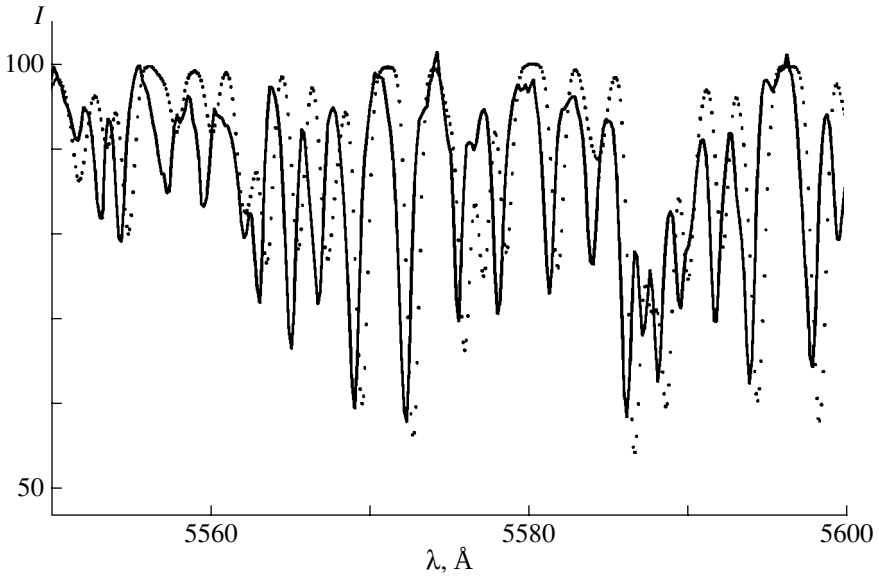

Fig. 2. Comparison of the theoretical (points) and observed (solid curve) spectra of IRAS 18123 + 0511 in the wavelength range free of telluric, circumstellar, and interstellar features. For clarity, the synthetic spectrum is shifted slightly in wavelength relative to the observed spectrum.

cool envelope is not sufficient to form weak lines, which are mainly due to transitions from high-excitation levels [3]. Therefore, using the above criteria for the entire set of lines leads to significant errors in the atmospheric parameters [24]. Studies of molecular spectra formed in the envelopes of post-AGB stars have shown that the state of matter in the envelope cannot be described assuming thermodynamic equilibrium in the stellar atmosphere [3, 23]. We limited our analysis to lines with $W \le 0.25$ Å. Only for Zn and Ba were we forced to use stronger lines ($W \le 0.3$ Å for Zn and $W \le 0.6$ Å for Ba), due to the absence of weaker lines. Although barium is not overabundant, the barium ion lines in the spectrum of IRAS 18123 + 0511 are appreciably enhanced due to the very high luminosity of the star ($\log g \le -0.2$).

Thus, we estimated the effective temperature based on the condition that the iron abundance be independent of the excitation potential of the lower level of the lines used. Additional criteria that can help to ensure reliability of the method is that this also be true for other elements that have numerous lines in the spectra (such as Ca I, Si I, Sc II, Ni I). Moreover, if the microturbulence velocity can be determined with certainty, the individual abundances should show no dependence on the equivalent widths of the lines used for the analysis. The titanium abundances determined from neutral-atomic and ionic lines are consistent within the errors for the method used. This provides evidence that our value for the atmospheric gravity, found from the condition of ionization balance for the iron atoms, is correct. Overall, the internal consistency of the parameters indicates the suitability of the uniform model atmospheres we have used to calculate the weak lines in an LTE approximation. Tables 3 and 4 list the parameters derived for the model atmospheres of the objects studied ($T_{\rm eff}$, $\log g$, ξ_t, $[{\rm Fe/H}]_\odot$).

The typical accuracies of the model parameters for a star with a temperature of 4500–4800 K are $\Delta T_{\rm eff} \approx 70$ K, $\Delta \log g \approx 0.2$ dex, $\Delta \xi_t \approx 0.5$ km/s. We should bear in mind that most of the lines used to calculate the chemical compositions have equivalent widths of up to 100–150 mÅ; this makes appreciable demands on the accuracy of the observational data, since, for a given spectral resolution, the accuracy of W for weak lines depends primarily on the signal-to-noise ratio in the spectrum. The scatter of the elemental abundances obtained from a set of lines is insignificant, and the error δ of the mean value usually does not exceed 0.10–0.12 dex when the number of lines exceeds 8–10 (see Tables 3 and 4). Note that we have made no corrections for hyperfine structure and isotopic shifts, which broaden the lines of Ni I, Mn I, and Ba II.

To check the trustworthiness of the parameters for the model atmosphere of IRAS 18123 + 0511, we compared the observed spectrum with a synthetic spectrum calculated using the STARSP software [25]. By means of illustration, Fig. 2 presents a comparison of the theoretical and observed spectra in the wavelength range free from telluric and circumstellar features. The agreement is satisfactory, considering that the optical counterpart of IRAS 18123 + 0511 is a cool supergiant with an extended atmosphere having a complex structure due to the presence of dynamic phenomena and a gas–dust envelope, while the synthetic spectrum is based on a one-dimensional model in a hydrostatic approximation.

Table 3. Chemical composition $\log\epsilon(X)$ of IRAS 18123 + 0511 (with $\log\epsilon(H) = 12.0$)[1]

The Sun		IRAS 18123 + 0511						
element	$\log\epsilon$(E)	ion	s24503 4500 K, −0.2, 6.0 km/s, [−0.5]			s25305 4550 K, −0.4, 6.0 km/s, [−0.5]		
			$\log\epsilon$(X)	n	δ	$\log\epsilon$(X)	n	δ
Li	3.31	Li I	1.04	1		0.96	1	
C	8.55	C I	9.23	5	0.11	9.31	5	0.17
O	8.87	O I	9.95	4	0.06	9.76	2	
Na	6.33	Na I	5.87	2		6.23	1	
Mg	7.58	Mg I	6.94	1		7.23	1	
Al	6.47	Al I	6.28	2		6.09	1	
Si	7.55	Si I	7.25	15	0.06	7.45	15	0.05
		Si II	7.67	1		7.50	1	
Ca	6.36	Ca I	6.07	5	0.13	5.84	6	0.07
Sc	3.17	Sc I	2.69	1		2.69	1	
		Sc II	2.50	2		2.39	6	0.10
Ti	5.02	Ti I	4.86	41	0.04	4.95	25	0.05
		Ti II	4.63	1		4.57	4	0.08
V	4.00	V I	3.58	21	0.06	3.56	24	0.06
		V II	3.43	3	0.08	3.25	3	0.04
Cr	5.67	Cr I	4.86	10	0.07	5.05	7	0.08
		Cr II	5.34	7	0.07	5.21	3	0.12
Mn	5.39	Mn I	4.61	8	0.15	4.87	6	0.12
Fe	7.50	Fe I	7.04	155	0.02	7.07	115	0.02
		Fe II	7.05	9	0.04	7.05	10	0.07
Co	4.92	Co I	4.46	16	0.05	4.49	5	0.10
Ni	6.25	Ni I	5.75	21	0.06	5.97	22	0.06
Cu	4.21	Cu I	3.18	1		3.51	2	
Zn	4.60	Zn I	4.32[2]	1		4.48[2]	2	
Y	2.24	Y I	1.72	3	0.22	1.54	2	
		Y II	1.57	5	0.10	1.32	6	0.08
Zr	2.60	Zr I	1.86	5	0.10	1.97	3	0.05
		Zr II	2.12	1		1.93	2	
Ba	2.13	Ba II	1.50[2]	3	0.19	1.85[2]	3	0.07
La	1.22	La II	0.65	3	0.19	0.61	3	0.18
Ce	1.55	Ce II	0.72	3	0.13	0.41	3	0.03
Pr	0.71	Pr II	0.13	1		−0.10	1	
Nd	1.50	Nd II	0.81	8	0.07	0.56	9	0.08
Eu	0.51	Eu II	0.28	3	0.16	0.11	2	

[1] In the table, n denotes the number of the lines used, and δ the error of the mean abundance derived using this number of lines. Atmospheric model parameters ($T_{\rm eff}$, $\log g$, ζ_t, [Fe/H]) are given under the spectrum number. The solar photospheric abundances were taken from [26]; we used the meteoritic abundance for lithium.

[2] The abundance of this element was determined from lines with equivalent widths $W > 250$ mÅ.

Table 4. Chemical composition $\log\epsilon(X)$ of BD + 18° 2757 and BD + 18° 2890[1]

Ion (X)	BD + 18° 2757						BD + 18° 2890		
	s23217			s23601			s23220		
	4850 K, 1.0, 2.3 km/s, [–2]			4850 K, 0.9, 2.2 km/s, [–2]			4790 K, 1.3, 1.2 km/s, [–1.5]		
	$\log\epsilon$ (X)	*n*	δ	$\log\epsilon$ (X)	*n*	δ	$\log\epsilon$ (X)	*n*	δ
Li I	1.00	1		0.70	1				
C I	7.62	7	0.10	7.78	1		8.17	8	0.12
O I	7.93	3	0.19				8.30	3	0.08
Na I	4.28	3	0.21	4.25	4	0.16	4.71	3	0.11
Mg I	5.83	5	0.19	5.76	3	0.06	6.36	5	0.08
Al I	4.96	4	0.11				5.06	1	
Si I	5.95	14	0.09	5.94	9	0.05	6.35	14	0.07
Si II	6.12	1		6.21	1		6.40	1	
K I	4.02	1							
Ca I	4.54	19	0.03	4.52	18	0.03	5.18	22	0.04
Sc II	1.00	12	0.08	0.99	12	0.04	1.47	9	0.07
Ti I	3.05	23	0.06	3.01	7	0.07	3.52	34	0.04
Ti II	3.01	13	0.06	3.04	6	0.08	3.69	9	0.07
V I	2.09	8	0.10	2.08	4	0.10	2.16	8	0.07
V II							2.67	1	
Cr I	3.53	10	0.12	3.37	7	0.08	3.95	10	0.06
Cr II	3.58	5	0.12	3.67	11	0.08	4.15	7	0.10
Mn I	3.06	5	0.22	2.78	4	0.16	3.78	5	0.13
Fe I	5.41	180	0.02	5.38	125	0.02	6.03	206	0.02
Fe II	5.39	17	0.02	5.41	15	0.04	6.00	15	0.05
Co I							3.66	9	0.07
Ni I	4.12	22	0.06	4.06	6	0.11	4.15	29	0.03
Cu I	1.54	2		1.70	2		2.19	3	0.12
Zn I	2.67	3	0.17	2.74	1		3.11	3	0.02
Y II	0.13	8	0.06	0.23	4	0.12	0.19	3	0.10
Zr I	0.92	4	0.17	1.12	4	0.16	1.14	2	
Zr II	0.64	3	0.11	0.77	2	0.10	0.86	1	
Ba II	0.08	3	0.07	0.01	3	0.08	0.69	3	0.05
La II	–0.40	3	0.02	–0.93	3	0.12	–0.06	2	
Ce II	–0.72	5	0.10	–0.90	4	0.04	–0.15	1	
Pr II	–1.29	1		–1.14	1		–0.60	1	
Nd II	–0.54	7	0.11	–0.56	8	0.08	–0.09	6	0.07
Eu II	–1.27	3	0.07	–1.37	3	0.17	–0.92	3	0.07

[1] In the table, *n* denotes the number of lines used, and δ the error of the mean abundance derived using this number of lines. Atmospheric model parameters ($T_{\rm eff}$, $\log g$, ζ_t, [Fe/H]) are given under the spectrum number.

3. DISCUSSION

3.1. Chemical Composition

Tables 3 and 4 list the elemental abundances $\log\epsilon(X) \pm \delta$ for the stars studied, averaged over the set of lines measured. The second column of Table 3 contains the corresponding data [26] for the solar atmosphere, which we have used to derive the abundances

$$[X/Fe] = (\log\epsilon(X) - \log\epsilon(Fe))_\star - (\log\epsilon(X) - \log\epsilon(Fe))_\odot,$$

required for analysis of the elemental-abundance curve. We will consider the elemental abundances of the stellar atmospheres in more detail below (Table 5).

BD + 18° 2890 and BD + 18° 2757. We have used the supergiants BD + 18° 2890 and BD + 18° 2757 as comparison objects, as stars whose luminosities and temperatures assign them to the upper part of the giant branch. However, their detailed chemical composition are also of special interest, since these very luminous stars are located at high Galactic latitudes (cf. Table 1) and they are relevant to the nature of UU Her-type stars [5, 27, 28].

Metallicities and abundances for a small group of chemical elements have been published for BD + 18° 2890 and BD + 18° 2757. Table 1 contains the metallicities estimated by Tautvaisiene [18] using photometric data in the Vilnius system. Based on high-resolution spectra (narrow intervals near the sodium lines), Pilachowski *et al.* [29] determined the metallicities and abundances of a number of light elements in the atmospheres of 60 low-metallicity evolved stars, including BD + 18° 2757 ($T_{\rm eff}$ = 4850 K, $\log g$ = 1.50, ξ_t = 1.5 km/s, [Fe/H] = –2.19) and BD + 18° 2890 ($T_{\rm eff}$ = 5000 K, $\log g$ = 2.20, ξ_t = 1.3 km/s, [Fe/H] = –1.58).

For comparison, Table 5 lists the results of Pilachowski *et al.* [29] together with our data. Our model parameters and metallicity for BD + 18° 2890 are in good agreement with those of [29]. The agreement for BD + 18° 2757 is somewhat worse. Note that the parameters of the stellar model atmospheres are determined using fundamentally different methods in the two studies. We have determined the parameters for each star individually, using a purely spectroscopic method (see above), whereas Pilachowski *et al.* [29] estimated the effective temperature from photometric indices, calculated the surface gravity assuming that the stellar masses are $0.8M_\odot$, and determined the microturbulence velocity based on the statistical dependence of this parameter on the effective temperature.

Table 4 presents our model parameters and elemental abundances for these supergiants, and Table 5 the elemental abundances relative to iron. We can see in Table 5 that the iron abundances for the stars derived in the two studies coincide within the systematic errors due to the different methods used to determine the model parameters. The abundances of magnesium and silicon are in good agreement, but the agreement is poorer for calcium, sodium, scandium, and nickel. We are inclined to consider our abundances of these elements to be more trustworthy, since they were obtained using a larger set of lines. This is supported, for example, by the fact that we derived a normal (close to solar) value for the [Ni/Fe] ratio for both stars, whereas Pilachowski *et al.* [29] found a deficiency of nickel for both these objects, whose origin was unclear.

We find considerable oxygen overabundances for both stars, by more than an order of magnitude. We used the lines of the IR triplet of oxygen near 7773 Å to calculate the oxygen abundances. The abundances of α-process elements in BD + 18° 2890 and BD + 18° 2757 correspond to those of low-metallicity, unevolved stars: we find a small excess of even elements (magnesium, silicon, and calcium), with no excess of sodium. The abundances of some s-process elements in BD + 18° 2890 and BD + 18° 2757 have been determined with low accuracy from a small set of very weak lines, but their mean abundance relative to iron is close to zero (on a relative scale). The barium abundance is most reliably determined from this group of elements. Hence, we can be confident that we have found no overabundances of *s*-process heavy metals.

Table 5. Relative elemental abundances $[X/Fe]_\odot$ in the stellar atmospheres

Element	IRAS 18123	BD + 18° 2757		BD + 18° 2890	
	this work	[29]	this work	[29]	this work
	$[Fe/H]_\odot$				
	–0.45	–2.19	–2.10	–1.58	–1.48
Li	–1.86		–0.36		
C	1.17		1.19		1.10
O	1.44		1.16		0.91
Na	0.12	–0.24	0.03	–0.27	–0.14
Mg	–0.04	0.32	0.32	0.33	0.26
Al	0.16		0.59		0.07
Si	0.36	0.45	0.50	0.39	0.28
K			1.00		
Ca	0.04	0.47	0.27	0.43	0.30
Sc	–0.14	0.18	–0.07	0.07	–0.22
Ti	0.18		0.11		0.18
V	–0.10		0.19		–0.36
Cr	–0.10		–0.02		–0.16
Mn	–0.20		–0.36		–0.13
Co	0.00				0.22
Ni	0.06	–0.32	–0.05	–0.22	–0.12
Cu	–0.26		–0.49		–0.54
Zn	0.25		0.18		–0.01
Y	–0.16		0.02		–0.57
Zr	–0.34		0.19		–0.07
Ba	0.00		0.01		0.04
La	–0.14		0.22		0.20
Ce	–0.53		–0.25		–0.22
Pr	–0.25		0.27		0.17
Nd	–0.36		0.05		–0.11
Eu	0.13		0.27		0.05

As a whole, the elemental abundances for BD + 18° 2890 and BD + 18° 2757 are consistent with their AGB status. Note that UU Her-type stars have a similar chemical composition. Thus, some characteristics of BD + 18° 2890 and BD + 18° 2757—namely their high absolute luminosities, positions in the Galaxy, and the peculiarities of their chemical composition—suggest that both supergiants are UU Her-type stars. However, neither star displays two attributes typical of stars of this type: an Hα emission component and characteristic variability.

IRAS 18123 + 0511. This object may be in a stage of intense mass exchange between the atmosphere and the circumstellar gas-dust envelope. Therefore, before analyzing the properties of chemical elements synthesized in various nuclear processes, we should determine the properties of elements that are to some degree subject to condensation processes. There are cases where the atmospheric abundance of an element depends on the temperature at which its atoms condense onto dust particles of the envelope; i.e., Fe, Mg, Si, and Ca may be considerably underabundant, while the CNO group elements, S, and Zn (which belongs to the iron group), which experience essentially no fractionation, have normal abundances [30]. If an appreciable fraction of iron nuclei have condensed onto dust particles, we will observe a deficiency of gas-phase iron nuclei in the stellar atmosphere. In this case, normalization of chemical abundances to the gas-phase iron content will result in relative excesses of elements that are less subject to condensation.

We can see a modest excess of zinc ([Zn/Fe] = + 0.25) in the atmosphere of IRAS 18123 + 0511 (Table 5). The zinc abundance, which does not change during nucleosynthesis in the interiors of low- and intermediate-mass stars, varies by the same amount as the iron abundance over a wide range of metallicities [31, 32]. Therefore, the inferred zinc excess does not depend on the scale (differential or absolute) on which it is obtained. Unfortunately, the zinc abundance for IRAS 18123 + 0511 is not completely certain, since we had to use strong zinc lines with equivalent widths exceeding 250 mÅ. We are therefore inclined to think that the inferred zinc excess has an instrumental/methodical origin, and that there is no fractionation in the circumstellar envelope of IRAS 18123 + 0511. This is supported by the normal (relative to the metallicity) abundance of calcium, which is reliably determined from a set of weaker lines. Hence, the obtained iron abundance, $[Fe/H]_\odot = -0.45$, reflects the actual metallicity of the atmosphere of IRAS 18123 + 0511.

Taking into account the errors, the abundances of the iron-group elements (scandium, vanadium, chromium, manganese, cobalt, nickel, copper) correspond to [Fe/H]. This is consistent with the properties of these elements over a wide range of metallicities [33]. For example, scandium and manganese are slightly underabundant relative to iron. Copper is also underabundant, in agreement with the conclusions of Sneden and Crocker [34] about the behavior of this element in stars with various metallicities.

The study of the detailed chemical composition of AGB stars is also interesting from the viewpoint of the lithium abundance: both theoretical predictions [35] and spectroscopic observations of AGB stars in the Magellanic Clouds [36, 37] suggest that relatively massive AGB stars are a source of Galactic lithium. The 6707-Å lithium doublet in the spectrum of IRAS 18123 + 0511 is measured rather accurately, and its average equivalent width W is 16 mÅ. However, the calculated lithium abundance, $\log\epsilon(\mathrm{Li}) \approx 1$, is extremely low; this may be associated with the destruction of lithium by convection.

Within the errors, the abundances of light elements (magnesium, sodium, aluminum) are consistent with the properties of these elements in unevolved stars of the same metallicity [32]. Note that the small sodium excess [Na/Fe] is probably due to neglect of deviations from LTE. For a luminous star with $T_{\mathrm{eff}} \approx 5000$ K and low metallicity, the corrections to the sodium abundance due to superionization reach 0.10–0.20 dex [38] for the subordinate lines (5682, 5688, 6154, 6160 Å) we have used. Hence, for this group of elements, also, we find no manifestations of nucleosynthesis and mixing.

The relative abundances of heavy metals (Y, Zr, Ba, La, Ce, Pr, Nd) are determined to low accuracy because of the limited set of lines used, but, on average, we can say that these metals are slightly underabundant relative to iron: [*s*/Fe] = –0.25. Thus, we have not found excesses of either lithium or s-process elements in IRAS 18123 + 0511. Consequently, there are no products of the third dredge-up in the atmosphere of IRAS 18123 + 0511. It is most probable that the lack of an excess of *s*-process elements is due to the fact that the time the star has spent on the AGB is insufficient to have carried the products of the third dredge-up to the surface. This is consistent with the earlier conclusion of Garcĭa-Lario *et al.* [40] for a sample of Galactic AGB stars with powerful envelopes.

We determined the carbon abundance, [C/Fe] = 1.17, from five weak lines of CI. To calculate the oxygen abundance ([O/Fe] = 1.44), we used the reliably measured lines of the oxygen IR triplet. The oxygen abundance is fairly realistically determined in the approximation of LTE: Gratton *et al.* [38] showed that non-LTE corrections for the lines of the oxygen IR triplet are insignificant in cool supergiants. We emphasize that the ratio O/C > 1 we have obtained is consistent with the overabundance of oxygen; this follows from the fact that the object is an OH/IR star. The ratio O/C > 1 also agrees with the presence of an IR silicate emission feature at 9.7 μm, which is characteristic of oxygen-rich AGB stars [39].

As a whole, the elemental abundances in the atmosphere of IRAS 18123 + 0511 are consistent with the idea that it is a relatively massive star at an early stage of its AGB evolution.

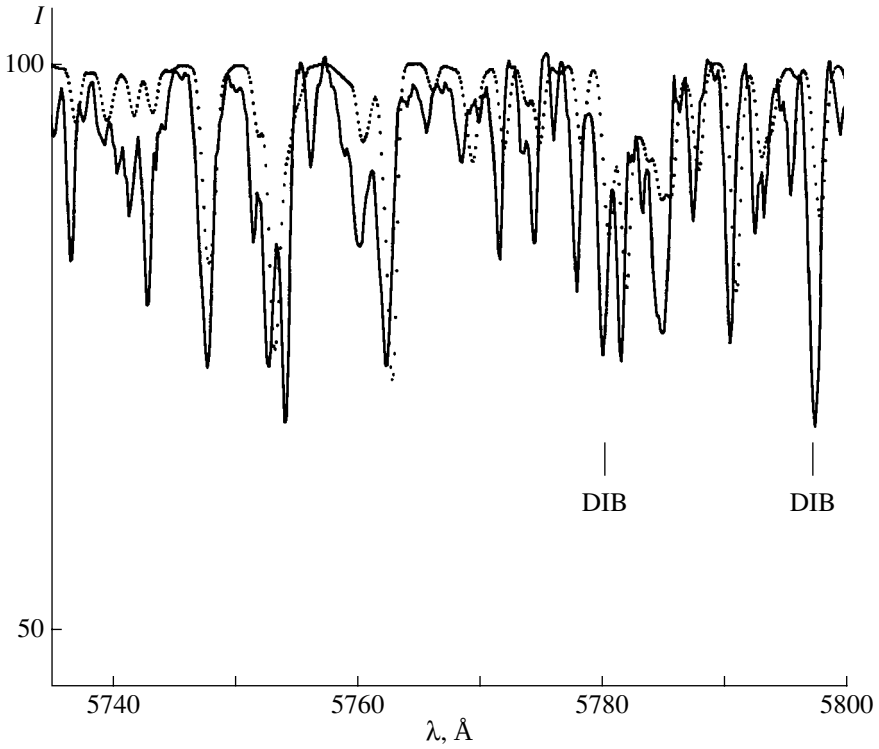

Fig. 3. Comparison of the theoretical (points) and observed (solid curve) spectra of IRAS 18123 + 0511 in the wavelength range containing the 5780- and 5797-Å bands.

3.2. Radial Velocities

Table 2 presents the results of radial-velocity measurements for individual spectrograms. We first selected unblended lines (300–500 lines in each spectrogram) by comparing the observed spectrum with the corresponding synthetic spectrum. We found the zero-point of each spectrogram using the standard procedure, by referencing to night-sky ionospheric emission features and the telluric absorption spectrum. When the number of lines exceeds 200, the typical error of the mean δ is 0.2 km/s for measurements of a single line, σ = 2.4 km/s for stars with a strong metal deficiency, and σ = 3.5 km/s for IRAS 18123 + 0511, where blending is higher due to the presence of numerous strong lines.

The radial velocities of BD + 18° 2757 and BD + 18° 2890 are of no special interest in the context of this paper. Note that variability of the radial velocities of these stars was established in [41]. Later, Bartkevicius and Sperauskas [42] measured radial velocities for a sample of halo stars using a photoelectric radial-velocity meter on the 1-m telescope on Mt. Maĭdanak. They found that the velocity for BD + 18° 2757 varied from –31.23 to –15.17 km/s, and that for BD + 18° 2890 from –33.12 to –17.71 km/s; these values far exceed the measurement errors. Our data for a very different epoch confirm the variability of V_r for both these objects.

Let us consider the radial-velocity measurements for IRAS 18123 + 0511 in more detail. The mean value V_r = 78.0 km/s derived from metallic lines, which we can take to be the systemic velocity, is in good agreement for the three observation times, indicating that the radial velocity of IRAS 18123 + 0511 is constant. The data of Table 2 show that, within the above errors, the mean velocity derived from metallic lines for all observation times is in good agreement with the velocity V_r determined for the center of the Hα profile.

3.3. Absorption Features Identified with Diffuse Interstellar Bands

We found several absorption features in the spectrum of IRAS 18123 + 0511, whose positions identify them with well-known diffuse interstellar bands (DIB). Figure 3 shows the part of the spectrum containing the strongest diffuse band, together with a synthetic spectrum we calculated using the STARSP software [25] for models with the parameters and chemical composition determined for IRAS 18123 + 0511. We can see from this figure that the calculated photospheric spectrum does not fit the observed spectrum in this wavelength range, which is filled with diffuse bands. The vertical lines in Fig. 3 mark the strongest known diffuse bands in this wavelength interval, 5780 and 5797 Å [43]. The mean radial velocities measured from 5–7 such features in each spectrum of IRAS 18123 + 0511 coincide within the errors with the velocity of one of the components observed in the D1, D2 sodium doublet lines

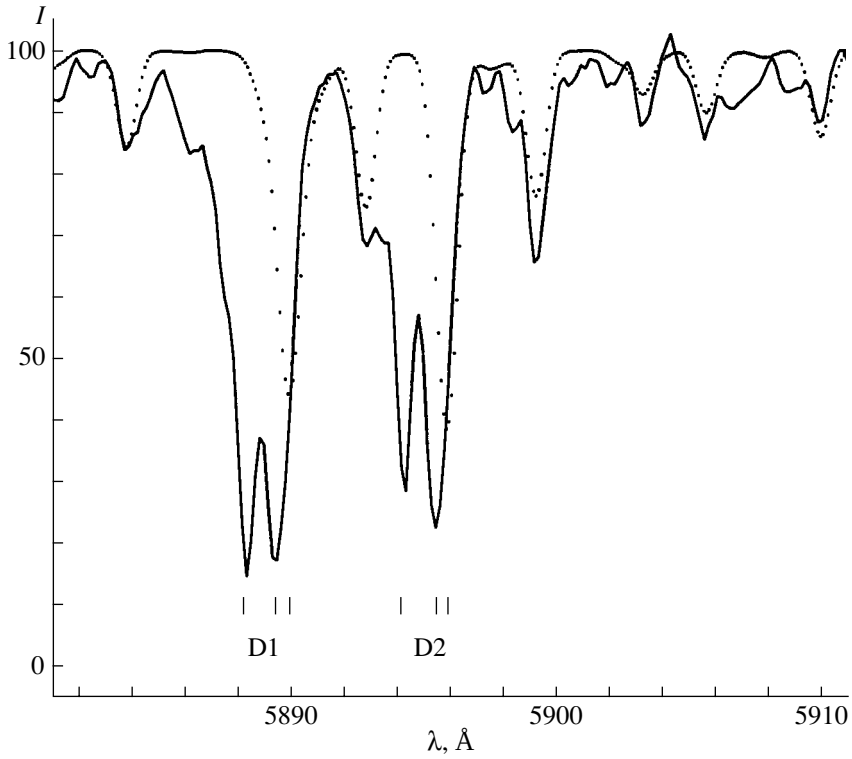

Fig. 4. Same as Fig. 2, but in the wavelength range containing the sodium doublet. The position of the stellar component of each doublet line coincides with the position of this line in the synthetic spectrum.

(Table 2). Figure 4 shows that the complex structures of the D1, D2 sodium doublet lines contain stellar, interstellar, and circumstellar components.

When corrected for the motion toward the apex, $\Delta V_{\rm apex} = 19.6$ km/s, the velocity found from the interstellar component of the sodium doublet lines, $V_{\rm IS} = -4.1$ km/s, is consistent with the results of Munch [44] for this direction in the Galaxy. The difference of the radial velocities measured from photospheric and circumstellar lines in the spectrum of IRAS 18123 + 0511 yields the envelope expansion velocity $V_{\rm exp} \approx 21$ km/s. Unfortunately, we cannot compare the radial velocity of IRAS 18123 + 0511 and the expansion velocity of its envelope with the radio data, since Eder *et al.* [14] measured an unusual single-peaked 1612-MHz profile. While most OH/IR stars have a double-peaked OH profile, produced by the expanding envelope, the profile of IRAS 18123 + 0511 contains only one broad feature with mean velocity $V_{LSR} = 85.0$ km/s. Note, however, that our envelope expansion velocity, $V_{\rm exp} \approx 21$ km/s, is in good agreement with the statistical mean for OH/IR stars at high Galactic latitudes ($|b| > 6°$) [14].

Diffuse interstellar bands have been found earlier in the spectra of several evolved stars. Cohen and Jones [45] detected diffuse interstellar bands in the spectrum of the strongly reddened nucleus of a planetary nebula (WC11, IRAS 21282 + 5050). In their study of a sample of stars showing signs of mass loss, Le Bertre and Lequeux [46], found interstellar bands in the spectra of IRC + 10420 and AC Her. We have likewise found circumstellar absorption in the spectra of several cool post-AGB objects in our PPN sample: IRAS 04296 + 3429 [8], IRAS 23304 + 6147 [9], and RAFGL 2688 [10]. The very fact that the spectra of some high-latitude post-AGB stars contain diffuse bands suggests they have a circumstellar nature. The circumstellar origin of the DIB absorption in the spectrum of IRAS 18123 + 0511 is especially obvious, since the object is located fairly high above the Galactic plane, $b = 11°$. Additional evidence for this is provided by a comparison of the radial velocities derived from these bands and from atmospheric absorption lines (Table 2).

4. CONCLUSIONS

We have reported spectroscopic results for three AGB stars, and studied for the first time the optical spectrum of the OH/IR star IRAS 18123 + 0511. We have determined model parameters, calculated detailed chemical compositions, and measured radial velocities using various spectral features. The deficiency of iron we find in the atmosphere of IRAS 18123 + 0511, $[{\rm Fe/H}_\odot] = -0.45$, is real, since fractionation in the circumstellar envelope is not efficient. As a whole, the elemental abundances are consistent with those expected for the AGB stage. In combination with the radial velocity and Galactic latitude of the object, its metallic-

ity suggests that it belongs to the old disk population of the Galaxy. We determined the envelope expansion velocity to be $V_{exp} \approx 21$ km/s, based on the positions of absorption bands formed in the circumstellar envelope.

The parameters of the high-latitude supergiants BD + 18° 2890 and BD + 18° 2757 (high absolute luminosity, position in the Galaxy, and chemical-composition peculiarities) suggest they should probably be classified as UU Her-type stars.

ACKNOWLEDGMENTS

This research used the SIMBAD astronomical database and ADS bibliographic database. The program of spectroscopic studies of objects evolving from AGB stars to planetary nebulae using the 6-m telescope is supported by the Russian Foundation for Basic Research (project code 99-02-18339) and the State Science and Technology Program in Astronomy (projects 1.4.1.1. and 2.1.5.5).

REFERENCES

1. V. G. Klochkova, Mon. Not. R. Astron. Soc. **272**, 710 (1995).
2. L. Zacs, V. G. Klochkova, and V. E. Panchuk, Mon. Not. R. Astron. Soc. **275**, 764 (1995).
3. V. G. Klochkova and V. E. Panchuk, Bull. Spec. Astrophys. Obs. **41**, 5 (1996).
4. L. Zacs, V. G. Klochkova, V. E. Panchuk, and R. Spelmanis, Mon. Not. R. Astron. Soc. **282**, 1171 (1996).
5. V. G. Klochkova, E. L. Chentsov, and V. E. Panchuk, Astron. Astrophys. **323**, 789 (1997).
6. V. G. Klochkova, E. L. Chentsov, and V. E. Panchuk, Mon. Not. R. Astron. Soc. **292**, 19 (1997).
7. V. G. Klochkova, Bull. Spec. Astrophys. Obs. **44**, 5 (1998).
8. V. G. Klochkova, R. Szczerba, V. E. Panchuk, and K. Volk, Astron. Astrophys. **345**, 905 (1999).
9. V. G. Klochkova, R. Szczerba, and V. E. Panchuk, Pis'ma Astron. Zh. **26**, 115 (2000) [Astron. Lett. **26**, 88 (2000)].
10. V. G. Klochkova, R. Szczerba, and V. E. Panchuk, Pis'ma Astron. Zh. **26**, 510 (2000) [Astron. Lett. **26**, 439 (2000)].
11. B. M. Lewis, Astrophys. J. **338**, 234 (1989).
12. K. V. K. Iyengar and M. Parthasarathy, Astron. Astrophys., Suppl. Ser. **121**, 45 (1997).
13. V. E. C. J. van der Veen and H. J. Habing, Astron. Astrophys. **194**, 125 (1988).
14. J. Eder, B. M. Lewis, and Y. Terzian, Astrophys. J., Suppl. Ser. **66**, 183 (1988).
15. D. Engels and B. M. Lewis, Astron. Astrophys., Suppl. Ser. **116**, 117 (1996).
16. B. M. Lewis, Astrophys. J. **533**, 959 (2000).
17. A. Bartkevicius, Byull. Vil'nyus. Astron. Obs., No. 66, 3 (1984).
18. G. Tautvaisiene, Byull. Vil'nyus. Astron. Obs., No. 78, 3 (1984).
19. V. E. Panchuk, I. D. Najdenov, V. G. Klochkova, *et al.*, Bull. Spec. Astrophys. Obs. **44**, 127 (1998).
20. V. E. Panchuk, V. G. Klochkova, I. D. Naĭdenov, *et al.*, Preprint No. 139, Spets. Astrofiz. Obs. (Special Astrophysical Observatory, 1999).
21. G. A. Galazutdinov, Preprint No. 92, Spets. Astrofiz. Obs. (Special Astrophysical Observatory, 1992).
22. B. Gustafsson, R. A. Bell, K. Eriksson, and Å. Nordlund, Astron. Astrophys. **42**, 407 (1975).
23. E. J. Bakker, E. F. van Dishoeck, L. B. F. M. Waters, and T. Schoenmaker, Astron. Astrophys. **323**, 469 (1997).
24. V. G. Klochkova and V. E. Panchuk, Pis'ma Astron. Zh. **24**, 754 (1998) [Astron. Lett. **24**, 650 (1998)].
25. V. Tsymbal, in *Model Atmospheres and Spectrum Synthesis*, Ed. by S. J. Adelman, F. Kupka, and W. W. Weiss; Astron. Soc. Pac. Conf. Ser. **108**, 198 (1996).
26. N. Grevesse, A. Noels, and A. J. Sauval, Astron. Soc. Pac. Conf. Ser. **99**, 117 (1996).
27. D. Sasselov, Astrophys. Space Sci. **102**, 161 (1984).
28. V. G. Klochkova and V. E. Panchuk, Pis'ma Astron. Zh. **14**, 933 (1988) [Sov. Astron. Lett. **14**, 395 (1988)].
29. C. A. Pilachowski, C. Sneden, and R. P. Kraft, Astron. J. **111**, 1689 (1996).
30. H. Bond, Nature **356**, 474 (1992).
31. J. C. Wheeler, C. Sneden, and J. W. Truran, Annu. Rev. Astron. Astrophys. **27**, 279 (1989).
32. F. X. Timmes, S. E. Woosley, and T. Weaver, Astrophys. J., Suppl. Ser. **98**, 617 (1995).
33. A. McWiliam, Annu. Rev. Astron. Astrophys. **35**, 503 (1997).
34. C. Sneden and D. A. Crocker, Astrophys. J. **335**, 406 (1988).
35. A. G. W. Cameron and W. A. Fowler, Astrophys. J. **164**, 111 (1971).
36. V. V. Smith and D. L. Lambert, Astrophys. J. Lett. **361**, L69 (1990).
37. V. V. Smith, B. Plez, and D. L. Lambert, Astrophys. J. **441**, 735 (1995).
38. R. G. Gratton, E. Caretta, K. Eriksson, and B. Gustaffsson, Astron. Astrophys. **350**, 955 (1999).
39. S. Kwok, Annu. Rev. Astron. Astrophys. **31**, 63 (1993).
40. P. García-Lario, F. D'Antona, J. Lub, *et al.*, in *Asymptotic Giant Branch Stars (IAU Symposium 191)*, Ed. by T. Le Bertre, A. Lebre, and C. Waelkens, 1999, p. 91.
41. B. W. Carney and D. W. Latham, Astron. J. **92**, 60 (1986).
42. A. Bartkevičius and J. Sperauskas, Balt. Astron. **3**, 49 (1994).
43. P. Jenniskens and F.-X. Desért, Astron. Astrophys., Suppl. Ser. **106**, 39 (1994).
44. G. Munch, Astrophys. J. **125**, 42 (1957).
45. M. Cohen and B. F. Jones, Astrophys. J. Lett. **321**, L151 (1987).
46. T. Le Bertre and J. Lequeux, Astron. Astrophys. **274**, 909 (1993).

Translated by G. Rudnitskiĭ

Astronomy Reports, Vol. 45, No. 7, 2001, pp. 564–568. Translated from Astronomicheskiĭ Zhurnal, Vol. 78, No. 7, 2001, pp. 655–660.

A New Approach to Modeling the Surface Magnetic Fields of Chemically Peculiar Stars

V. R. Khalak[1], Yu. N. Khalak[2], A. V. Shavrina[1], and N. S. Polosukhina[3]

[1]*Main Astronomical Observatory, National Academy of Sciences of Ukraine, Goloseevo, Kiev, 252127 Ukraine*

[2]*Bogolyubov Institute of Theoretical Physics, Kiev, Ukraine*

[3]*Crimean Astrophysical Observatory, National Academy of Sciences of Ukraine, Nauchnyĭ, Crimea, 334413 Ukraine*

Received July 26, 2000

Abstract—A reconstruction of the line-of-sight component and modulus of the surface-magnetic-field vector is proposed, using a model with artificial point sources of the magnetic field with "virtual" magnetic charges in the body of a star. This approach for the direct calculation of the field from the superposition of the potentials of individual magnetic charges enables the reconstruction of most possible configurations of the surface magnetic field of a star. Proper choice of the axis orientations for the three coordinate systems used makes it possible to obtain a simple representation for the vector components of the surface magnetic field. In a dipole approximation, the expression for the line-of-sight component of the magnetic field averaged over the visible disk of the star reduces to the form obtained in other studies. © *2001 MAIK "Nauka/Interperiodica".*

1. INTRODUCTION

A detailed investigation into the spectra of chemically peculiar stars and analyses of the distribution of chemical elements over their surfaces require a comprehensive consideration of all processes contributing to the broadening of observed spectral lines. In the case of magnetic chemically peculiar stars, magnetic broadening of spectral lines due to the Zeeman or, for strong fields, the Paschen–Bach effect deserves particular attention. To take into account magnetic line broadening, we must know the modulus of the surface magnetic field averaged over the visible disk of the star and the angle between the magnetic-field vector and the line of sight. These quantities vary with the phase of the axial rotation of the star, so that an appropriate model for the structure of the surface magnetic field of the star must be constructed.

Most of our knowledge of the surface magnetic fields of chemically peculiar stars has been inferred from observations of variations in the line-of-site magnetic field component with the rotational phase of the star. At present, magnetic fields have been reliably detected for more than 150 chemically peculiar stars [1], and they play an important role in evolutionary processes in stars of this type. The results of early measurements of the magnetic fields on chemically peculiar stars can be found in [2, 3]. Later, the use of new instruments and modern techniques enabled measurements of the line-of-sight component of the field [4–6] and the modulus of the surface field [7] to high accuracy (by current standards) for more than 40 chemically peculiar stars.

Modeling of the magnetic-field structure of chemically peculiar stars was originally based on models with an oblique rotator and a centered dipole field [8], taking into account only the dipole moment of the system. In most cases, this simplified approach yielded a relatively good description of the observed averaged (in most cases, over the stellar disk) line-of-sight component $\langle B_z \rangle$ of the magnetic field as a function of the rotational phase of the oblique rotator. However, a more detailed analysis of the available $\langle B_z \rangle$ measurements for chemically peculiar stars indicated that these data can by no means always be well fit by such models. The sinusoidal rotational-phase dependence of $\langle B_z \rangle$ predicted by models with an exactly centered dipole leads to substantial discrepancies with the observational data in some cases [9]. A model with an off-centered magnetic dipole was invoked in an attempt to remove these discrepancies [10], but this model was likewise unable to describe the entire collection of observational data.

Over the past five years, a series of studies by Landolfi *et al.* [11] and Bagnulo *et al.* [12, 13] have used higher order (dipole, quadrupole, etc.) moments of the magnetic field to account for specific features of nonsinusoidal variations in the line-of-sight component $\langle B_z \rangle$ of the field with the rotational phase of a star as an oblique rotator. This approach provides a fairly good description of the observed character of the $\langle B_z \rangle$ variations in most chemically peculiar stars [13]. However, the octupole magnetic moment must be taken into account in some cases, substantially increasing the number of free model parameters and lowering the accuracy with which they are determined.

Gerth *et al.* [14, 15] proposed an alternative model for the structure of the surface field, which we consider in detail in the following section.

1063-7729/01/4507-0564$21.00 © 2001 MAIK "Nauka/Interperiodica"

2. THE APPROACH

Magnetic fields originate physically in the interior of the star. According to the Maxwell equations, magnetic field lines are circularly closed ($\mathrm{div}\,\mathbf{B} = 0$). They thread the body of the star and go outward into circumstellar space, forming a certain magnetic-field configuration on the surface of the star (Fig. 1). The principal task is to describe the surface field's structure as fully as possible in the framework of a particular model. Gerth *et al.* [14, 15] suggested considering a system of spatially separated *point field sources* with virtual magnetic charges. Although there is no evidence for the existence of isolated magnetic charges in nature, we can introduce such charges artificially and place them within a certain volume D in the body of the star (Fig. 1). Since the number of magnetic-field sources under consideration is obviously grater than unity, we create a system of several magnetic dipoles (or one dipole). Because of the discontinuity of the magnetic-field lines in the region where the virtual magnetic charges are located and the presence of a system of currents generating the actual stellar magnetic field in the region D, the modeling of the field structure is correct only outside this volume (Fig. 1). We assume that there are no virtual magnetic charges and current system outside the volume D; accordingly, the Maxwell equations $\oint \mathrm{div}\,\mathbf{B}\,d\mathbf{S} = 0$ and $\oint \mathrm{curl}\,\mathbf{H}\,d\mathbf{l} = 0$ are satisfied there. Thus, to model the surface magnetic field of the star, we should place an artificial system of point field sources within the star's body, such that the volume D is fully contained within the star.

Each point source, for example the jth, is characterized by some virtual magnetic charge Q_j and produces a field with the corresponding potential $U_j = Q_j/|\mathbf{r}_j|$ at an arbitrary point M of the stellar surface a distance $|\mathbf{r}_j|$ from the source (Fig. 1). By analogy with electric fields, we take a virtual magnetic charge to be positive if its magnetic-field lines diverge and negative if they converge. At this point on the stellar surface, the system of point sources produces a magnetic field whose potential is equal to the sum of the potentials due to the individual sources:

$$U = \sum_j U_j = \sum_j Q_j/|\mathbf{r}_j|. \qquad (1)$$

It is important that, in order for the magnetic flux through the stellar surface to be zero ($\oint \mathbf{B}\,d\mathbf{S} = 0$), the sum of the virtual magnetic charges for the system of point field sources must be zero:

$$\sum_j Q_j = 0. \qquad (2)$$

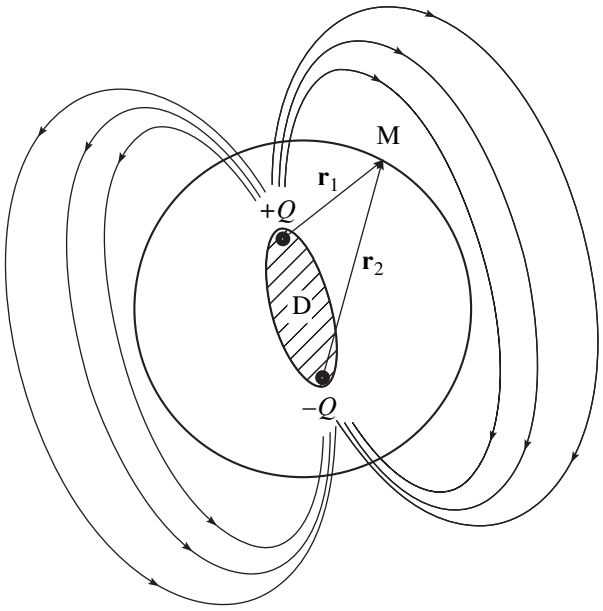

Fig. 1. System of point sources of magnetic field constructed artificially in the body of a star to model the structure of the surface magnetic field.

Accordingly, the total magnetic-field vector at a given point M can be determined in terms of the gradient of the field potential:

$$\mathbf{B} = -\nabla U = \sum_j \frac{Q_j}{|\mathbf{r}_j|^3}\mathbf{r}_j. \qquad (3)$$

It follows from [2, 4, 6] that, by and large, the character and amplitude of variations in the line-of-sight component of the surface magnetic field in chemically peculiar stars have been constant over the 40-year observation period. Thus, it is logical to suppose that we are dealing with long-lived magnetic fields, whose structure does not change significantly over such intervals.

3. MODELING TECHNIQUE

For simplicity, we consider an oblique rotator with only one (test) point magnetic-field source inside a star, using three different coordinate systems (see Fig. 2). All observational data for the surface magnetic field of the star are referenced, in one way or another, to the direction towards the observer. For this reason, it is convenient to use for the first coordinate system a *right-handed Cartesian (RHC) system* (x, y, z) with its origin at the star's center (point C) and one axis (for instance, the z axis) directed toward the observer, i.e., along the line of sight. The z axis intersects the surface of the star of radius $R_\star$ at the *subsolar* point Z. Let the x axis be directed toward the *northern celestial pole* and the

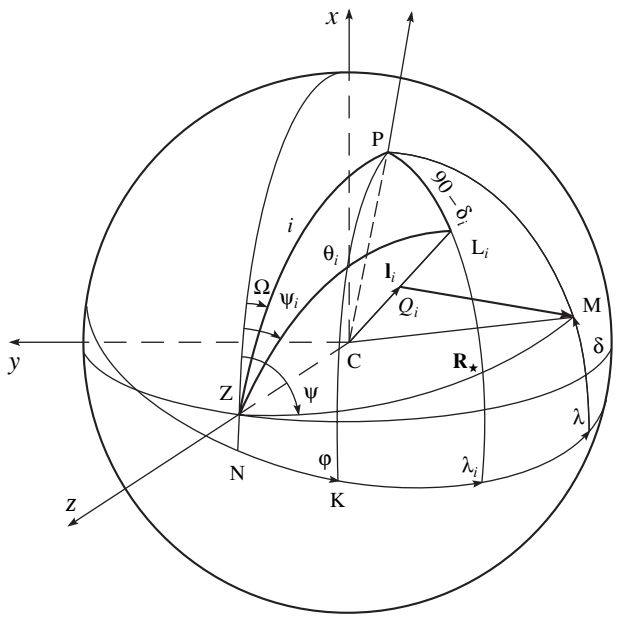

Fig. 2. Geometry of the oblique-rotator model with one test point source of magnetic field.

direction of the *y* axis be such that the coordinate system is right-handed (Fig. 2). Since we wish to model the structure of the surface magnetic field, it is convenient to choose a spherical coordinate system (R, θ, ψ) fixed to an Earth-based observer (SO) as the second coordinate system. The spherical and Cartesian coordinates (x, y, z) are related as follows:

$$\begin{cases} x = R\sin\theta\cos\psi \\ y = -R\sin\theta\sin\psi \\ z = R\cos\theta. \end{cases} \tag{4}$$

Thus, the position of an arbitrary point M on the stellar surface ($R = R_\star$) is specified in the SO system by a latitude θ ($0° < \theta < 180°$) and a longitude ψ ($0° < \psi < 360°$), measured counterclockwise from the central meridian (Fig. 2). Accordingly, the star's *positive rotational pole* P (about which, by definition, the star rotates counterclockwise, viewed from above) is specified by the *inclination i of the rotational axis to the line of sight* and by the *position angle* Ω.

As the third coordinate system, it is convenient to use a spherical coordinate system (R, δ, λ) fixed to the star (SS), with its origin at the star's center (point C). At some initial time in the star's rotation ($\varphi = 0$), when the line-of-sight component of the magnetic field $\langle B_z \rangle$ is minimum, the great-circle arc connecting the point P with the subsolar point Z (and intersecting the stellar equator at a point N) coincides with the *zero meridian*. In the SO coordinate system, an arbitrary point M on the surface $R = R_\star$ is specified by a latitude δ ($-90° < \delta < 90°$) and a longitude λ ($0° < \lambda < 360°$), measured counterclockwise from the zero meridian (Fig. 2). As the star rotates, the zero meridian moves in the direction of increasing longitude, and its position is given by the *phase angle* φ.

Let the test point source of magnetic field be at a point Q_j a distance l_j from the center of the star. Its projection along vector $\mathbf{l}_j$ onto the surface of the star is a point L_j with coordinates (θ_j, ψ_j) in the SO system and (δ_j, λ_j) in the SS system. We can then derive from the spherical triangle ZPL_j, given the angles Ω and i, the following relationship between the two spherical coordinate systems (omitting the subscript j):

$$\begin{cases} \cos\theta = \sin\delta\cos i + \cos\delta\sin i\cos(\varphi + \lambda) \\ \sin\theta = \sqrt{1 - \cos^2\theta}; \end{cases} \tag{5}$$

$$\begin{cases} \cos(\psi - \Omega) = \dfrac{\sin\delta - \cos i\cos\theta}{\sin\theta\sin i} \\ \sin(\psi - \Omega) = \cos\delta\dfrac{\sin(\varphi + \lambda)}{\sin\theta}. \end{cases} \tag{6}$$

Using well-known geometrical formulas and (6), we obtain for the angle ψ:

$$\begin{cases} \sin\psi = \cos\Omega\sin(\psi - \Omega) + \sin\Omega\cos(\psi - \Omega) \\ \cos\psi = \cos\Omega\cos(\psi - \Omega) - \sin\Omega\sin(\psi - \Omega). \end{cases} \tag{7}$$

The distance between the test point magnetic-field source Q_j and an arbitrary surface point M is determined by the relationship $|\mathbf{r}_j| = |\mathbf{R}_\star - \mathbf{l}_j|$ and, in the SO coordinate system, is equal to

$$|\mathbf{r}_j| = R_\star\sqrt{1 + a_j^2 - 2a_j(\sin\theta\sin\theta_j\cos(\psi - \psi_j) + \cos\theta\cos\theta_j)}, \tag{8}$$

[see (4)]; here, $a_j = l_j/R_\star$ is the distance from the point source to the center of the star in units of the stellar radius.

Consequently, using (4) and (8), the projections of the vector **B** [see (3)] onto the axes of the RHC coordinate system at an arbitrary point M on the surface $R = R_\star$ can be written

$$\begin{cases} B_x = R_\star \sum\limits_j \dfrac{Q_j}{|\mathbf{r}_j|^3}(\sin\theta\cos\psi - a_j\sin\theta_j\cos\psi_j) \\ B_y = -R_\star \sum\limits_j \dfrac{Q_j}{|\mathbf{r}_j|^3}(\sin\theta\sin\psi - a_j\sin\theta_j\sin\psi_j) \\ B_z = R_\star \sum\limits_j \dfrac{Q_j}{|\mathbf{r}_j|^3}(\cos\theta - a_j\cos\theta_j). \end{cases} \tag{9}$$

Adopting a limb-darkening law for the star of the form $1 - u + u\cos\theta$ (where $0 \le u \le 1$) and averaging B_z over the visible hemisphere of the star in accordance with [11], we obtain the following theoretical expression for the observed line-of-sight component of the surface field:

$$\langle B_z\rangle = \frac{3}{\pi(3-u)R_\star^2}\sum_j Q_j \int_0^{2\pi} d\psi \int_0^{\pi/2} \frac{\sin\theta\cos\theta(1-u+u\cos\theta)(\cos\theta - a_j\cos\theta_j)d\theta}{[1 + a_j^2 - 2a_j(\sin\theta\sin\theta_j\cos(\psi-\psi_j) + \cos\theta\cos\theta_j)]^{\frac{3}{2}}}. \tag{10}$$

Accordingly, the *modulus of the surface magnetic-field* at the point M is $|\mathbf{B}| = \sqrt{B_x^2 + B_y^2 + B_z^2}$, and, after averaging over the visible hemisphere of the star, we obtain

$$\langle|\mathbf{B}|\rangle = \frac{3}{\pi(3-u)}\int_0^{2\pi} d\psi \int_0^{\pi/2} \sin\theta\cos\theta(1-u+u\cos\theta) \times \sqrt{B_x^2 + B_y^2 + B_z^2}\, d\theta. \tag{11}$$

We do not write here the full expression for $\langle|\mathbf{B}|\rangle$, which is cumbersome.

For an artificially introduced system of two point magnetic-field sources (a magnetic dipole), in view of condition (2), the proposed model will have the following 11 free parameters:

$$\begin{cases} Q, R_\star \\ 0 \le a_1, a_2 < 1 \\ 0 \le u \le 1 \\ 0^\circ \le i \le 180^\circ \\ 0^\circ \le \lambda_1, \lambda_2, \Omega < 360^\circ \\ -90^\circ \le \delta_1, \delta_2 \le 90^\circ. \end{cases} \tag{12}$$

Two (Ω, i) specify the position of the rotational axis of the star with respect to the observer, two (u, $R_\star$) characterize the star itself, and the remaining seven specify the virtual charge and the positions of the point sources of field in the body of the star. Varying the free model parameters within the above limits, we can find the best fit of the model parameters for the surface magnetic field to the observational data [13, 16].

In contrast to the model of Gerth *et al.* [14, 15], we have searched for the projections of the **B** vector onto the axes of the RHC coordinate system, one of which (the z axis) is directed toward the observer. Our choice of the orientations of all three coordinates systems enable us to obtain a simpler form (9) for the components of the **B** vector, with the transformation from the coordinates (δ_j, λ_j) to the coordinates (θ_j, ψ_j) taken into account in advance via (5)–(7).

4. THE CENTERED-SYMMETRIC-DIPOLE APPROXIMATION

For a symmetric magnetic dipole situated at the center of a star of radius $R_\star$ with limb-darkening coefficient u, we have the following relations between the free model parameters:

$$a_1 = a_2 = a \ll 1; \quad Q_1 = -Q_2 = Q;$$
$$\delta_1 = -\delta_2 = \delta; \quad \lambda_1 = \lambda; \quad \lambda_2 = 180^\circ + \lambda_1.$$

As noted in [11], for a symmetric dipole, $\langle B_z\rangle$ does not depend on the position angle Ω. Therefore, without loss of generality, we can assume in subsequent calculations that $\Omega = 0^\circ$. Following Hensberge *et al.* [10], we will use the angle $\beta = 90^\circ - \delta$ between the magnetic-dipole axis and the rotational axis of the star. Thus, according to (9), the line-of-sight (z) component of the magnetic field at an arbitrary surface point M(θ, ψ) is

$$B_z \propto \left\{ \frac{\cos\theta - aZ}{[1 + a^2 - 2a(A\sin\theta + Z\cos\theta)]^{\frac{3}{2}}} \right.$$

$$-\frac{\cos\theta + aZ}{[1 + a^2 + 2a(A\sin\theta + Z\cos\theta)]^{\frac{3}{2}}}\Bigg\},$$

where $A = X\cos\psi + Y\sin\psi$, and

$$\begin{cases} X = \cos\beta\sin i - \sin\beta\cos i\cos(\varphi + \lambda) \\ Y = \sin\beta\sin(\varphi + \lambda) \\ Z = \cos\beta\cos i + \sin\beta\sin i\cos(\varphi + \lambda). \end{cases} \quad (13)$$

Since $a \ll 1$, the resulting expression for B_z can be expanded in a Maclaurin series in the small parameter a. If only the first term of the expansion is retained, we obtain

$$B_z \propto 2a[Z(3\cos^2\theta - 1) + 3A\sin\theta\cos\theta].$$

Then, averaging over the visible disk of the star [see (10)], we find

$$\langle B_z\rangle \sim \frac{15 + u}{20(3 - u)}Z. \quad (14)$$

The form of this expression coincides with that given in [10] for the line-of-sight component of the magnetic field in the case of a centered symmetric dipole. In fact, as we can easily see from (13) and Fig. 2, we have $Z = \cos\alpha$, where α is the inclination of the magnetic-dipole axis to the line of sight. Thus, the case of a centered symmetric magnetic dipole represents one particular realization of our model that leads to results described earlier by other authors [10].

5. CONCLUSION

The model proposed here to describe various stellar surface magnetic-field structures, based on an artificially constructed system of point field sources in the body of the star is a modification of the approach developed in [14, 15]. Our choice of the orientations of the three coordinate systems used made it possible to obtain a simpler expression for the components of the vector **B** in the RHC coordinate system [see (9)].

Point sources of magnetic field do not exist in nature. We introduced them into our model artificially in order to obtain the best description of the observed configurations of the surface magnetic field using a minimum number of free model parameters. Therefore, the estimate of the magnetic-field strength yielded from our modeling will agree with the real value only outside the volume confining the system of point field sources (Fig. 1).

Applying the model to the particular case of a centered symmetric dipole reproduces the results for the line-of-sight component of the surface magnetic field obtained earlier in other studies [10].

Thus, the model proposed here can be used to describe any observed surface-magnetic-field configuration with high accuracy as a superposition of the fields of the required number of point field sources whose sum of virtual magnetic charges is equal to zero. One advantage of this approach is that it allows for an arbitrary distribution of point field sources in the body of the star, and its applicability is restricted only by the number of such sources.

ACKNOWLEDGMENTS

V. Khalak is grateful to the Ukrainian Astronomical Association for financial support and to S. Plachinda for consultation and valuable recommendations.

REFERENCES

1. I. I. Romanyuk, in *Stellar Magnetic Fields*, Ed. by Y. V. Glagolevskij and I. I. Romanyuk (Special Astrophys. Observ. Press, Moscow, 1997), p. 11.
2. H. W. Babcock, Astrophys. J., Suppl. Ser. **99**, 135 (1958).
3. E. F. Borra and J. D. Landstreet, Astrophys. J., Suppl. Ser. **42**, 421 (1980).
4. G. Mathys, Astron. Astrophys., Suppl. Ser. **89**, 121 (1991).
5. G. Mathys, Astron. Astrophys., Suppl. Ser. **108**, 547 (1994).
6. G. Mathys and S. Hubrig, Astron. Astrophys., Suppl. Ser. **124**, 475 (1997).
7. G. Mathys and T. Lanz, Astron. Astrophys. **323**, 881 (1997).
8. D. W. N. Stibbs, Mon. Not. R. Astron. Soc. **110**, 395 (1950).
9. G. W. Preston, Publ. Astron. Soc. Pac. **83**, 571 (1971).
10. H. Hensberge, W. van Rensbergen, M. Goossens, and G. Deridder, Astron. Astrophys. **61**, 235 (1977).
11. M. Landolfi, S. Bagnulo, and E. Landi Degl'Innoncenti, Astron. Astrophys. **338**, 111 (1998).
12. S. Bagnulo, M. Landolfi, and E. Landi Degl'Innoncenti, Astron. Astrophys. **308**, 115 (1994).
13. S. Bagnulo, M. Landolfi, and E. Landi Degl'Innoncenti, Astron. Astrophys. **343**, 865 (1999).
14. E. Gerth, Yu. V. Glagolevskij, and G. Scholz, in *Stellar Magnetic Fields*, Ed. by Y. V. Glagolevskij and I. I. Romanyuk (Special Astrophys. Observ. Press, Moscow, 1997), p. 67.
15. E. Gerth, Yu. V. Glagolevskij, and G. Scholz, Contrib. Astron. Obs. Skalnate Pleso **27**, 455 (1998).
16. V. R. Khalak and A. V. Shavrina, Kinematika Fiz. Nebesnykh Tel **15** (4), 327 (1999).

Translated by A. Getling

Astronomy Reports, Vol. 45, No. 7, 2001, pp. 569–576. Translated from Astronomicheskiĭ Zhurnal, Vol. 78, No. 7, 2001, pp. 661–668.

Convective Mechanism for the Formation of Photospheric Magnetic Fields

A. V. Getling

Institute of Nuclear Physics, Lomonosov Moscow State University, Moscow, 117234 Russia
e-mail: A.Getling@ru.net

Received October 16, 2000

Abstract—The well-known model that attributes the formation of a bipolar sunspot group to the emergence of a flux tube disagrees sharply with the usual observed pattern of phenomena. At the same time, the observed patterns can be accounted for quite convincingly in terms of local magnetic-field amplification due to cellular convective motions of the solar plasma. In this study, magnetoconvection in a plane horizontal fluid layer is simulated numerically in the framework of the fully nonlinear, three-dimensional problem. A weak horizontal magnetic field and weak cellular flow are assumed to be present initially. Convection is shown to be capable of producing bipolar magnetic configurations of the strongly amplified magnetic field. Indications of magnetic freezing of the flow in the cell are found. The action of the amplification mechanism under study may be controlled by the large-scale toroidal magnetic field of the Sun. *© 2001 MAIK "Nauka/Interperiodica".*

1. INTRODUCTION

The traditional scheme describing the formation of the magnetic field of a bipolar sunspot group (often silently assumed to be virtually unquestionable) is based on the idea that a magnetic flux tube lies at some depth below the solar photosphere. The strength of the magnetic field in the tube locally reaches a value sufficient for the tube to emerge under the action of magnetic buoyancy. The segment of the tube that has emerged intersects the photosphere at two sites, and two spots of opposite magnetic polarities arise precisely at these sites [1]. This view can also account for some global regularities in solar activity, e.g., the Hale law.

However, the rising-tube model can hardly offer an adequate representation of reality. First, if it is adopted, one has to account for the origin of the strong magnetic field in the tube; to this end, some additional, fairly artificial assumptions need to be introduced. Second, and especially important, is that the evolution pattern inferred from this model for a local photospheric magnetic field disagrees sharply with the corresponding pattern actually observed on the Sun. Let us list the main points of this disagreement.

(1) The strong magnetic field present in the tube would affect the convective flow even before the emergence of the tube on the surface, and subsequently the rising tube would completely break down the existing supergranular velocity field. In contrast, the actually observed flow patterns normally remain almost invariable in the process of local magnetic-field amplification [2].

(2) Certain dramatic effects, such as plasma streams spreading from the site above the rising tube, should be especially impressive but have never been observed.

(3) The emerging magnetic field itself, strong and mainly horizontal, would be directly observed in the photosphere as one of the most prominent features of the process. Nothing of the sort actually takes place.

(4) The emergence of a tube implies a sharp discrepancy in direction between the streamlines and magnetic field lines. In reality, as a spot develops, the magnetic field gradually *seeps* through the photosphere without disrupting the existing velocity field [2].

(5) According to the observations of Bumba [2], the area distribution of sunspots exhibits pronounced peaks near multiples of the area of a supergranule. Such spot-area quantization cannot be accounted for in the rising-tube model.

At the same time, an alternative possibility was suggested 35 years ago by Tverskoy [3]. He associated the process of local magnetic-field amplification with the actually observed convective motions of the solar matter in supergranules. The solar plasma circulating in a supergranular cell can amplify the magnetic field to high strengths and form a bipolar magnetic configuration typical of a sunspot group. Tverskoy's hypothesis naturally and easily overcomes the serious difficulties encountered by the rising-tube model. At the same time, the mechanism suggested by Tverskoy fits into the overall picture of solar activity at least as well as the tube mechanism does.

Tverskoy considered a simple kinematic model, assuming the fluid motion to be predefined and independent of the magnetic field. The velocity field in the supergranular convection cell was approximated by a toroidal eddy, and the electrical conductivity of the fluid was assumed to be infinite. A weak horizontal magnetic field was specified at the initial time. The

1063-7729/01/4507-0569$21.00

"winding" of magnetic field lines by the eddy produced two bunches of lines of amplified field, opposite in polarity and situated in diametrically opposed parts of the vortex ring—a bipolar magnetic configuration. This approach made it possible to arrive at a number of generalizations [4, 5]. In addition, it demonstrated the possibility of the action of a global solar hydromagnetic dynamo based on the idea of an ensemble of toroidal eddies (cells) with an azimuthal (Coriolis) velocity component, distributed over the entire convective envelope of the Sun [6].

If we suppose that precisely this convective mechanism is responsible for the formation of the bipolar magnetic configurations observed on the Sun, any artificial assumptions concerning the advance formation of flux tubes of strong magnetic fields become unnecessary, and the predicted picture comes into agreement with observations. The magnetic field lines will be stretched along streamlines, and the magnetic flux will gradually percolate through the solar surface.

However, the kinematic model leaves many questions unresolved. Among them is the most important issue of the efficiency of the mechanism under study: Can a real convection cell provide sufficient magnetic-field amplification before the flow in this cell is slowed down or the cell is disrupted by instabilities?

The convective amplification of a magnetic field is a strongly nonlinear and fundamentally three-dimensional mechanism. A thorough analysis and deep substantiation of the convective mechanism for the formation of photospheric magnetic fields thus require numerical simulations of the evolution of three-dimensional flows and magnetic fields based on a full system of magnetohydrodynamic equations. High spatial resolution is necessary for the computational scheme; such calculations have become possible only in recent years.

Some results obtained in this way will be presented here. At this early stage of investigation, we will restrict ourselves to the Boussinesq approximation (see, e.g., [7]). In other words, we will assume density variations to be negligibly small in all terms of the equations except for the term proportional to the gravitational acceleration.

Let us note that, although numerical simulations of three-dimensional magnetoconvection have been carried out for a relatively long time by various groups around the world, the mechanism of magnetic-field amplification and structuring has not been comprehensively studied. Most frequently, studies have been concerned with the effect (discovered by Weiss [8]) of spatial separation of the flow and the magnetic flux, which arises as the convection interacts with an initially imposed—as a rule, vertical—magnetic field ([9] is noteworthy among the most recent investigations in this cycle); some studies have focused attention on the oscillation and wave processes inherent in compressible magnetoconvection (as, e.g., in [10]).

2. FORMULATION OF THE PROBLEM OF NONLINEAR NUMERICAL SIMULATION

We will solve the system of magnetohydrodynamic equations in the Boussinesq approximation for a plane horizontal layer $0 < z < d$ of a fluid with finite electrical conductivity heated from below. Imagine that the layer under study is bounded from below and above by slabs of a motionless material, perfectly electrically and thermally conductive, and that the lower and upper boundary are kept at constant temperatures T_1 and T_2, respectively, their difference being ΔT. We represent any variable f of the problem as the sum of its *unperturbed* value f_0, which corresponds to the motionless state of the fluid, and a *perturbation*, which is produced by the flow (and, in general, can even substantially exceed the unperturbed value). We take the unperturbed (initial) magnetic field $\mathbf{H}_0$ to be uniform and directed horizontally, along the x axis. We denote the magnetic-field perturbation, measured in units of H_0, as $\mathbf{h}$. The perturbation of the temperature—i.e., its departure from the equilibrium, linear profile $T_0 = T_1 - \Delta T(z/d)$, expressed in units of ΔT—will be designated as θ. We choose d as the unit length and the characteristic time $t_\nu = d^2/\nu$ for viscous dissipation on the scale d as the unit time (here, ν is the kinematic viscosity). We denote the dimensionless velocity as $\mathbf{u}$.

Let us write the original system of equations in the following dimensionless form:

$$\frac{\partial \mathbf{u}}{\partial t} + (\mathbf{u}\nabla)\mathbf{u} = -\nabla\varpi + \frac{R}{P_1}\hat{\mathbf{z}}\theta - \frac{Q}{P_2}([\hat{\mathbf{H}}_0 \operatorname{curl}\mathbf{h}] + [\mathbf{h}\operatorname{curl}\mathbf{h}]) + \Delta\mathbf{u}, \tag{1}$$

$$\frac{\partial \mathbf{h}}{\partial t} = \operatorname{curl}[\mathbf{u}\hat{\mathbf{H}}_0] + \operatorname{curl}[\mathbf{u}\mathbf{h}] + \frac{1}{P_2}\Delta\mathbf{h}, \tag{2}$$

$$\frac{\partial \theta}{\partial t} - u_z + (\mathbf{u}\nabla)\theta = \frac{1}{P_1}\Delta\theta, \tag{3}$$

$$\operatorname{div}\mathbf{u} = 0, \tag{4}$$

$$\operatorname{div}\mathbf{h} = 0. \tag{5}$$

Here, $\hat{\mathbf{H}}_0 = \mathbf{H}_0/H_0$, and $\hat{\mathbf{z}}$ is a unit vector directed along the z coordinate axis, vertically upward. The quantity ϖ is the dimensionless form of the combination p'/ρ_0 (where p' is the pressure perturbation and ρ_0 is the density at temperature T_0). The dimensionless parameters

$$R = \frac{\alpha g \Delta T d^3}{\nu\chi}, \quad Q = \frac{H_0^2 d^2}{4\pi\rho_0\nu\nu_m} = \frac{H_0^2 d^2 \sigma}{\rho_0 c^2 \nu}, \quad P_1 = \frac{\nu}{\chi}, \quad P_2 = \frac{\nu}{\nu_m} = \frac{4\pi\sigma\nu}{c^2} \tag{6}$$

(where α is the volumetric thermal-expansion coefficient of the fluid, χ its thermal diffusivity, σ its electri-

cal conductivity, and ν_m its magnetic viscosity) are the Rayleigh number, Chandrasekhar number, normal Prandtl number, and magnetic Prandtl number, respectively.

We assume the surfaces of the layer to be free-slip and impermeable; i.e., we specify the condition that the normal (vertical) velocity component and tangential stresses vanish at these surfaces:

$$u_z = \frac{\partial u_x}{\partial z} = \frac{\partial u_y}{\partial z} = 0 \quad \text{at} \quad z = 0, 1. \tag{7}$$

If the slabs bounding the layer are perfectly electrically conducting, the boundary conditions for the magnetic field have a quite similar form:

$$h_z = \frac{\partial h_x}{\partial z} = \frac{\partial h_y}{\partial z} = 0 \quad \text{at} \quad z = 0, 1. \tag{8}$$

In this formulation of the problem, the temperature perturbations vanish at the layer boundaries:

$$\theta = 0 \quad \text{at} \quad z = 0, 1. \tag{9}$$

We employ the Galerkin method in the form described by Orszag [11]. We assume the velocity field, magnetic field, and thermal-perturbation field to be periodic functions of the coordinates x and y. We introduce spectral representations of these functions in the form of partial sums of trigonometric Fourier series; the boundary conditions (7)–(9) also make it possible to choose trigonometric functions to describe the z dependences. The full wavevector of a harmonic with numbers l, m, n will be $\mathbf{k}_{lmn} = \{l\alpha, m\beta, n\pi\}$, with $l < K_x$, $m < K_y$, $n < K_z$; here, α and β are the wavenumbers specifying the fundamental periods in x and y, respectively, and K_x, K_y, K_z are the spectrum bounds chosen for the computations. To reduce the number of variables, we restrict our consideration to physical fields with a certain symmetry with respect to the coordinate origin (see Figs. 1, 2, 4 below); in this case, the spectral coefficients (harmonic amplitudes) will obey certain parity relations in l and m.

Substitution of the spectral representations into the original system (1)–(5) reduces it to a system of ordinary differential equations for the harmonic amplitudes as functions of time. Following Orszag [11], we use a fast Fourier transformation to calculate the convolution sums in the right-hand sides of the spectral equations, and employ the fourth-order Runge–Kutta method to carry out the integration over time.

3. RESULTS

All the computation runs whose results are presented here were conducted for $K_x = K_y = K_z = 32$ (the run simulating a nonmagnetic flow, which assumes $K_x = K_y = K_z = 16$, is an exception). By virtue of the symmetry chosen for the initial perturbation, the number of harmonics representing the dependence of the physical fields on any coordinate is 32; therefore, the total number of basis functions used in the Galerkin representation is $32^3 = 32768$ for each variable.

In each run, a weak perturbation of the motionless state of the fluid was specified at the initial time, in the form of a collection of Bénard-type hexagonal cells (Fig. 1a); viz.,

$$u_z = -4\frac{A}{\pi}(2\cos\sqrt{3}\beta x\cos\beta y + \cos 2\beta y)\cos\pi z \quad \text{at} \quad t = 0, \tag{10}$$

where $A = -0.1$, $\beta = 2$ [with the corresponding expressions for u_x and u_y according to (4)].

We first consider the evolution of the velocity field in the absence of a magnetic field ($Q = 0$, Fig. 1); qualitatively, this pattern of evolution also holds in a number of MHD scenarios. For the conditions chosen, the three-dimensional convection regime is metastable. Fairly soon, before $t = 1$, a steady cellular flow is established (Fig. 1b); at that time, in the midplane $z = 1/2$ of the layer, the maximum value of u_z (at the center of the cell) exceeds the minimum value (at the vertices of the hexagon) in absolute magnitude. This regime is observed until at least $t = 9$. Further, the hexagonal cells undergo a sudden breakdown, and a transition to a two-dimensional roll flow takes place (Figs. 1c, 1d); in this flow, the minimum and maximum velocities over the horizontal cross section of the cell are equal in absolute magnitude (this complete history of the temporal variations of $\max u_z$ and $\min u_z$ is also observed in most scenarios with a magnetic field; see Figs. 3a and 3b below).

For the initial conditions considered, the rolls that ultimately arise from hexagons are oriented along the x axis and can be represented to first approximation by the function

$$u_z = B\cos\beta y. \tag{11}$$

It is clear that, in the case at hand, the rows of central upwellings situated in the system of hexagonal cells along different straight lines $y = \text{const}$ (e.g., $y = 0$ and $y = \pm 1.57$ in Fig. 1b) cannot behave similarly, since some rows change into continuous upflow zones, while others change into downflow zones. In the direction of the y axis, rows in which the upwellings merge (e.g., along the lines $y = \pm 1.57$) alternate with rows where the upwellings are compressed (at $y = 0$) and then disappear, giving way to expanding downflows (Figs. 1c, 1d). In which specific rows (even or odd ones, when counted along the y axis) the upwellings will merge depends on uncontrolled noise perturbations.

Note that the flow pattern of two-dimensional rolls, typical of convection in horizontal fluid layers weakly nonuniform in the vertical direction, should not necessarily arise in the solar convection zone, where compressibility and other factors complicating the stratification are present. Without discussing possibilities for

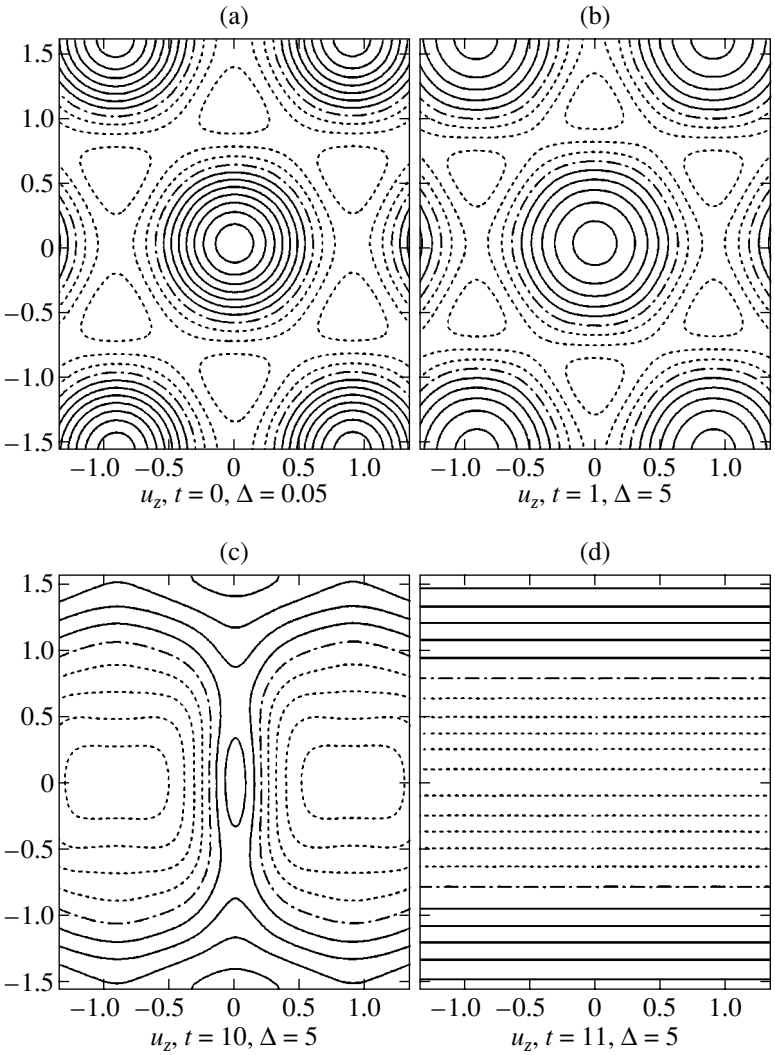

Fig. 1. Evolution of the flow in the absence of a magnetic field for $R = 3000 = 4.56R_c$ and $P_1 = 1$. Contours of the vertical velocity component u_z in the midplane $z = 1/2$ of the layer are shown with contour increment Δ (here, as in Figs. 2 and 4 below, the solid lines correspond to positive values, the dash–dot lines to zero, and dashed lines to negative values): (a) initial perturbation; (b) well-established cellular flow; (c) transition from the cellular to a roll flow; and (d) well-established roll flow.

two-dimensional convection on the Sun, we will be interested here only in phenomena occurring at the stage when the flow is three-dimensional.

We now consider the evolution of the flow and magnetic field for $R = 3000 = 4.56R_c$, $Q = 0.01$, $P_1 = 1$, and $P_2 = 10$ (Figs. 2, 3a; here, $R_c = 657.5$ is the critical Rayleigh number at which convection sets in). Crudely, by the time $t = 0.5$, the cellular flow settles down to a steady state, which persists almost until $t = 9$. During the interval $0 < t < 2$, the magnetic field is amplified by the flow, and characteristically bipolar configurations—pairs of compact magnetic islands—develop in the zones of convective upwelling, near the cell centers. At $t = 2$ or so, they reach a steady state, with a magnetic-field strength of about 41.5 (in units of H_0) within the islands. The magnetic islands remain nearly identical in all upwellings as long as the velocity field retains its original symmetry.

After $t \approx 9.5$, a rapid transition to a two-dimensional roll flow takes place. The magnetic field weakens in merging upwellings (in the case under consideration, e.g., along the line $x = 0$) and, on the contrary, is additionally amplified for some time in those upwellings that undergo compression ($x = \pm 1.57$); this is reflected by the peak in the curve of $\max H_z$ in Fig. 3a near $t = 9.9$, whose height is 49.1. Ultimately, the component of the magnetic field produced by convection decays, and the fields returns to its initial state. As is well known [12], an externally imposed horizontal magnetic field favors the formation of rolls oriented along this field. Such rolls cannot amplify the magnetic field. Nevertheless, in our case, the fairly weak initial field does not inhibit

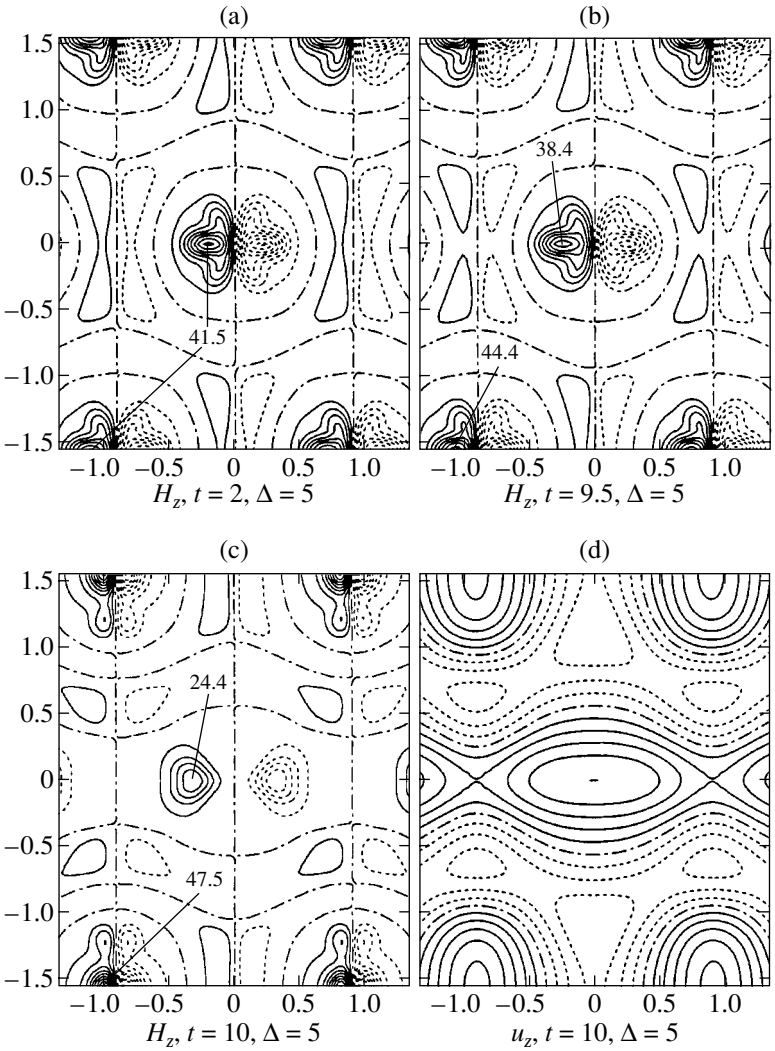

Fig. 2. Evolution of the flow and magnetic field for $R = 3000 = 4.56R_c$, $P_1 = 1$, $P_2 = 10$, and $Q = 0.01$. Contours of the vertical components of the magnetic field H_z and velocity u_z in the midplane $z = 1/2$ of the layer are shown with contour increment Δ: (a) well-established distribution of H_z; (b) deformation of the distribution of H_z shortly after the loss of the steady state and cell symmetry; and (c, d) distributions of H_z and u_z, respectively, at the stage of the transition from the cellular flow to a roll flow. Same notation as in Fig. 1 is used for the contours.

the development of three-dimensional convective flows.

Varying the Chandrasekhar number Q (actually, the initial magnetic-field strength) with other parameters fixed demonstrates that the main features of the scenario described are typical of the range $0.001 < Q < 1$ studied (the cases of $Q = 0.001$ and $Q = 0.01$ are very similar not only qualitatively, but also quantitatively). A comparison of scenarios computed for various Q values (Fig. 3) shows that a strong initial field ($Q = 1$) results in a rapid transition to rolls, while the period of existence of the three-dimensional flow becomes longer as Q is decreased.

The influence of the parameters R and P_2 can easily be predicted. An increase in the Rayleigh number R to $4000 = 6.08R_c$ raises the steady-state value of $\max H_z$ to 49.2 and the peak value (at $t \approx 7.6$) to 50.9. The efficiency of magnetic-field amplification grows rapidly with increase of the magnetic Prandtl number P_2. For $P_2 = 30$, as can be seen from Fig. 4, the value of $\max H_z$ at the steady-state stage proves to be much larger than for $P_2 = 10$, and even exceeds 170 at the upwelling-compression stage. The islands of amplified magnetic field at $P_2 = 30$ are more compact than at $P_2 = 10$.

4. DISCUSSION

Thus, our computations confirm qualitative conclusions based on the model of Tverskoy [3]. In any particular case, the efficiency of the convective mechanism

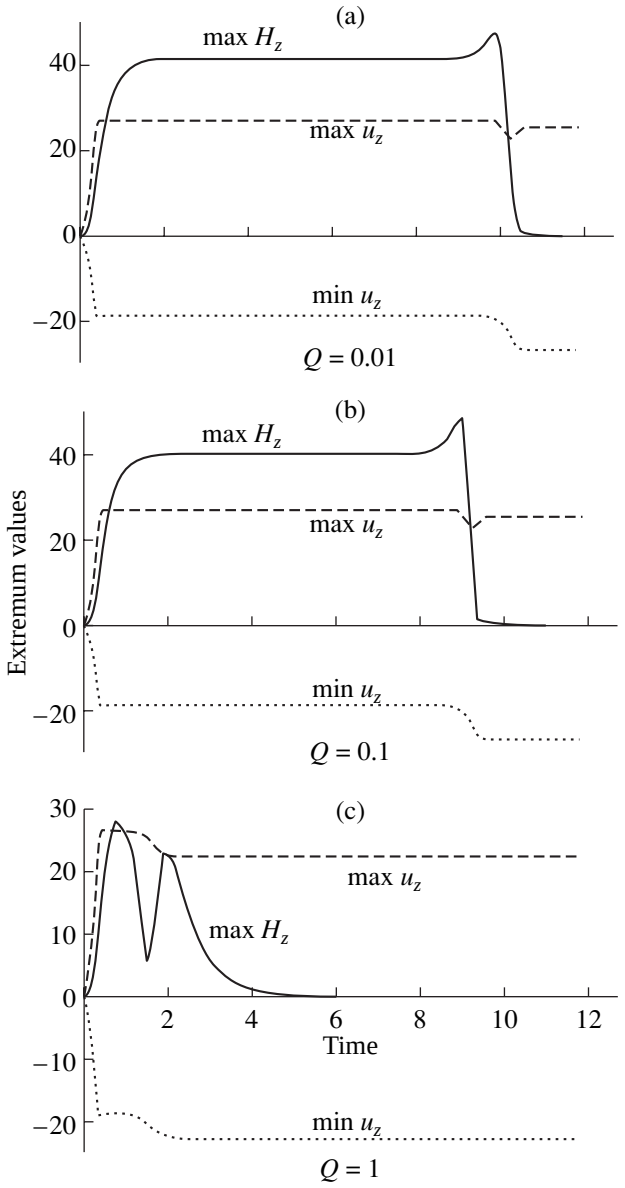

Fig. 3. Time variation of extremum values of the vertical components of the magnetic field and velocity for $R = 3000 = 4.56R_c$, $P_1 = 1$, $P_2 = 10$, and (a) $Q = 0.01$, (b) $Q = 0.1$, and (c) $Q = 1$.

can be measured by the maximum achieved dimensionless H and the ratio γ of the maximum values of the magnetic- and kinetic-energy densities E_m and E_k:

$$E_m = \frac{H_0^2(\max H_z)^2}{8\pi}, \quad E_k = \frac{\rho_0(\max u_z)^2}{2}\frac{\nu^2}{d^2}, \qquad \gamma = \frac{E_m}{E_k} = \frac{Q(\max H_z)^2}{P_2(\max u_z)^2}. \tag{12}$$

This ratio increases with R and P_2, and also with Q—until the flow braking by the magnetic field becomes strong. In particular, in the scenarios presented in Fig. 3, $\gamma \approx 0.003$ for $Q = 0.01$ (Fig. 3a), $\gamma \approx 0.032$ for $Q = 0.1$ (Fig. 3b), and $\gamma \approx 0.1$ for $Q = 1$ (Fig. 3c); in the last case, the braking is fairly strong, and the amplified magnetic field rapidly disrupts the three-dimensional flow. In the case illustrated by Fig. 4, $\gamma \approx 0.013$, while the preliminary results obtained for $R = 5000$, $P_1 = 1$, $P_2 = 30$ yield $\gamma \approx 1$ for $Q = 1$ and $\gamma \approx 1.24$ for $Q = 3$. Since a 170-fold amplification is possible at quite moderate values of R and P_2, larger values of these parameters could undoubtedly provide amplification by factors of many hundreds or even thousands. Thus, the convective magnetic-field amplification mechanism described here should be very efficient and is promising in the context of searches for sources of strong photospheric magnetic fields. In particular, our computations demonstrate the possibility of the formation of very compact magnetic islands. For this reason, it will be useful to investigate the possible role of this mechanism in producing not only sunspots and active regions, but also compact magnetic elements.

A comparison between the computation runs with and without a magnetic field shows that the amplified magnetic field can leave the flow structure and velocity in a cell virtually unaffected. This is likely a manifestation of the effect predicted earlier from the kinematic model [13]. The Ampére force of flow braking due to the magnetic field is determined by the product $[\mathbf{H}\mathrm{curl}\mathbf{H}] \cdot \mathbf{v}$. The $\mathbf{H}$ component that grows with time is parallel to the velocity vector $\mathbf{v}$, whereas the component normal to $\mathbf{v}$ is of the order of the initial field $\mathbf{H}_0$. Therefore, the braking force is proportional to $H_0|\mathrm{curl}\mathbf{H}|$. Given the order of magnitude of the amplified field $\mathbf{H}$, the energy losses due to braking will be smaller the weaker the initial field $\mathbf{H}_0$. One can easily imagine situations where larger final amplified field strengths will be achieved with smaller initial field strengths—of course, if the flow in the cell remains stable, and the process develops in accordance with the model scenario.

Moreover, the amplified field aligned with the streamlines should stabilize the fluid flow. The lines of the amplified field are "rails" laid by the flow, which should counteract changes in the flow configuration. At the same time, the magnetic-field component normal to the velocity vector, which can destabilize the flow, retains a magnitude of order H_0. Thus, weak magnetic fields are favorable for the operation of this mechanism also in terms of stability. It is possible that, at sufficiently small H_0 and sufficiently large magnitude of the amplified magnetic field, the latter will exert a "freezing" effect on the flow.

At this stage, it would be premature to attempt to estimate the parameter values typical of the solar convection zone, where the viscosity and thermal conductivity are controlled by turbulent transport and are thus highly indeterminate. Large Rayleigh numbers R can be expected; however, the mere presence of a relatively regular supergranular pattern on the Sun suggests that

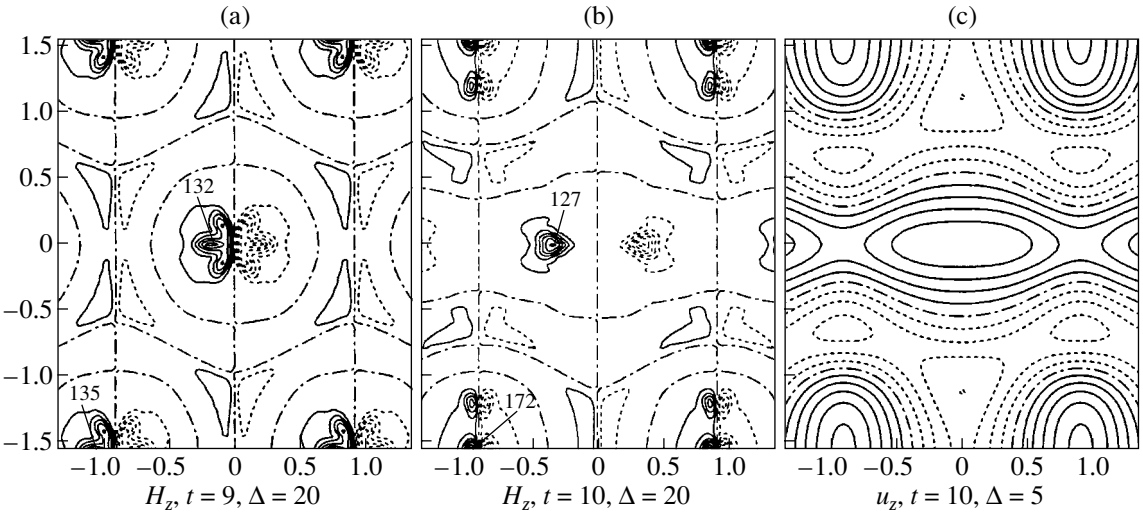

Fig. 4. Evolution of the flow and magnetic field for $R = 3000 = 4.56R_c$, $P_1 = 1$, $P_2 = 30$, and $Q = 0.01$. Contours of the vertical components of the magnetic field H_z and velocity u_z in the midplane $z = 1/2$ of the layer are shown with contour increment Δ: (a) deformation of the distribution of H_z shortly after the loss of the steady state and cell symmetry; (b, c) distributions of H_z and u_z, respectively, at the stage of the transition from the cellular flow to a roll flow. Same notation as in Fig. 1 is used for contours.

the effective R for the corresponding layers is maintained by small-scale turbulent processes on a level at which convection remains quasi-laminar. The electrical conductivity of the solar plasma in the convection zone grows rapidly with depth, reaching values for which the magnetic field can be considered to be completely frozen in the plasma. Turbulence should reduce the effective conductivity. However, as can be judged by the observed picture, the magnetic-field dynamics do not depart too strongly from a freezing-in regime, even in layers that can be directly observed; therefore, the magnetic Prandtl number P_2 still remains fairly high. Effective hydrodynamic Prandtl numbers of order unity are usually considered plausible.

The pattern of the evolution of photospheric magnetic fields controlled by the convective mechanism is free of the contradictions with observations inherent in the rising-tube model (see Introduction).

For the convective mechanism to come into action, it is necessary that an especially large and intense supergranular cell encompassing layers deeper than usual be threaded with a weak seed magnetic field. Such a field is unlikely to be highly ordered, but the spatially averaged vector of this field could naturally be identified with the large-scale toroidal (latitudinally directed) magnetic field; the presence of such a preferred direction of the magnetic field at the initial time is, in principle, sufficient for the field to subsequently evolve in qualitative agreement with the computed scenarios. Therefore, the seed field should be controlled by large-scale dynamo processes, and should introduce a global regularity into the distribution of sunspot groups. Nothing but convection on supergranular and sunspot scales will serve as a connecting link between the global and local processes.

Diverse initial conditions can ensure the generation of diverse configurations of the amplified magnetic field. In particular, if the initial magnetic field is directed vertically, a unipolar-type configuration will form, whereas oblique initial fields will produce a variety of superpositions of unipolar, bipolar, and higher multipolar fields. If the seed field threads a group of cells, the interaction of the flows with the magnetic field will be "collective," and the amplified field will have a more complex structure; in this case, natural prerequisites arise for the manifestation of the sunspot-area quantization pointed out in [2].

Let us summarize the main conclusions of this study.

(1) The convective mechanism considered here, which does not require strong initial magnetic fields, is highly efficient, i.e., it can form bipolar configurations of a multiply amplified magnetic field.

(2) This mechanism provides a natural explanation for the general, global regularities in the behavior of local solar magnetic fields and for the quantization of sunspot areas.

(3) The basic features of the magnetic-field amplification process are in agreement with the observed pattern for the evolution of flows and magnetic fields in the regions where sunspot groups develop.

5. ACKNOWLEDGMENTS

I am grateful to the Pushchino Radio Astronomy Observatory of the Russian Academy of Sciences for computer-resource allocation, to I.L. Ovchinnikov for invaluable help in arranging and performing the computations, and to L.M. Alekseeva for perpetual fruitful discussions. This work was supported by the Russian Foundation for Basic Research (project code 00-02-16313).

REFERENCES

1. E. N. Parker, Astrophys. J. **121**, 491 (1955).
2. V. Bumba, *Rendiconti della Scuola Internazionale di Fisica* "*E.Fermi*," 39 Corso (1967), p. 77.
3. B. A. Tverskoy, Geomagn. Aeron. **6** (1), 11 (1966).
4. A. V. Getling and B. A. Tverskoy, Astron. Zh. **45** (3), 606 (1968).
5. A. V. Getling, Dokl. Akad Nauk SSSR **187** (2), 301 (1969).
6. A. V. Getling and B. A. Tverskoy, Geomagn. Aeron. **11** (2), 211 (1971); **11** (3), 389 (1971).
7. A. V. Getling, *Rayleigh–Bénard Convection: Structures and Dynamics* (World Scientific, Singapore, 1998; URSS, Moscow, 1999).
8. N. O. Weiss, Mon. Not. R. Astron. Soc. **128**, 225 (1964).
9. L. Tao, N. O. Weiss, D. P. Brownjohn, and M. R. E. Proctor, Astrophys. J. Lett. **496**, L39 (1998).
10. N. E. Hurlburt, P. C. Matthews, and M. R. E. Proctor, Astrophys. J. **457** (2), 933 (1996).
11. S. A. Orszag, Stud. Appl. Math. **50** (4), 293 (1971); J. Fluid Mech. **49** (1), 75 (1971).
12. S. Chandrasekhar, *Hydrodynamic and Hydromagnetic Stability* (Oxford, Clarendon, 1961).
13. A. V. Getling, Astron. Zh. **45** (6), 1222 (1968).

Translated by A. Getling

Astronomy Reports, Vol. 45, No. 7, 2001, pp. 577–579. Translated from Astronomicheskiĭ Zhurnal, Vol. 78, No. 7, 2001, pp. 669–672.

The Hamiltonian in the Planetary or Satellite Problem as a D'Alembertian Function

K. V. Kholshevnikov

Astronomical Institute, St. Petersburg State University, Bibliotechnaya pl. 2, St. Petersburg, 198504 Russia

Received October 15, 1999

Abstract—This completes a series of three articles establishing the d'Alembertian properties of key functions in celestial mechanics. The first two presented the concept of a d'Alembertian function of a pair of complex variables specified within an infinitely long bottle with a narrowing neck. The main properties of d'Alembertian functions were demonstrated, and it was shown that the main functions in celestial mechanics belong to this class, including Cartesian coordinates. The d'Alembertian radii of these functions were found and their moduli estimated, in many cases exactly. The current paper demonstrates the d'Alembertian nature of the perturbing function—or equivalently, the Hamiltonian—in the planetary or satellite problem. The d'Alembertian radius of this function is estimated. © *2001 MAIK "Nauka/Interperiodica".*

1. INTRODUCTION

The current paper completes a short series of articles dedicated to d'Alembertian functions as natural functionals of the space $\mathfrak{D}$ in problems in celestial mechanics. The motivation, definitions, and main properties of these functions are described in [1, 2]. The membership of the main functions of celestial mechanics in the space $\mathfrak{D}$, including the differences of anomalies and Cartesian coordinates in Keplerian motion, is demonstrated in [2, 3]. Here, we consider the d'Alembertian properties of perturbing functions, and thereby the Hamiltonians, of planetary and satellite problems in various coordinate systems.

2. PERTURBING FUNCTION IN HELIOCENTRIC MOTION

Let us consider the motion of material points Q_0, …, Q_N with masses m_0, …, m_N under the action of Newtonian gravity. We refer the positions Q_i ($i = 1, \ldots, N$) to the point Q_0, denoting $\mathbf{r}_i$ to be the vector Q_0Q_i. The components $\mathbf{r}_i$ are usually called heliocentric coordinates, having in mind the planetary interpretation of the problem. The equation of motion of the points Q_i has the form [4]

$$\ddot{\mathbf{r}}_i + \kappa_i^2 \frac{\mathbf{r}_i}{r_i^3} = \operatorname{grad}_i U_i, \tag{1}$$

$$U_i = \sum G m_k \left(\frac{1}{|\mathbf{r}_k - \mathbf{r}_i|} - \frac{\mathbf{r}_i \mathbf{r}_k}{r_k^3} \right). \tag{2}$$

Here, G is the gravitational constant, $\kappa_i^2 = G(m_0 + m_i)$, and the sum over k is from 1 to N, omitting the value $k = i$.

When $U_i = 0$, the motion of Q_i is described by Keplerian elements, which we take to have major axis a_i, eccentricity e_i, sine of the half-inclination s_i, mean longitude α_i, longitude of pericenter β_i, and longitude of the ascending node γ_i. The mean motion n_i is related to the major axis by the formula $n_i = \kappa_i a_i^{-3/2}$. When $U_i \neq 0$, the elements are osculating: the position Q_i depends on six elements, and its velocity depends in addition on n_i (or equivalently on κ_i) *in accordance with the formulas of elliptical Keplerian motion.*

We can expand the domain of definition of functions in celestial mechanics to complex-valued elements. Namely, we consider the osculating elements varying in the domain **D**:

$$\begin{gathered} \left| \frac{a_i - A_i}{A_i} \right| \le \varepsilon_{1i}, \quad |\Im \alpha_i| \le \varepsilon_{2i}, \\ |e_i| \exp |\Im \beta_i| < R_{1i}, \quad |s_i| \exp |\Im \gamma_i| < R_{2i}, \end{gathered} \tag{3}$$

where A_i and the right-hand sides of the inequalities are the specified positive numbers. If

$$\varepsilon_{1i} < 1, \quad R_{2i} \le 1, \quad R_{1i} \le R_0 \exp(-\varepsilon_{2i}), \tag{4}$$

then, according to [3], the Cartesian coordinates and radii of the points Q_i are holomorphic and restricted to **D**, with the radii differing from zero. Here, $R_0 = 0.662743$ is the Laplace limit.

Therefore, the components $\mathbf{r}_i$, their scalar products, the powers of the radii r_i^{-3}, and the squares of the moduli of the difference vectors are, by definition, equal to

$$r_{ik}^2 = r_i^2 + r_k^2 - 2\mathbf{r}_i \mathbf{r}_k, \tag{5}$$

Table 1. Most probable $R_{15} = R_{16}$ as a function of $\varepsilon_{15} = \varepsilon_{16}$

ε_{15}	0	0.1	0.2	0.2925
R_{15}	0.2925	0.1983	0.0983	0

Table 2. Most probable R_{12}, $R_{13} = qR_{12}$ as a function of q, $\varepsilon_{12} = \varepsilon_{13}$

ε_{12}	0	0.05	0.1	0.1628
$R_{12}(q = 1)$	0.1628	0.1137	0.0638	0
$R_{12}(q = 2)$	0.1029	0.0730	0.0417	0
$R_{13}(q = 2)$	0.2059	0.1461	0.0833	0
$R_{12}(q = 2.5)$	0.0870	0.0620	0.0355	0
$R_{13}(q = 2.5)$	0.2174	0.1549	0.0888	0

and are holomorphic and restricted to **D** under conditions (4). *However, the functions* r_{ik}^{-1} *, together with* U_i*, are certain to have critical poles in the domain* **D** *if its parameters are close to their upper limits* (4). Indeed, the inequality (3) does not impose restrictions on the real parts of α_i, β_i, and γ_i. Therefore, there are present in **D** points $Q_i = Q_k$ for which $r_{ik} = 0$, corresponding to collisions. Note that, in the complex case, $r_{ik} = 0$ does not necessarily imply that $Q_i = Q_k$.

When the U_j are holomorphic, it is necessary first and foremost to consider the A_i (mean major axes of the planets) to be different; otherwise, it is not possible to avoid collisions in the real domain. In addition, we must decrease the right-hand sides of (4). This is sufficient: infinitely small ε_{1i}, ε_{2i}, R_{1i}, and R_{2i} correspond to an infinitely small complex neighborhood of planar circular orbits with radii A_i; due to continuity, the r_{ik}^2 differ from zero in this neighborhood.

Theorem 1. For fixed different A_i and sufficiently small ε_{1i}, ε_{2i}, R_{1i}, and R_{2i}, the functions $U_1, \ldots, U_N$ are holomorphic in **D**, and are R_{1i} d'Alembertian with respect to the pair (e_i, β_i) and R_{2i} d'Alembertian with respect to the pair (s_i, γ_i). Indeed, the holomorphicity demonstrated above and the d'Alembertian nature of these functions flow from the properties 3 of d'Alembertian functions [2].

How small must the domain **D** be? Since the major axes of the orbits grow in a geometrical progression, it is sufficient to consider a successive planetary pair Q_i, Q_k, $k = i + 1$. Initially, we assume that all elements are real. Obviously,

$$|\mathbf{r}_k - \mathbf{r}_i| \geq r_k - r_i \geq a_k(1 - e_k) - a_i(1 + e_i),$$

and finally,

$$\begin{aligned} |\mathbf{r}_k - \mathbf{r}_i| \geq A_k(1 - \varepsilon_{1k})(1 - R_{1k}) \\ - A_i(1 + \varepsilon_{1i})(1 + R_{1i}), \end{aligned} \tag{6}$$

with the equality achieved at certain points on the boundaries of **D**. The quantities A_j can be taken to be fixed (they are the mean major axes). Setting the right-hand side of (6) equal to zero, we obtain a relation between the largest possible values of the four parameters ε_{1i}, R_{1i}, ε_{1k}, and R_{1k}. Since the first of the inequalities (3) gives the *relative* deviation a from A, it is reasonable to take $\varepsilon_{1k} = \varepsilon_{1i}$. The eccentricities of the planetary orbits appreciably differ from each other; therefore, we assume

$$R_{1k} = qR_{1i},$$

sorting several values of q. For given A_i, A_k, and q, we obtain a linear relation between two parameters, which can rationally be written in the two forms

$$\begin{aligned} \varepsilon_{1i} &= \frac{A_k(1 - qR_{1i}) - A_i(1 + R_{1i})}{A_k(1 - qR_{1i}) + A_i(1 + R_{1i})}, \\ R_{1i} &= \frac{A_k(1 - \varepsilon_{1i}) - A_i(1 + \varepsilon_{1i})}{qA_k(1 - \varepsilon_{1i}) + A_i(1 + \varepsilon_{1i})}. \end{aligned} \tag{7}$$

We consider two pairs as an example: Jupiter–Saturn ($i = 5, k = 6$) and Venus–Earth ($i = 2, k = 3$). We adopt $A_5 = 5.2$, $A_6 = 9.5$, $A_2 = 0.72$, and $A_3 = 1$ AU. Since the eccentricities are $e_6 \approx e_5$ and $e_3 \approx 2.4e_2$, we adopt $q = 1$ for the outer pair and the three values $q = 1$, $q = 2$, and $q = 2.5$ for the inner pair. The limits of variation of $\varepsilon_{1i} = \varepsilon_{1k}$, R_{1i}, and R_{1k} are presented in Tables 1 and 2. Recall that the estimates (7) are reached in the real domain of variation of the variables. In particular, for fixed semiaxes, real values of s_j, α_j, β_j, and γ_j are found, such that a Macloren expansion in powers of the eccentricities converges best when

$$|e_5| < 0.2925, \quad |e_6| < 0.2925.$$

We have three possibilities for the Venus–Earth distance:

$$|e_2|, |e_3| < 0.1628; \quad |e_2| < 0.1029,$$
$$|e_3| < 0.2059; \quad |e_2| < 0.0870, \quad |e_3| < 0.2775.$$

These last data can be represented as flowing from (7) via the linear dependence of R_{1k} on R_{1i} when $\varepsilon_{1i} = \text{const}$. In particular, when $\varepsilon_{12} = \varepsilon_{13} = 0$,

$$R_{13} = 1 - A_2/A_3 - A_2R_{12}/A_3 = 0.28 - 0.72R_{12}.$$

Dividing the mean eccentricities by the right-hand sides of these inequalities, we can conclude the following. With specified "poor" values s_j, …, and γ_j, the Macloren expansions for $|\mathbf{r}_6 - \mathbf{r}_5|^{-1}$ converge no more rapidly than a geometrical progression with the denominators $e_5^* = 0.16$ and $e_6^* = 0.19$. We have three possibilities for the Venus–Earth distance:

$$e_2^* = 0.043, \quad e_3^* = 0.104; \quad e_2^* = 0.068,$$
$$e_3^* = 0.083; \quad e_2^* = 0.080; \quad e_3^* = 0.078.$$

Thus, *the domain of convergence of the perturbing functions expanded in powers of the eccentricities is appreciably worse* than the coordinate domain in the two-body problem determined by the Laplace limit. Accordingly, the denominators of the progressions are *larger than the eccentricities* by factors of three to five or more.

Recall that, above, we restricted our consideration to real arguments. Thus, the estimates we have obtained can be thought of as a view of the world through rose-colored glasses. In particular, a restriction on the inclination s_j did not even arise.

It is difficult to obtain nearly exact analytical estimates in a complex domain, if it is possible at all, and numerical estimates are rather cumbersome. We put off such analyses to the future.

3. THE PERTURBING FUNCTION IN JACOBIAN COORDINATES

Jacobian coordinates have many advantages over heliocentric coordinates in theoretical problems. In particular, there exists a single perturbing function U equal to a linear combination of the quantities

$$r_i^{-1}, \quad \rho_i^{-1}, \quad |\boldsymbol{\rho}_k - \boldsymbol{\rho}_i|^{-1}.$$

Here, $\mathbf{r}_i$ and $\boldsymbol{\rho}_i$ are vectors whose components serve as the Jacobian and heliocentric coordinates Q_i [4]. As in the previous section, ρ_i^2 and $(\boldsymbol{\rho}_k - \boldsymbol{\rho}_i)^2$ are polynomials that are second-order in the coordinates in the two-body problem, which are d'Alembertian in the domain **D** under the restrictions (4). In the same way, Theorem 1 is valid, with exchange of the functions U_i with U. The numerical estimates of the parameters of the domain **D** likewise change little, since the differences of ρ_i and $|\boldsymbol{\rho}_k - \boldsymbol{\rho}_i|$ from r_i and $|\mathbf{r}_k - \mathbf{r}_i|$ are of the order of the ratio of planetary masses to the solar mass.

4. THE SATELLITE PROBLEM

In the problem of satellite motion, the influence of external bodies is described in the same way as for the planetary problem, so that the properties of interest to us are transferred to that case.

The effect of the non-sphericity of the planets is described by the external gravitational potential U. For Earth-group planets and other rough bodies, U has a singularity (in addition to the usual singularities associated with Cartesion coordinates and the radius) at $|\mathbf{r} - \mathbf{r}'| = 0$, where $\mathbf{r}'$ is the radius vector of an arbitrary point on the planetary surface. The only difference from the previous case is that $\mathbf{r}'$ runs through a continuum of real values, rather than a finite set of complex values. Therefore, Theorem 2 is valid.

Theorem 2. For fixed A and sufficiently small ε_1, ε_2, R_1, and R_2, the function U is holomorphic in **D**, and is R_1 d'Alembertian with respect to the pair (e, β) and R_2 d'Alembertian with respect to the pair (s, γ).

A substantially stronger result is valid for smooth or nearly spherical bodies, for which the potential U is well approximated by the function $\tilde{U}$, which can be represented as a polynomial in the coordinates x, y, z divided by some power of r. A segment of a Laplace series is usually taken for $\tilde{U}$, or a combination of spherical functions that, in some well defined sense, best approximates V [5].

Theorem 3. For fixed A, the function $\tilde{U}$ is holomorphic in **D** and is R_1 d'Alembertian with respect to the pair (e, β) and R_2 d'Alembertian with respect to the pair (s, γ) if the parameters of the domain **D** satisfy restrictions of type (4):

$$\varepsilon_1 < 1, \quad R_2 \le 1, \quad R_1 \le R_0 \exp(-\varepsilon_2). \tag{8}$$

Indeed, the function $\tilde{U}$ has no other singularities, apart from coordinate singularities and those associated with r becoming zero.

REFERENCES

1. K. V. Kholshevnikov, Prikl. Mat. Mekh. **41** (5), 870 (1977).
2. K. V. Kholshevnikov, Astron. Zh. **74**, 149 (1997) [Astron. Rep. **41**, 135 (1997)].
3. K. V. Kholshevnikov and O. K. Tublina, Astron. Zh. **75**, 476 (1998) [Astron. Rep. **42**, 420 (1998)].
4. M. F. Subbotin, *Introduction to Theoretical Astronomy* [in Russian] (Nauka, Moscow, 1968).
5. V. A. Antonov, E. I. Timoshkova, and K. V. Kholshevnikov, *Introduction to the Theory of Newtonian Potentials* [in Russian] (Nauka, Moscow, 1988).

Translated by D. Gabuzda